General Disclaimer

One or more of the Following Statements may affect this Document

- This document has been reproduced from the best copy furnished by the organizational source. It is being released in the interest of making available as much information as possible.

- This document may contain data, which exceeds the sheet parameters. It was furnished in this condition by the organizational source and is the best copy available.

- This document may contain tone-on-tone or color graphs, charts and/or pictures, which have been reproduced in black and white.

- This document is paginated as submitted by the original source.

- Portions of this document are not fully legible due to the historical nature of some of the material. However, it is the best reproduction available from the original submission.

Spaceborne Imaging Radar Symposium

January 17-20, 1983
Jet Propulsion Laboratory

July 1, 1983

NASA

National Aeronautics and
Space Administration

Jet Propulsion Laboratory
California Institute of Technology
Pasadena, California

Spaceborne Imaging Radar Symposium

January 17-20, 1983
Jet Propulsion Laboratory

July 1, 1983

NASA

National Aeronautics and
Space Administration

Jet Propulsion Laboratory
California Institute of Technology
Pasadena, California

CONTENTS

CONTENTS (Contd)

CONTENTS (Contd)

ABSTRACT

This document contains the abstracts of the papers presented at the Spaceborne Imaging Radar Symposium held at the Jet Propulsion Laboratory, California Institute of Technology, in Pasadena, California, on January 17-20, 1983. The purpose of the Symposium was to present an overview of the present state-of-the-art in the different scientific and technological fields related to spaceborne imaging radars. The data acquired with the Seasat SAR (1978) and Shuttle Imaging Radar, SIR-A (1981) clearly demonstrated the important emphasis in the 80's is going to be on in-depth research investigations to be conducted with the more flexible and sophisticated SIR series instruments and on long-term monitoring of geophysical phenomena to be conducted from free-flying platforms such as ERS-1 and Radarsat.

INTRODUCTION

This document contains the abstracts of the papers presented at the Spaceborne Imaging Radar Symposium held at the Jet Propulsion Laboratory, California Institute of Technology, in Pasadena, California, on January 17-20, 1983. The purpose of the Symposium was to present an overview of the present state-of-the-art in the different scientific and technological fields related to spaceborne imaging radars. The data acquired with the Seasat SAR (1978) and Shuttle Imaging Radar, SIR-A (1981) clearly demonstrated the important role spaceborne radars could play in Earth and planetary observations. The emphasis in the '80s is going to be on in-depth research investigations to be conducted with the more flexible and sophisticated SIR series instruments and on long-term monitoring of geophysical phenomena to be conducted from free-flying platforms such as ERS-1 and Radarsat.

Later this year the German MRSE sensor will be flown on Spacelab-1 and will provide the first X-band radar images from space. In 1984 the SIR-B experiment will be conducted, providing L-band data at a wide variety of incidence angles. Plans are under development for a SIR-C/MRSE flight in 1986. The SIR-C will have L- and C-band channels and polarization diversity. This experiment will provide data at L-, C-, and X-bands. Thus, it is expected that in the next three years, research activity in spaceborne radar remote sensing will continue aggressively, leading to a much better understanding and utilization of radar data in geophysical research and observation.

Charles Elachi
Symposium Chairman

Geologic Research

GEOLOGIC APPLICATION OF SPACEBORNE RADARS

Floyd F. Sabins, Jr.
Chevron Oil Field Research Company
La Habra, California

Earth and Space Science Department
University of California, Los Angeles

This paper illustrates geologic applications of spaceborne radar images, specifically Seasat in southern California and SIR-A in Indonesia.

I. SEASAT IMAGE OF DURMID HILLS, CALIFORNIA

The San Andreas fault bisects the Durmid Hills, which form a broad, low ridge on the east shore of the Salton Sea. There is little vegetation or soil cover in this arid region. but the trace of the San Andreas fault is obscure on aerial photographs, Landsat images, Ka-band aircraft radar images, and Skylab photographs (Fig. 1A). On the SIR-A image (Fig. 1B), however, the fault is clearly indicated where terrain with contrasting bright and dark radar signatures is separated by a distinct linear contact (Sabins, Blom, and Elachi, 1980). For Seasat (average depression angle of $70°$ and wavelength of 23.5 cm) the Rayleigh roughness criterion predicts that surfaces with relief greater than 5.7 cm will appear rough to the incident radar beam, resulting in strong backscattering and a bright image signature. Surfaces with relief less than 1.0 cm appear smooth and specularly reflect the incident radar beam which results in minimal backscattering and a dark image signature. Field checking showed that the bright signature correlates with outcrops of the Borrego Formation (Pliocene-Pleistocene), which consists predominantly of nonresistant siltstone with interbeds of resistant sandstone and concretions (Fig. 1C). Erosion produces a highly dissected surface littered with large angular fragments of sandstone. The relief exceeds the rough criterion and explains the bright radar signature of the Borrego outcrops. The dark signature correlates with areas covered by sand and silt deposited in Lake Coahuila, which occupied the Salton depression until a few hundred years ago. This surface is essentially undissected and has a relief less than the smooth criterion, which explains the dark radar signature.

II. SIR-A IMAGES OF INDONESIA

Detailed interpretations of the limited SIR-A coverage of Indonesia are being reported elsewhere (Sabins, 1983). One example from the Vogelkop region in western Irian Jaya is summarized here to demonstrate the geologic applications of SIR-A images in this heavily forested, cloud-covered, poorly accessible region that is well suited for radar investigations. Geologic interpretation of radar images involves two operations: (1) recognize and record the distribution of geologic units, and (2) map geologic structures.

In the SIR-A images of Indonesia, the following geologic units are recognized: alluvial and coastal terrain; clastic terrain; carbonate terrain; volcanic terrain; metamorphic terrain; melange terrain; and other types of bedrock. Five of these categories are shown in the image and terrain interpretation map (Fig. 2). In the well-exposed Durmid Hills area, geologic

3, 4

units were distinguished by differences in surface roughness. Because of soil and vegetation cover in Indonesia, however, roughness criteria are not useful for this purpose; therefore, geologic units are distinguished by their weathering characteristics. For example, solution and collapse of limestone in this humid environment produces karst topography with its pitted appearance that is characteristic of carbonate terrain. In Fig. 2, typical carbonate terrain occurs in the southern (lower right) corner of the image and map. Clastic terrain is characterized by ledge and slope topography formed by alternating resistant and nonresistant strata. Metamorphic terrain is characterized by angular ridges with no evidence of stratification.

Structural interpretation of a SIR-A image is illustrated in the map and cross section of Fig. 3, where strike and dip, lineaments, faults, and folds are recorded. The structural and lithologic interpretations agree with geologic maps that became available after completion of the SIR-A interpretation. For example, a high proportion of the lineaments on the image coincide with mapped faults, and it is possible that the other lineaments may represent previously unmapped faults.

III. SUMMARY

Spaceborne radar images have proven valuable for geologic interpretation in a wide range of environments. The major hindrance to this application is the lack of adequate images. Therefore, it is recommended that global coverage be acquired by spaceborne radar systems with emphasis on regions where persistent cloud cover hampers the acquisition of images in the visible spectral band.

REFERENCES

Sabins, F. F., 1983, Geological interpretation of Space Shuttle radar images of Indonesia, American Association of Petroleum Geologists Bulletin, in press.

Sabins, F. F., R. Blom, and C. Elachi, 1980, Seasat radar image of San Andreas fault, California, American Association of Petroleum Geologists Bulletin, V. 64, pp. 619-628.
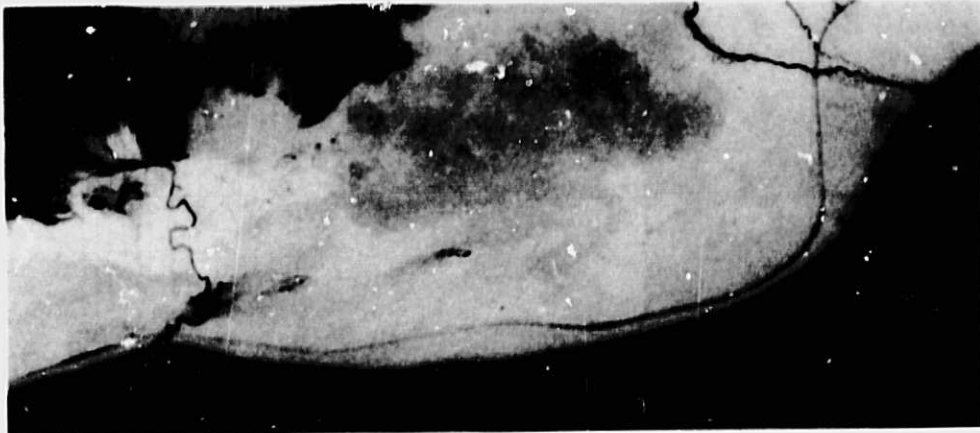
A. Skylab −3 infrared black-and-white photograph.
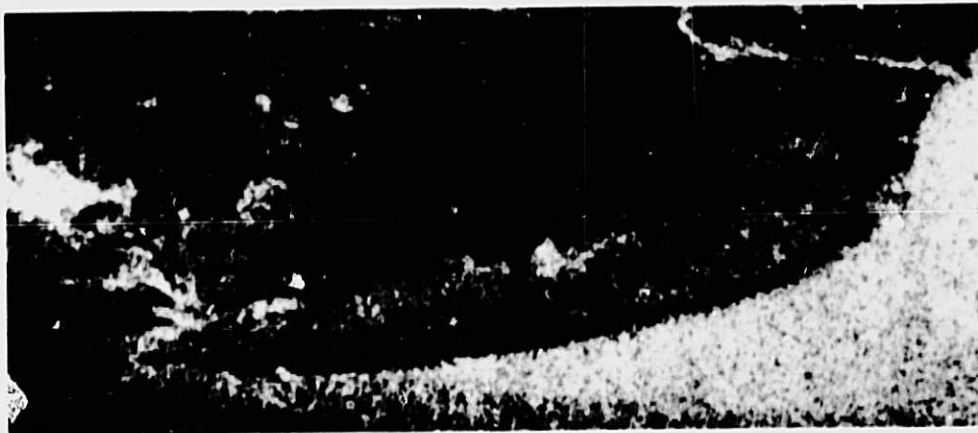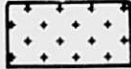
B. Seasat radar image.
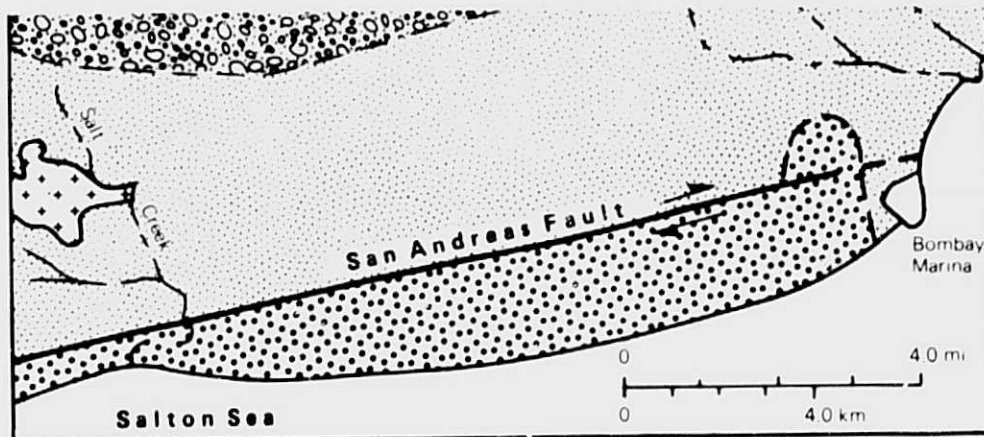
C. Geologic interpretation of Seasat image.

ALLUVIAL FAN DEPOSITS OF SAND AND GRAVEL

SALT CRUST

LAKE COAHUILA DEPOSITS OF SAND AND SILT

BORREGO FORMATION OUTCROPS

Fig. 1. Durmid Hills, Southern California. From Sabins, Blom, and Elachi (1980, Figs. 5, 9).
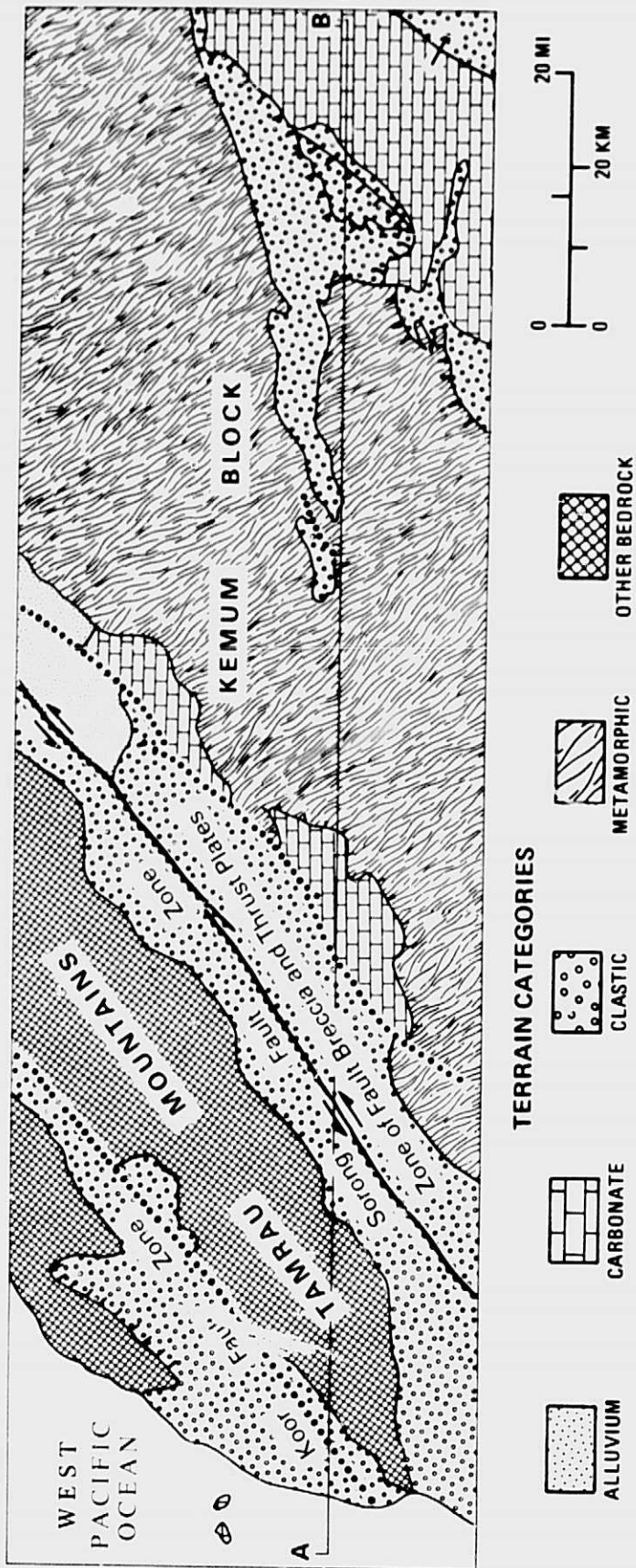
Fig. 2. Northwestern Vogelkop region, Irian Jaya, Indonesia. SIR-A image and interpretation of terrain types. From Sabins (1983, Fig. 10).

8
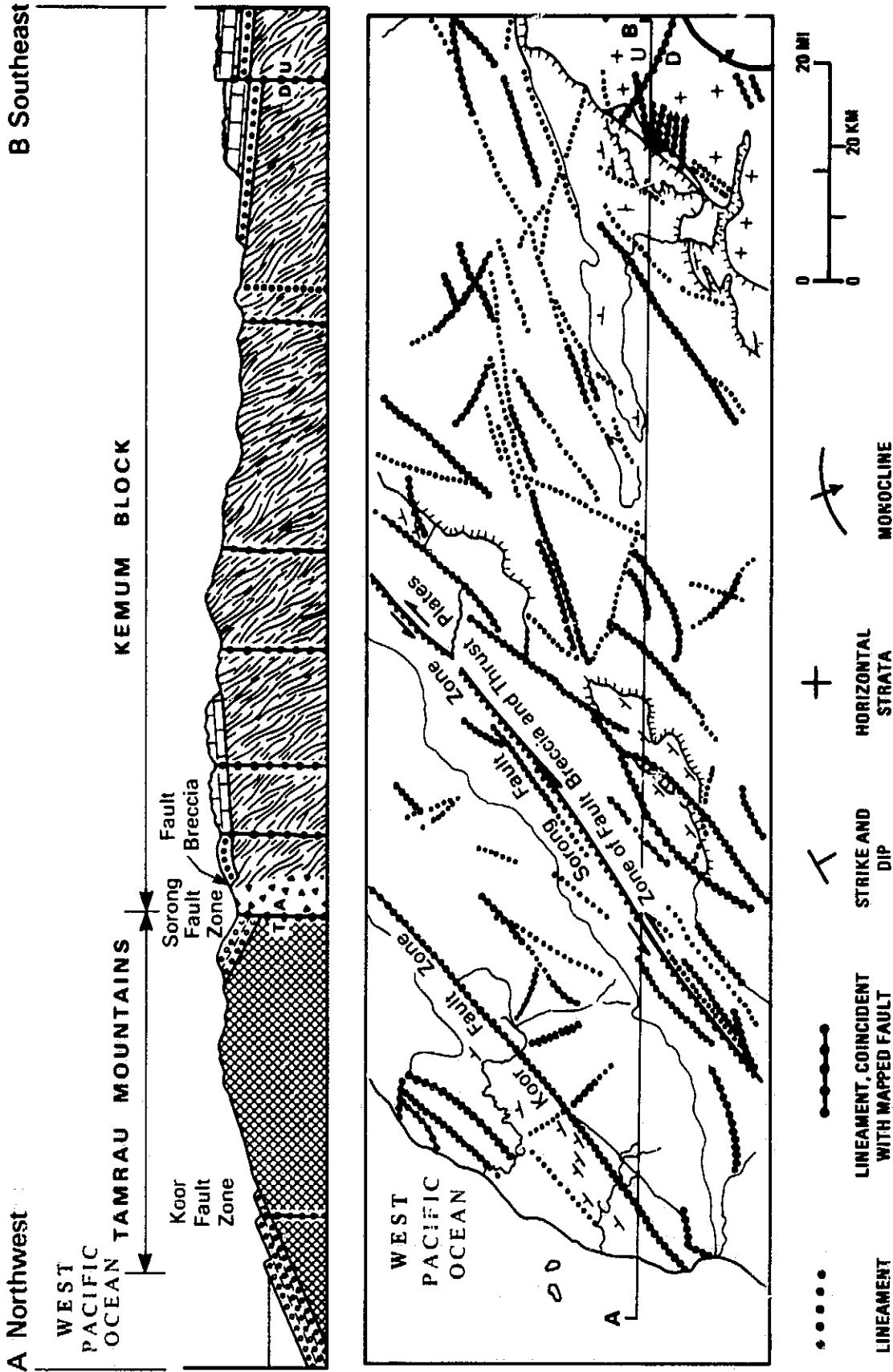
Fig. 3. Structural map and cross section interpreted from SIR-A image of northwestern Vogelkop region. From Sabins (1983, Fig. 11).

SUBSURFACE GEOLOGY OF THE WESTERN DESERT IN EGYPT AND SUDAN REVEALED BY SHUTTLE IMAGING RADAR (SIR-A)

C. S. Breed, G. G. Schaber, J. F. McCauley, and M. J. Grolier
U. S. Geological Survey, Flagstaff, Arizona

C. V. Haynes
University of Arizona, Tucson, Arizona

C. Elachi and R. Blom
Jet Propulsion Laboratory
California Institute of Technology
Pasadena, California

B. Issawi
Egyptian Geological Survey and Mining Authority, Cairo, Egypt

W. P. McHugh
GAI Consultants, Pittsburgh, Pennsylvania

Radar images from the SIR-A experiment carried by the Space Shuttle Columbia (November 1981) revealed a buried topography of integrated stream valleys and bedrock structures concealed beneath the Selima Sand Sheet, dunes, and drift sand of the Sahara in southern Egypt and northern Sudan. Radar responses from bedrock, talus slopes, boulder-gravel terraces, and alluvial fill delineate patterns of large and small, regional and local relict drainage systems. Some of the larger valleys are as broad as the Nile Valley 1000 km to the east but flowed to the south and west, opposite to the present regional gradient in Egypt. The master streams could be as old as middle Tertiary whereas the narrower wadis, many superimposed on the major valleys, represent recurrent later episodes of local running water, probably during Quaternary pluvial intervals. At present, running water is absent, and these ancient streamcourses lie within the $1,234,000$ $-km^2$-area hyperarid core of the driest region on Earth. The present surface consists of extremely dry unconsolidated sand that supports no vegetation except for a few isolated tamarisk mounds and palmtree and grass oases fed by near-surface ground-water. Neolithic people abandoned this increasingly arid region about 5000 years ago, and it remains uninhabited today.

Field investigations at key sites along the SIR-A path in February and September 1982, and in March 1983, confirm that the radar imaging of concealed topographic and geologic features results from penetration of the SIR-A 24-cm-wavelength signal through the "low-loss" surficial sediment to subjacent backscattering materials. Observations at selected localities where the SIR-A images show various signal responses indicate that the depth of these radar discontinuities ranges from a few tens of centimeters beneath sand-sheet deposits and semiconsolidated alluvium to 2 m or more under extremely loose dry dune sand. Radar penetration of dry sand and soils varies with the wavelength of the incident signals, the incidence angle, and the electrical properties of the materials, which are largely determined by moisture content. The calculated depth of radar penetration of dry sand and sandy alluvium, based on laboratory measurements of the electrical properties of samples collected in Egypt and Sudan, is between 1 and 5 m.

Numerous test pits were dug to verify and measure the depths of SIR-A signal penetration. On the Limestone Plateau of Egypt, drift sand obscures the surface on Landsat images but is essentially transparent to the SIR-A signal (Fig. 1a, b). Radar penetration to depths of at least 1.1 m through dry sand and fine pebble alluvium to the rough, wind-eroded bedrock surface of the plateau resulted in radar echoes from the buried limestone nearly as bright as those from bare outcrops nearby. Numerous observations in the Selima Sand Sheet west of the Limestone Plateau confirm that the varying thickness of the sand cover over the backscattering rocky substrate corresponds to the degree of brightness and mottled texture observed on SIR-A images of this region.

"Radar units," based on the degree of brightness and mottling on the SIR-A images, correspond to specific types of terrain units (thick and thin sand cover, alluvial valleys, talus slopes, isolated hills) and bedrock (wind-fluted limestone, granite, and sandstone knobs). "Radar valleys" not evident on the ground or on Landsat images (Fig. 2a, b) were first located in the field by dead reckoning with compass and odometer and occasional landmark recognition, and later by a portable satellite navigation device. Many of the test pits in these buried valleys revealed deposits of stream-worn, rounded-pebble alluvium concealed beneath a veneer of 2-20 cm of windblown sand. In some places, the blanketing Selima Sand Sheet was more than 1 m thick and alluvium was not reached in the pits. In two of these dry valleys, marked by alined tamarisk mounds, wet sand was found at depths of 1 - 3 m.

In several of the valleys examined, artifacts ranging in age from Ascheulean (at least 200,000 years old) through Middle Paleolithic (about 50,000 years old) to Neolithic (about 6000 years old) were found, some tumbled and stream worn within the river sediment. These artifacts indicate that the newly discovered river valleys were favored sites for human occupation during episodes of less aridity than the present. A correlation of known archae- ologic sites with the mapped locations of the streamcourses is expected and may lead to new interpretations of early human history in the Sahara. The valley networks, faults, and other subjacent bedrock features mapped on the SIR-A images are promising areas for ground-water and mineral exploration. Additionally, the analogies between the interplay of wind and running water in the geologic history of the Sahara and of Mars are strengthened by the SIR-A discoveries of relict drainage systems beneath the eolian veneer of Egypt and Sudan.
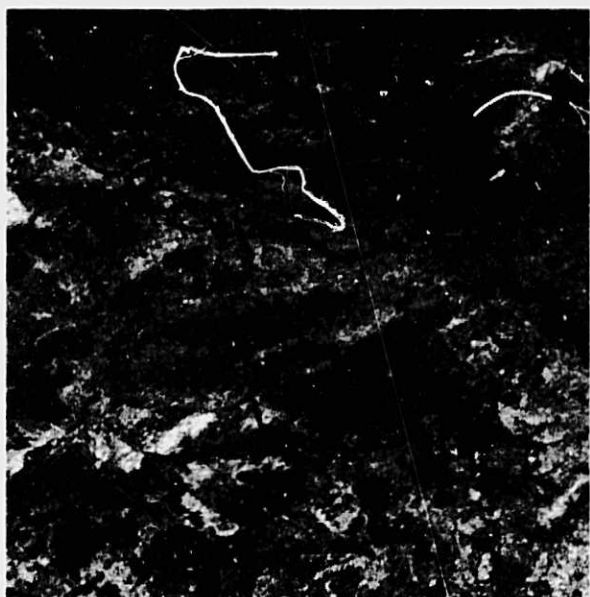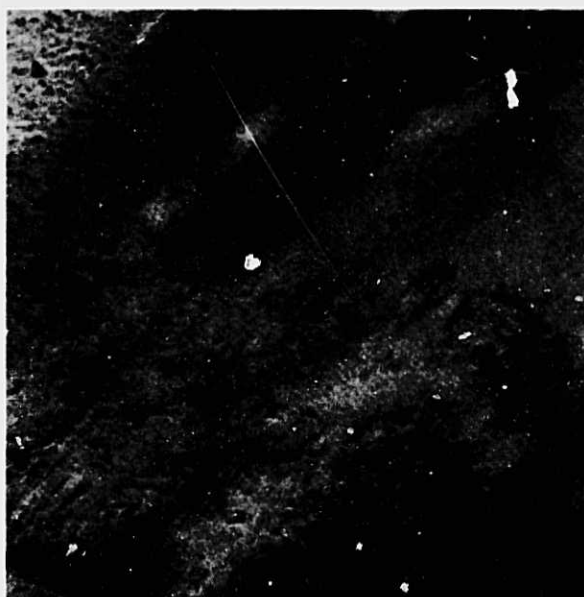
11
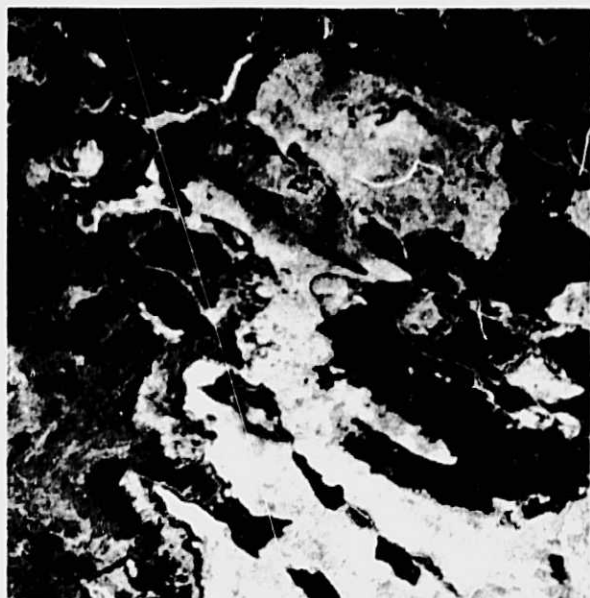
(a) (b)

Fig. 1.   Radar image (a) showing bright response from wind-eroded limestone concealed by drift sand on the Landsat image(b).

(a) (b)

Fig. 2.   Radar image (a) revealing braided network of stream channels in broad valley concealed by the Selima Sand Sheet on the Landsat image (b).

USE OF COREGISTERED RADAR, VISIBLE AND IR IMAGES
FOR GEOLOGIC REMOTE SENSING

Diane L. Evans
Jet Propulsion Laboratory, California Institute of Technology
Pasadena, California

In November 1981 the Shuttle Imaging Radar (SIR-A) obtained images over the southern portion of the San Rafael Swell in eastern Utah (Fig. 1). The SIR-A swath covered part of the area studied by Blom, et al. [1], Blom and Daily [2], using combined Seasat SAR and Landsat MSS images, and Kahle, et al. [3], using thermal inertia data from the Heat Capacity Mapping Mission (HCMM). The addition of SIR-A data to the image data set described in these studies provides a unique opportunity to compare radar images obtained with different incidence angles and different illumination directions with images obtained in other portions of the spectrum for geologic remote sensing.

System characteristics for Landsat, Seasat, SIR-A, and HCMM are shown in Table 1. Briefly stated, the scattering for the SIR-A geometry is dominated by surface roughness at the scale of the radar wavelength, although there is some contribution from vegetation. For the Seasat SAR geometry, surface slopes have a dominant role, and topography is strongly highlighted. Images acquired by the Landsat MSS are sensitive to compositional variations in surface materials, while thermal inertia images are sensitive to surface and bulk thermal properties.

The image data set over the southern portion of the San Rafael Swell was coregistered by finding common tie points in the Seasat, Landsat HCMM and digitized SIR-A images, and a digitized geologic map, and rotating and sizing each of the images to the map base. All images were resampled to Landsat resolution to facilitate computation. Examples of the registered image data set are shown as Fig. 2.

Lithologic units can be differentiated visually to varying extents in the images shown in Fig. 2. For example, the Moenkopi Siltstone is much more distinctive in the Landsat and Landsat ratio images than in the HCMM or radar images, indicating that the albedo, or composition, of the unit is more diagnostic than its texture. On the other hand, texture is an important factor in recognizing units such as the Tununk Shale, which looks very different in its two exposures on the Landsat and Landsat ratio images. Both outcrops of the Tununk Shale have a similar appearance on the SIR-A and Seasat images, however, because the outcrop pattern and the surface roughness are similar in both exposures of the unit. The two exposures of the Tununk Shale can also be differentiated as areas of low thermal inertia in the HCMM image, owing to the unconsolidated nature of the unit [3]. The two outcrops of the massive Navajo Sandstone are also more easily recognizable as the same unit in the HCMM image than in the other images, owing to the high thermal inertia of the unit [3].

The value of multisensor image data sets is borne out quantitatively using computer classification techniques. Using procedures such as Linear Discriminant Analysis (LDA), it is possible to determine the relative importance of each sensor in discriminating geologic units (e.g., [1,2]).

Results of the analysis showed that maximum discrimination of the nine units listed in Fig. 2 was achieved using Landsat Band 4 (MSS4), the ratio of Landsat Band 4/Band 5 (R4/5), HCMM, and SIR-A. As would be expected, some units, such as the Moenkopi Siltstone were accurately classified based on MSS4 and R4/5 alone. However, for most units, the combined data set improved classification accuracy significantly. For example, the addition of HCMM increased classification accuracy of the Carmel Limestone 31% and the addition of SIR-A further increased the accuracy 11%.

The significance of these results goes beyond the increased ability for rock type discrimination. The implication is that multisensor images provide information about intrinsic physical properties required for identification of surface types. Spectral signatures of the units in this area, derived from radiometric values for corresponding pixels in the coregistered images, show that the rocks have unique signatures when all of the wavelengths are included. The spectral resolution provided by the Thematic Mapper on Landsat 4 will provide increased compositional information required to identify some rock types. The increase in textural and backscatter information provided by multi-incidence angle radars such as SIR-B will further improve characterization of units with ambiguous signatures in the visible and near-infrared.

ACKNOWLEDGMENTS

REFERENCES

[1] Blom, R., Abrams, M., and Conrad, C. (1981) IGARSS '81, 597-602.

[2] Blom, R., and Daily, M. (1982) IEEE Transactions on Geoscience and Remote Sensing, GE-20, 343-351.

[3] Kahle, A. B., Schieldge, J. P., Abrams, M. J., Alley, R. E., LeVine, C. J. (1981) JPL Pub. 81-55.

[4] Hintz, L. F., and Stokes, W. L. (1964) Geologic Map of Southeastern Utah, Utah State Land Board.

[5] Smith, J. F., Huff, L. C., Hinrichs, E. N., and Luedke, R. G. (1963) U.S.G.S. Prof. Paper 363.

Table 1. System characteristics

	Seasat	SIR-A	HCMM	Landsat
Satellite altitude	800 km	257 km	620 km	920 km
Swath width	100 km	50 km	716 km	185 km
Wavelength	23.5 cm	23.5 cm	10.5-12.5 μm	0.5-1.1 μm
Resolution	25 m	40 m	0.6 km	80 m
Antenna nadir angle	20 deg	47 deg	0 deg	0 deg
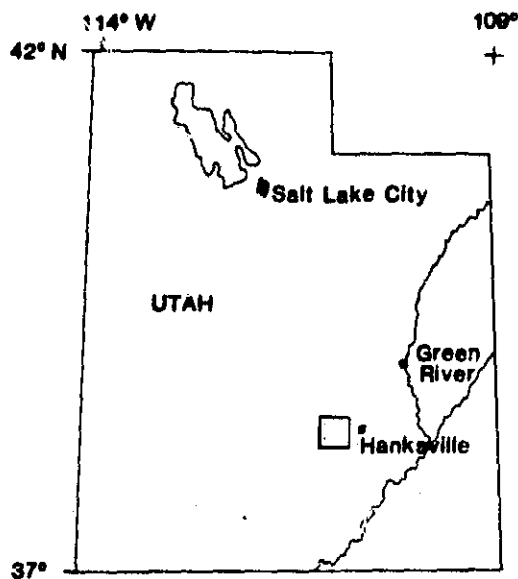
Fig. 1. Location of the study area shown as the stippled square west of Hanksville, Utah. The area includes portions of the San Rafael Reef and Capitol Reef which are made up of continental and marine sediments that were uplifed and folded in the Cretaceous [4,5].

0   25 km   ↑N

1) Kaibab Limestone   4) Saltwash Sandstone   7) Tununk Shale
2) Moenkopi Siltstone   5) Blue Gate Shale   8) Entrada Sandstone
3) Navajo Sandstone   6) Ferron Sandstone   9) Carmel Limestone
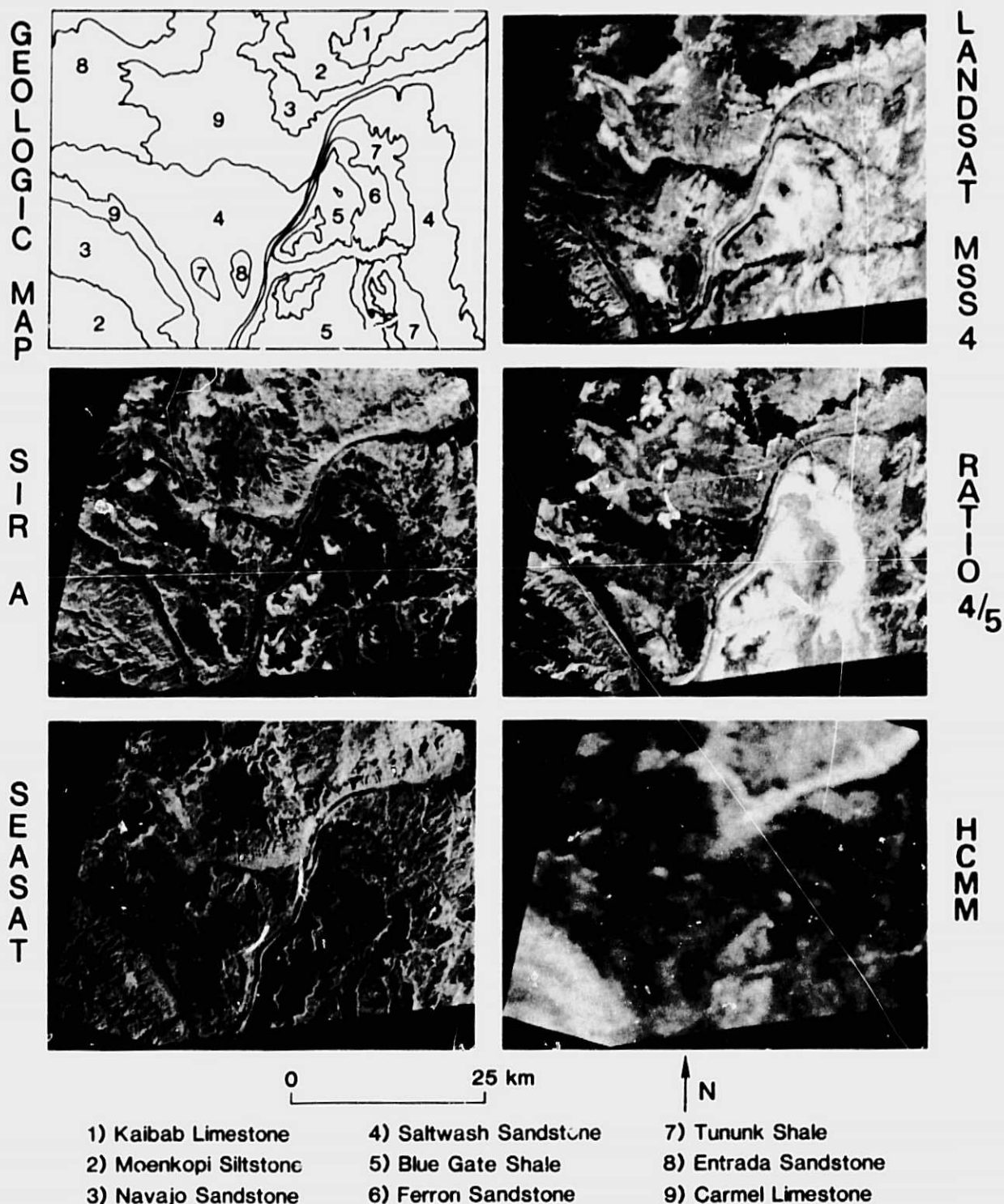
Fig. 2.   Coregistered image data of the study area. SIR-A data take 24B
(3 Nov. 1981), Seasat Rev. 789 (21 Aug. 1978), Landsat frame
#1068-17364 (29 Sept. 1972). HCMM is a thermal inertia image
calculated from frame #AA0124204802 (27-28 Aug. 1978) [3], R4/5
is the ratio of Landsat MSS4/MSS5.

16

Sensors and Antenna Technology

SPACEBORNE SAR SENSOR ARCHITECTURE

Keith R. Carver
Engineering Research Center
New Mexico State University
Las Cruces, New Mexico

I. INTRODUCTION

Spaceborne imaging radars for the decade of the '90s will be called upon to provide increased illumination parameter flexibility, polar orbital coverage, and to operate from the same platform with other advanced sensors such as multi-linear arrays. The potential information content in accurately merged microwave-infrared, or microwave-visible images is enormous by comparison to either radar images alone or visible/infrared images alone, since microwave images are principally responsive to surface geometry whereas visible/infrared images are highly sensitive to surface chemistry.

This paper discusses a strawman system concept in which a SAR and multilinear array (MLA) are flown on a polar-orbiting free-flyer at 800 km altitude. Data would be relayed to ground via the TDRSS (or equivalent).

Although the potential information content in accurately merged SAR-MLA images is great, two major problems must be faced:

(1)   The SAR looks off to the side of the satellite nadir ground track (e.g., 20-60°) whereas the MLA looks at or near the nadir ($\pm 20°$). Thus, in order to obtain simultaneous SAR and MLA imagery, two spacecraft would be required. Practically speaking, this is probably too expensive. A more realistic approach is to abandon the requirement for exact simultaneity of the SAR and MLA images, in favor of waiting a day or so for the MLA swath to drift into alignment with the previous day's SAR swath, as suggested in Fig. 1.

(2)   Both the SAR and the ML have high data rates. The MLA rate may exceed 200 Mbits/sec and the SAR rate can be as high as 200 Mbits/sec if the images are digitally correlated by a ground processor. One possible solution is to use a real-time on-board correlator for medium-resolution (100 m) survey mode SAR imagery, with high-resolution imagery (e.g., 20 m resolution) being processed by a ground processor on a delayed-time basis. This could reduce the survey-mode SAR data rate to about 10 Mbits/sec or less. High-resolution SAR imagery would be acquired when the MLA was turned off.

As a starting point in the SAR design, it is desirable to acquire multiwavelength and multiple incidence angle imagery; if possible, it would be desirable to acquire like (HH and VV) as well as cross-polarized (HV) imagery, transmit power permitting. Three frequencies (L-, C-, and X-bands) and three discrete incidence angles (20°, 40°, and 55°) will be specified along with a 150-km minimum swath width. A 10-dB SNR will be specified at the swath center; the noise includes thermal, distortion and ambiguity noise.

19

II. ANTENNA SIZE

Using an 800-km altitude and ambiguity safety factors of 1.3 in range and azimuth, a minimum antenna area may be calculated which avoids ambiguities (see Fig. 2). By making the antenna 20 m in length, an antenna height may then be specified. For each frequency, the aperture is divided into three subapertures, as suggested in Fig. 3. By orienting the beam in elevation (range) to a look angle of 35° (broadside to the array), an incidence angle of 40° is obtained. If the beam is then electronically steered to a 20° look angle or a 47° look angle, low-angle mode (22° incidence angle) or high-angle mode (55° incidence angle) coverage is obtained. As an example, for the low-angle mode at L-band, only 1 m of the aperture height is excited; for the medium-angle mode, 2 m would be used and for the high-angle mode, 3 m would be used. A similar approach would be used at C-band and X-band.

The SNR-limited swathwidth thus obtained would be 220 km for the low-angle mode, 115 km for the medium-angle mode and 150 km for the high-angle mode. Table 1 summarizes the antenna dimensions, area, minimizing required area and gain for each frequency and incidence angle. Note that the antenna area for the high-angle mode is not quite enough to achieve good ambiguity suppression over the 150 km swath.

It is also necessary to keep the antenna electrically flat over its 20-m length. The worst problem is at X-band, for which a 5-mm peak-to-peak flatness is required to reduce beam tilts or drifts and gain fluctuations to an acceptable level.

III. TRANSMIT POWER

The average transmit power required increases as the cube of the range-frequency product and inversely with the radar backscattering coefficient. The greatest power is therefore required for the high-angle mode. To estimate this power, a 10-dB SNR is used (beam center), a 60% antenna aperture efficiency, a 3-dB receiver noise figure, 4-dB system losses and a 20-m range resolution. The backscattering coefficient σ^O is assumed to be -25 dB at L-band and -20 dB at both C-band and X-band, all for a 55° incidence angle. With these assumptions, and a 4% duty cycle, the required average and peak power levels are summarized in Table 2.

With the current state of the transmitter art, solid-state amplifiers are available at L-band which can be paralleled to produce several hundred watts average power. However, at C-band and X-band, TWT or klystron amplifiers are required to achieve these power levels.

The dc-to-rf power efficiency and available gain are key factors in the design of a transmitter system, especially at C-band and X-band where some tens of kilowatts peak power is required. At X-band, TWT amplifiers are available for aircraft or ground radars which can deliver 40-50 dB gain at efficiencies from 30%-40%, at the 10-15 kW power level shown in Table 2. The challenge for TWT amplifiers is to develop space-qualified units which are light weight and reliable over the projected 3-5 year lifetime of the satellite.

20

An alternate approach is to use combined solid-state amplifiers. Although these are available at L-band (and were used on Seasat and SIR-A), X-band units are currently restricted to average output power levels of about 2 watts and have dc-to-rf efficiencies of less than 25%. For the strawman SAR of this paper, it would be required to parallel about 275 such units, which would then consume 2.2 kW prime dc power! If the power output per unit can be increased to 10-20 W and the efficiency raised to 50%, solid-state units (either hybrid or monolithic) will become more attractive for X-band SAR application.

IV. DISTRIBUTED SAR DESIGNS

One possible SAR design approach is to distribute the high-power amplifiers (HPA) of the transmitter and the low-noise amplifiers (LNA) of the receiver over the antenna array grid. At first blush, this could potentially give increased control over the SAR, improve reliability, and possibly improve the efficiency.

If phase shifters are used to electronically steer the beam in range, then only one phase shifter is needed for each array row (20 m long). Assuming the design shown in Table 1, about 30 rows of elements are required, each with its own phase shifter. Since the phase shifter is likely to be the lossiest (typically 2 dB) element in the transmission line feed network, it is desirable to place it at a point where the rf power level is low, i.e., before the HPA units. This can increase the rf efficiency (rf power out/rf power in) by several percent.

One difficulty with distributed amplifiers is in the total efficiency (rf power out/dc power in) of a network of solid-state amplifiers as opposed to a "big-bang" design using a single space-qualified TWT. Using the current state-of-the-art, the distributed solid-state array is at least 15% less efficient than the TWT design. Another difficulty may be in heat dissipation from the distributed HPA units.

V   IMAGE PROCESSING

If a ground processor is used to correlate 6-bit data into 4-look images, then assuming a 1500 Hz PRF and a 150 km swath width, the data rate would be about 150 Mbits/sec. This high data rate may be incompatible with simultaneous transmission of MLA images which also generate high data rates.

One alternative may be to design an on-board survey mode processor which transmits 100-m-resolution fully correlated images, thus reducing the SAR data by an order of magnitude. With 100 m resolution and 4 looks, such a correlator would require 1000 FFT processors and only one azimuth reference function per look. With a 12-bit complex word length, the size of the azimuth compression memory would be 18 Mbits at L-band, 3 Mbits at C-band and 1 Mbits at X-band.

With current IC technology and CCD memory, roughly 10,000 - 20,000 equivalent IC's would be required for such a correlator, which would consume several kW (2-5 prime power. If the promise of VHSIC technology is realized,

then by the mid- or late-'80s, it may be possible to drastically reduce the prime power and weight of such a device, thereby making such an on-board cor- relator feasible.

VI. SUMMARY

In conclusion, it appears possible to design a multi-parameter SAR which can be operated from the same platform as an MLA imager. This would require a 20-m-long antenna array with a total height of 4.8 m, assuming that separate apertures were used for L-band, C-band, and X-band. The greatest transmit power would be required at X-band, and would range from 10-30 kW peak. With current technology, the X-band power source would be a space-qualified TWTA, and would demand 1-3 kW prime power. A distributed solid-state SAR would increase this prime power by at least 15%, but would offer the advantage of graceful failure and increased reliability.

It appears very unlikely that such a system could be used effec- tively for cross-polarized (HV) imagery for the high-angle mode at either C-band or X-band, since the required transmit power levels would increase by a factor of 5 to 10. This is unfortunate, since the HV backscattering appears to be strongly related to volume scattering and would thus be valuable for vegetation discrimination and geological mapping.

Specific technology studies should be undertaken in the following areas:

(1) Antennas. Development of 20 m x 4 m planar arrays of microstrip elements vs waveguide slot elements.

(2) Transmitter. Development of C-band and X-band 10-20 W solid-state amplifiers with 40% - 50% efficiency.

(3) Processor. Development of on-board survey mode processors using either VHSIC or hybrid technologies.

Table 1. Antenna size

Frequency (angle)	Length, m	Height, cm	Area, m^2	Min. area, m^2	Gain, dB
L-band (1.275 GHz)					
Low-angle	20	100	20	14.6	34.2
Med-angle	20	200	40	33.6	37.4
High-angle	20	350	70	73.4	39.0
C-band (5.3 GHz)					
Low-angle	20	24	4.8	3.5	40.4
Med-angle	20	48	9.6	8.1	43.5
High-angle	20	85	17.0	17.7	45.2
X-band (9.6 GHz)					
Low-angle	20	13	2.6	1.9	43.0
Med-angle	20	26	5.2	4.5	46.1
High-angle	20	46	9.2	9.8	47.8

Table 2. Transmit power

σ^0 = -25 dB (L-band), -20 dB (C-band), -20 dB (X-band)

Angle of incidence = 55°

Duty factor = 4%

Frequency	Average power, W	Peak power, kW
L-band	240	6
C-band	315	8
X-band	550	15
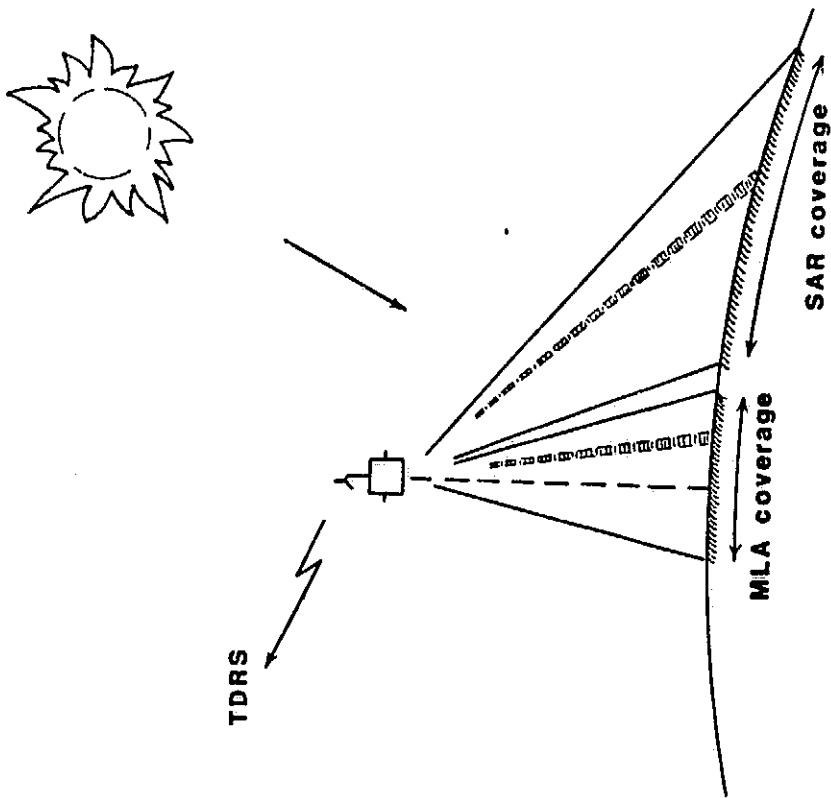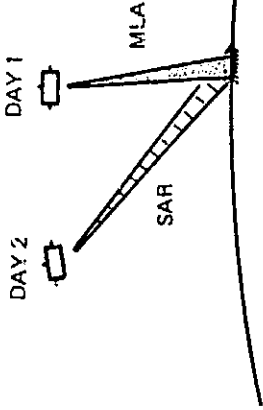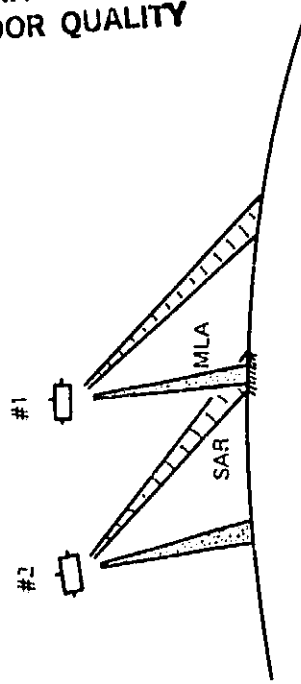
Fig. 1. SAR and MLA coverage limits (left); two means
for aligning SAR and MLA swaths (right).

ARRAY CONFIGURATION

- Planar array, electronically steered in elevation
- Electronic correction of non-flat antenna

L-band Patterns
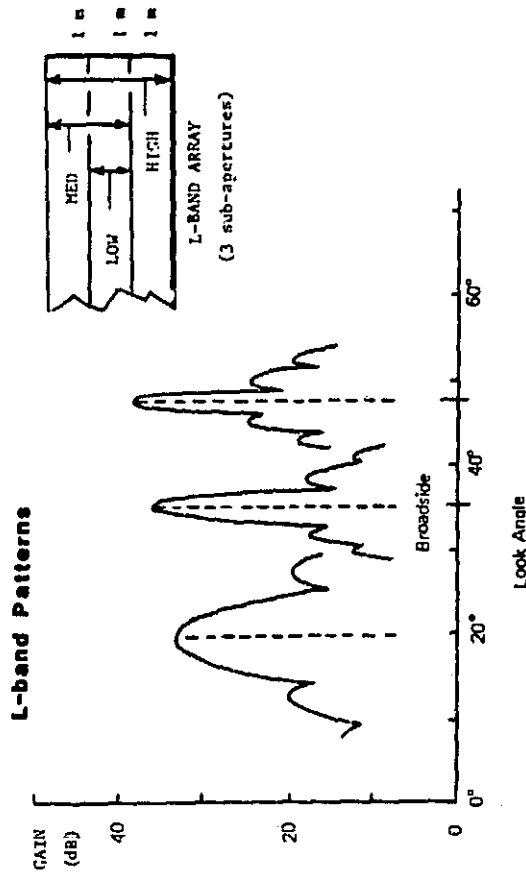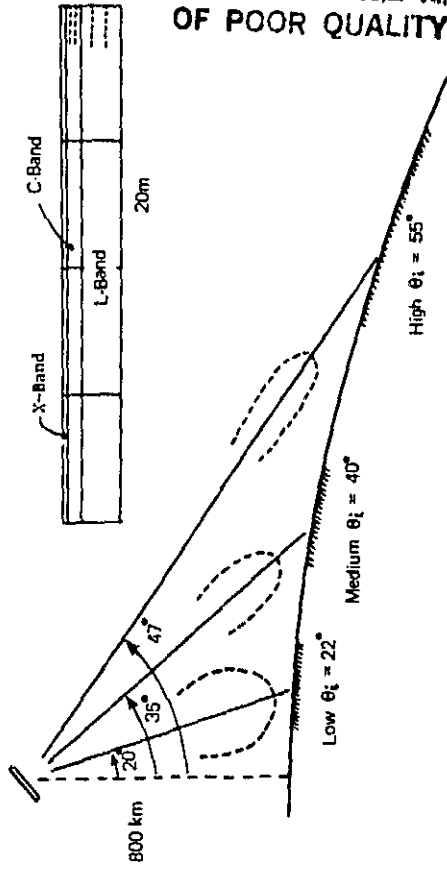
Fig. 3. Planar array concept with elevation beam steering (top); subaperture array design at L-Band (bottom).

MINIMUM ANTENNA AREA

- Altitude = 800 km
- Doppler sampling safety factor = 1.3
- Range safety factor = 1.3
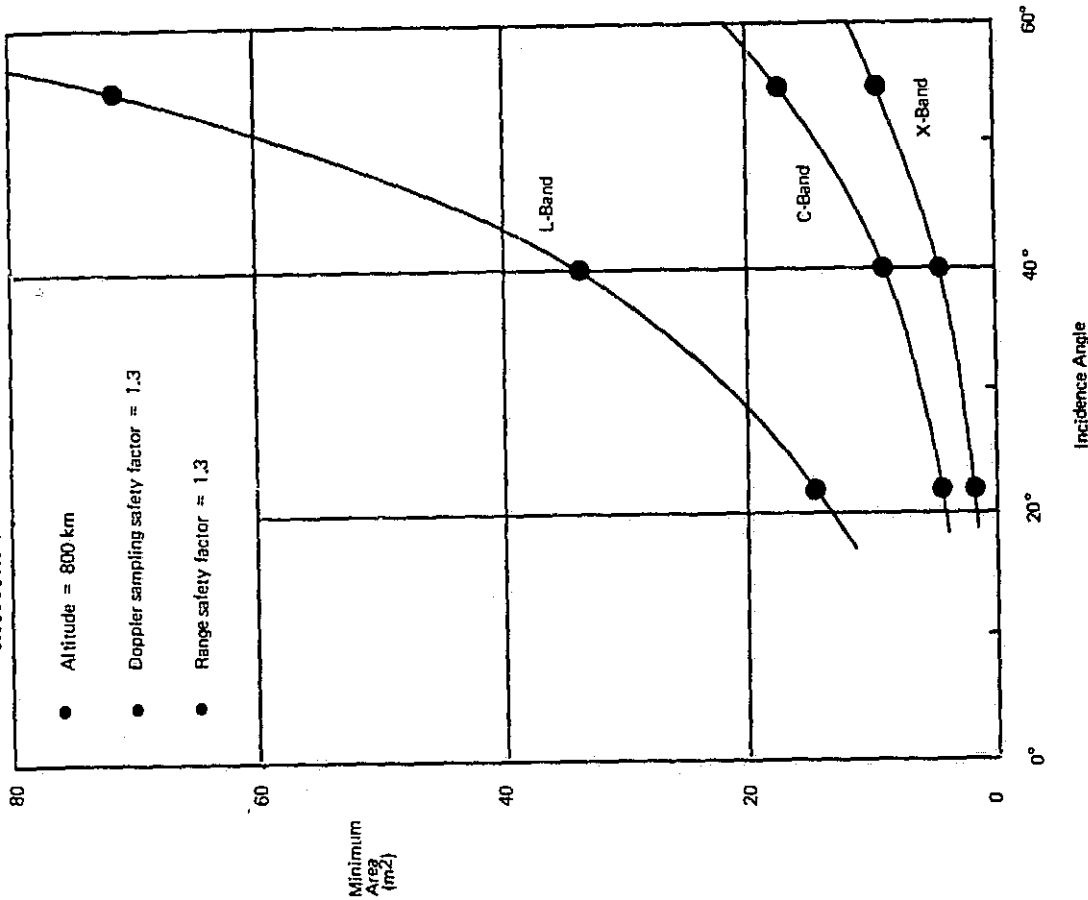
Fig. 2. Minimum antenna area necessary to avoid ambiguities.

25

SHUTTLE IMAGING RADAR - A/B SENSORS

James L. Granger
Jet Propulsion Laboratory
California Institute of Technology
Pasadena, California

I. INTRODUCTION

The exciting discoveries of the Shuttle Imaging Radar-A (SIR-A) experiment have prompted a refly of the instrument to be designated the Shuttle Imaging Radar-B. The SIR-B instrument will reuse the hardware flown for the SIR-A mission and add some interesting refinements. This paper describes the two radar sensors in detail.

The SIR-A and SIR-B instruments are both tailored for use on the space shuttle. They are physically configured to fit in the Shuttle's payload bay, are powered and cooled by shuttle systems, are controlled by the crew or from the ground, and record data on board or beam it to the ground using the orbiter's data links. The radars are designed to accommodate a range of orbiter altitudes and have built-in operating modes to cover a wide variety of mission objectives. The flexibility and utility of these radars make them ideal, cost-effective instruments for research in the space shuttle environment.

II. THE SIR-A SENSOR

The SIR-A instrument was based on the design of the Seasat imaging radar. Many of the subsystems flows in the SIR-A instrument were Seasat engineering models upgraded to flight quality. A block diagram of the flight radar system is shown in Fig. 1. Key parameters of the flight system are given in Table 1.

A linear-FM pulse is generated in the transmitter by gating a portion of the sinewave signal from a stable local oscillator (STALO) and passing it through a surface-acoustic-wave (SAW) dispersive delay line. The pulse is upconverted to L-band using a two-stage process to eliminate unwanted sidebands and mixing products. The L-band pulse is amplified by three, parallel, solid-state driver and power amplifier stages and combined at the output to produce approximately 1100 watts peak. The output is applied to the antenna through a ferrite circulator that acts as a transmit/receive diplexer.

Return echoes from the antenna are routed through the circulator to the input of the receiver, where they are filtered and amplified. The receiver's input contains a high-power, PIN-diode switch that disconnects the input of the receiver from the circulator during the transmit event, thereby preventing accidental damage to the sensitive circuits of the first amplification stage.

Prior to down-conversion, received echoes pass through a variable-gain amplifier for sensitivity time control (STC). The gain of the amplifier is controlled with a high-speed waveform that compensates for the shape of the

antenna pattern in range. The noise bandwidth of the receiver is set in the first IF with a special linear-phase bandpass filter. A second mixing operation converts the signal to video frequencies for optical recording.

The antenna is a 9.4 x 2.16 meter printed-circuit planar array fixed at one pointing angle. The radiating elements of the antenna are etched on copper-clad, fiberglass-epoxy sheets which are stiffened with a light-weight, honeycomb backplane. The antenna consists of seven separate panels that are summed together using a network of coaxial cables and power combiners.

The optical recorder used a prototype left over from the Apollo 17 Lunar Sounder program. The recorder was thoroughly refurbished and modified to provide a greater bandwidth and recording capacity than the Apollo design. It contained 3600 feet of 70mm film that allowed 8 hours of recording time.

The antenna, electronics package and optical recorder were mounted on a Spacelab pallet as shown in Fig. 2. The antenna was mounted to four hard-points on the pallet using a trusswork of aluminum tubing. The electronics was mounted below the antenna on a platform containing a Freon cooling system. The optical recorder was mounted on a shelf across the pallet from the antenna. The entire pallet assembly fit inside the shuttle's payload bay and was within the envelope of the closed bay doors.

III.   THE SIR-B SENSOR

The SIR-B sensor utilizes all of the subsystems flown for the SIR-A experiment and adds a movable antenna for variable look-angle experiments and a digital system for transmitting data to the ground. The SIR-B hardware will be placed on a Spacelab pallet, as shown in Fig. 3, and flown with deployable payloads on flight number 17. Key parameters of the SIR-B system are given in Table 1. A simplified block diagram is shown in Fig. 4.

The antenna's construction will be similar to that employed for SIR-A. An additional panel will be added for a total of eight. Because of the deployable payloads, the antenna must be folded to keep its physical dimensions within the confines of the pallet for launch. After the deployables are placed in orbit, the antenna will be unfolded and tilted to the desired viewing geometry. During the flight, the antenna can be tilted to any angle between 15° and 60° from nadir.

The digital data handling subsystem (DDHS) will allow real-time recording on the ground of unprocessed radar signal data. The video signal to the optical recorder will be split at the output of the receiver with one channel continuing to the optical recorder and the other to the DDHS. At the DDHS the signal is digitized with a high-speed, 6-bit ADC and applied to a ping-pong memory. While one range line of data is being stored into half of the memory, the other half, containing the previous range line, is being dumped to the Ku-band data link of the orbiter. The Ku-band signal is relayed through a Tracking and Data Relay Satellite (TDRS) to a receiving station at White Sands, New Mexico, then, transferred via DOMSAT to recording stations at the Goddard Space Flight Center and the Johnson Space Center. Real-time recording of digitized data will be possible only when the orbital geometry allows the shuttle's Ku-band link to access a TDRS satellite. The on-board optical recorder will allow recording anytime during the flight.

The digital recording capability, along with an increased bandwidth, will allow higher-resolution imagery than was achievable for the SIR-A mission. Where the resolution for SIR-A was 40 meters in range and azimuth, the resolution for SIR-B will be 18 to 55 meters in range (depending on look angle) and 25 meters in azimuth. The digital recordings are expected to add approximately 25 hours of data to the SIR-B mission on top of the 8 hours of optical recordings.

ACKNOWLEDGMENT

Table 1. SIR-A/B sensor characteristics

| Parameter	SIR-A	SIR-B
Transmitter power	1100 W peak	1100 W peak
Modulation	Linear FM pulse	Linear FM pulse
Pulse width	30.4 μs	30.4 μs
Center frequency	1278.4 MHz	1282.0 MHz
Bandwidth	6 MHz	12 MHz
Receiver noise temp	826° K	848° + 50° K
Receiver gain	80-101 dB	56-10$\overline{1}$ dB
Antenna size	9.4 x 2.16 m	10.7 x 2.16 m
Antenna gain	33.6 dB	33.0 + 0.3 dB
Antenna pointing	Fixed, 47° to nadir	Variable, 15-60° to nadir
Recording	Optical	Optical and digital
Bit rate	N/A	45.5 Mbps
Data processing	Optical	Optical and digital
Range resolution	40 m	18-55 m
Azimuth resolution	40 m	25 m
Number of looks	6	4
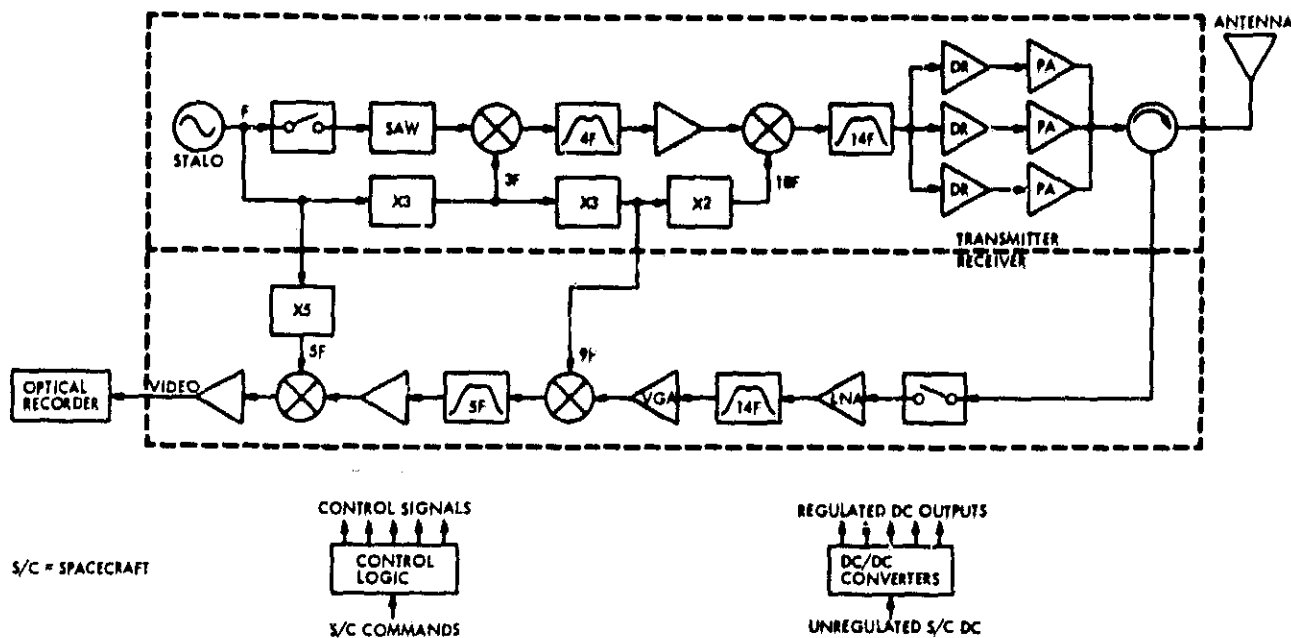
Fig. 1.   SIR-A flight sensor block diagram.
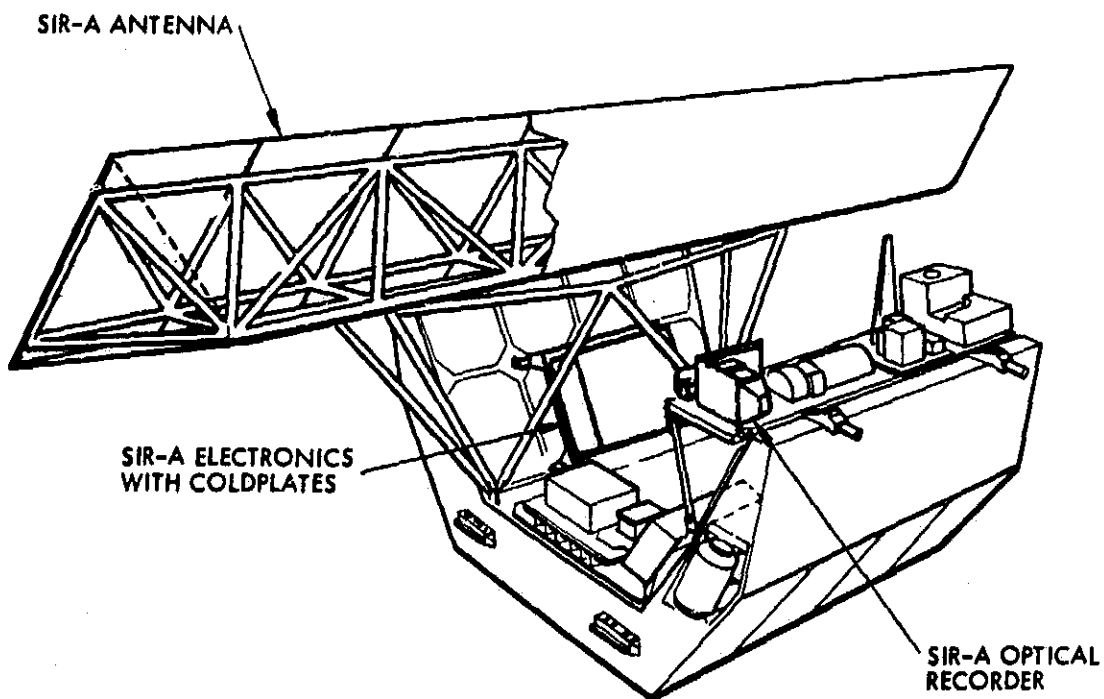
Fig. 2.   The Office of Space and Terrestrial Applications - 1 payload
showing placement of the SIR-A sensor hardware.
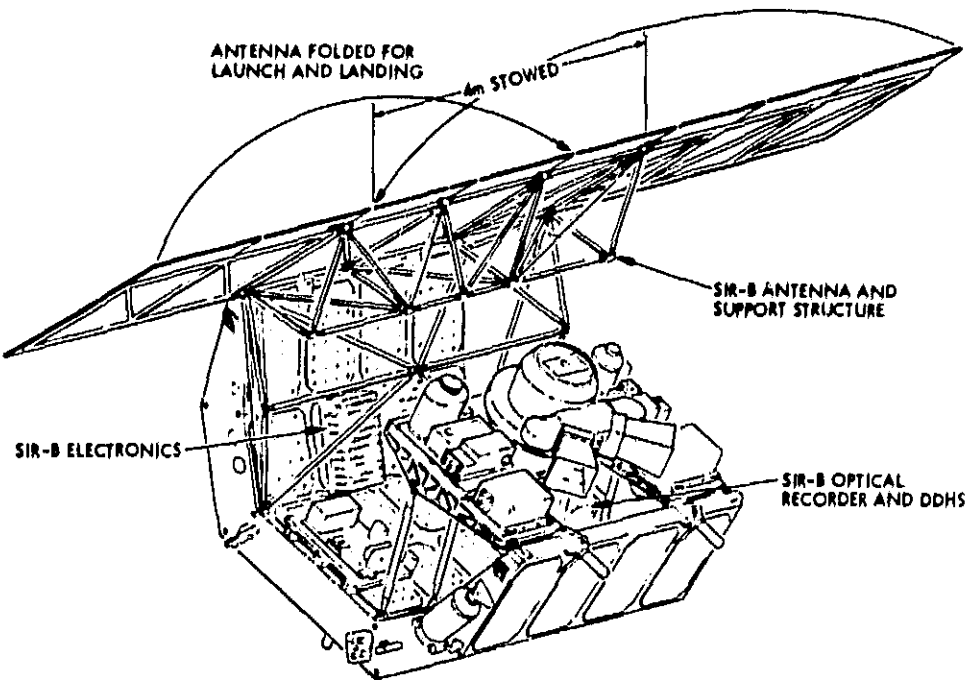
Fig. 3. The Office of Space and Terrestrial Applications - 3 payload
showing placement of the SIR-B hardware. The SIR-B antenna
is shown in its deployed configuration.
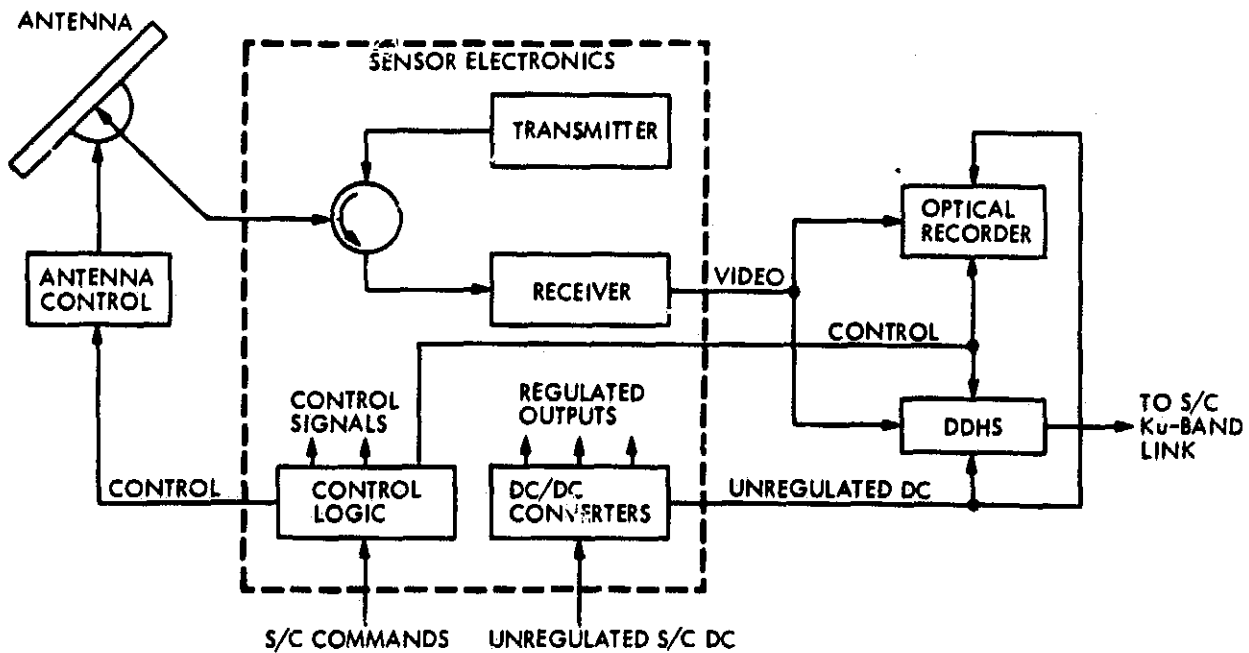
Fig. 4. Simplified SIR-B flight sensor block diagram.

31

MICROSTRIP ANTENNAS FOR SAR APPLICATIONS

Hussain A. Haddad
Ball Aerospace Systems Division
Boulder, Colorado

This paper summarizes current and future microstrip antenna technology development for Spaceborne Synthetic Aperture Radars (SAR). Table 1 shows some of the electrical and mechanical characteristics of previously and presently developed microstrip SAR antennas. The Seasat, the SIR-A and presently the SIR-B antennas are all designed for operation at L-band with approximately 22 MHz of bandwidth. The antennas have linear polarization with minimum of 20 dB of polarization purity. Both the Seasat and SIR-A antennas were designed for a fixed pointing angle of 20.5° and 47°, respectively. However, the SIR-B will have the added feature of mechanical beam-steering in elevation (range).

With the exception of different mechanical characteristics, it can be concluded that present spaceborne SAR antennas have only single-frequency and single-polarization performance. The lack of large spaceborne antennas operating at the higher frequency bands, for example, at C and X bands, stems from: (1) the higher degree of fabrication tolerance required for a given performance; and (2) larger feed and radiating element losses. We believe the mature technology of graphite/epoxy support trusses and glass woven PTFE/honeycomb panel construction offers the good dimensional stability and electrical performance needed for the development of future multifrequency SAR antennas.

In addition to the recent interest in multifrequency spaceborne SAR systems, dual polarization is also of prime importance in SAR sensor applications. Fig. 1 shows a model of a dual polarized C-band microstrip antenna. The measured polarization isolation was better than 30 dB on broadside and 20 dB over ±6° off broadside in three planes (E, H, and 45° planes) over a bandwidth of 100 MHz. This antenna can be extended to an equivalent SIR-A panel size. Note at this frequency band the panel height should be scaled to approximately one-fourth of the standard SIR-A panel height in order to have the same elevation beamwidth. Several panels can be combined as an array by feeding them with thinned-wall rectangular waveguides.

Recently, we have constructed a stacked microstrip antenna with dual frequency (1.25 and 5.3 GHz) and dual polarization. The antenna model is shown in Fig. 2. This design concept involves a multilayer sandwich construction. The top and bottom layers are glass woven PTFE substrates where the C-band microstrip radiating elements and feed systems are etched on. The central layers are two Hexcel honeycomb layers sandwiching an epoxy-glass sheet used for the L-band microstrip circuit feeds. The L and C band radiating patches are fed by spring-loaded pins and short coaxial sections, respectively. This type of stacked construction is slightly more complex than the simpler sandwich construction of the Seasat or SIR-A antennas. However, this design concept represents a near-term realization of a multifunction SAR system.

Another design option is the microstrip SAR antenna with distributed electronic beam-steering network and RF amplifiers. Current technology with three-bit phase shifters using state-of-the-art PIN diodes has over a dB of loss at C and X band. This presumably will make it difficult to operate a large spaceborne SAR without using low noise amplifiers (LNA's) and high power amplifiers (HPA's) near or at the radiating elements level. The hybrid technology as well as the Monolithic Microwave Integrated Circuit (MMIC) technology, where most of the components (phase shifters, LNA's, HPA's, TR switches, etc.) are integrated on or in the same substrate, should offer the future hope for constructing large distributed SAR antennas.

In conclusion, low-loss microstrip antennas are feasible for multifrequency and dual polarization SAR applications. Also, these antennas have the advantage that distributed amplifiers can be easily integrated into their design.

Table 1. Seasat, SIR-A and SIR-B antenna characteristics

	Seasat	SIR-A	SIR-B
Size (deployed)	10.74 x 2.16 m	9.40 x 2.16 m	10.74 x 2.16 m
Size (folded)	1.34 x 2.16 m	-	4.1 x 2.16 m
Weight	103 kg	181 kg	306 kg
Launch vehicle	Atlas/Agena	Space shuttle	Space shuttle
Support structure	Graphite/epoxy 3-dim. truss	Rigid alum. 3-dim. truss	Rigid alum. 2 & 3-dim. truss
Fold mechanisms	Multi-fold (spring-loaded)	Fixed	Two-folds (Motor-driven)
No. of elements	1024	896	1024
No. of panels	8	7	8
Feed network	Suspended substrate	Coax cable	Coax cable
Gain	34.9 dB	33.6 dB	33.0 dB
Polarization	Horiz. linear	Horiz. linear	Horiz. linear
Beamwidths			
H-plane	6.2°	6.2°	6.2°
E-plane	1.1°	1.4°	1.1°
Frequency	1275 MHz	1278 MHz	1282 MHz
Boresight angle	20.5° from nadir	47° from nadir	15°-60° (mechanical steering)
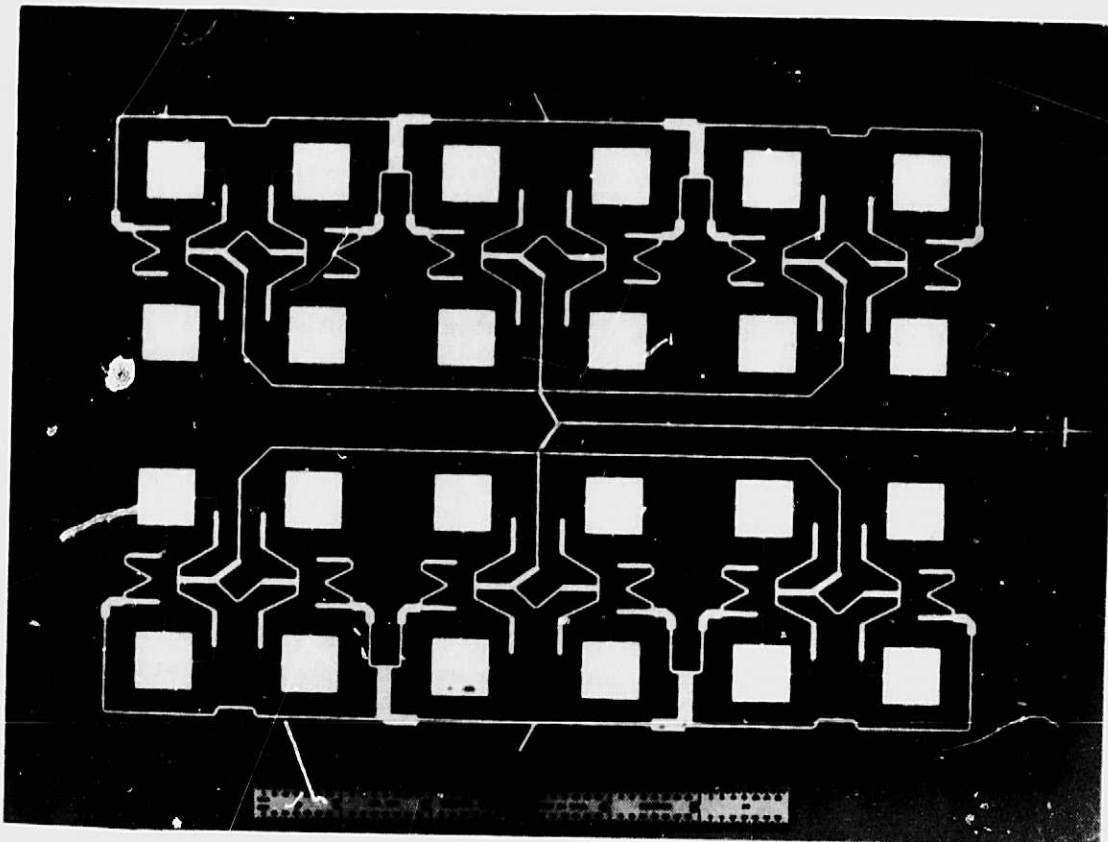
Fig. 1. A model of a dual polarized C-band microstrip antenna.
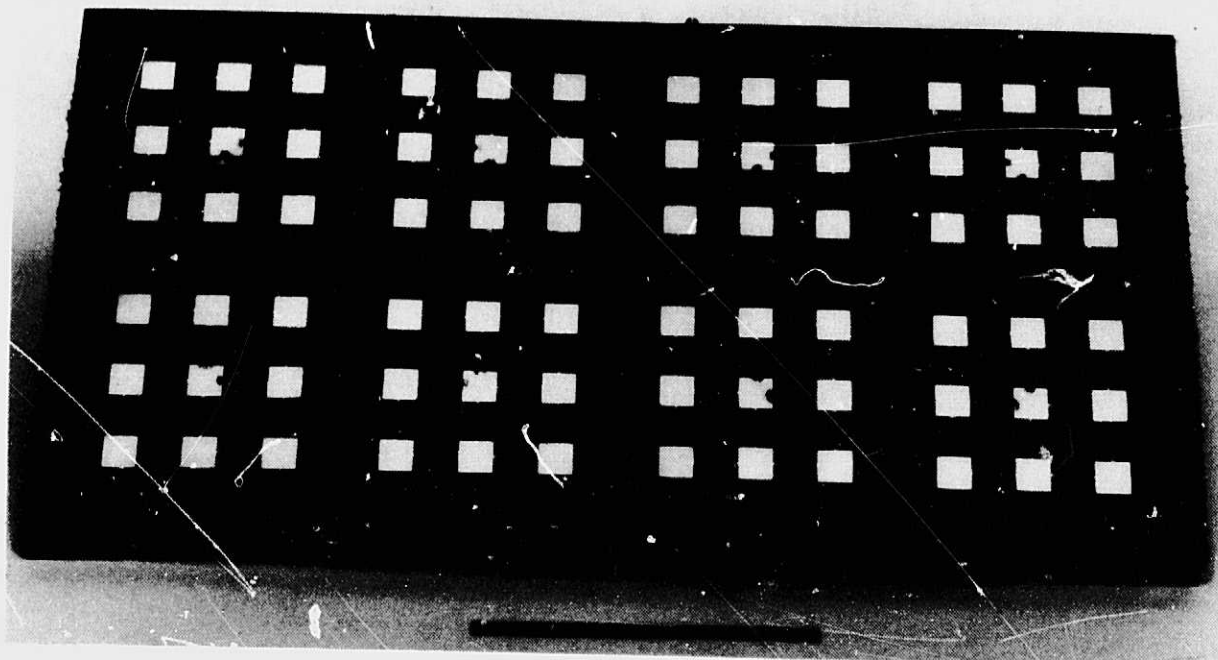
Fig. 2. A model of a stacked microstrip antenna with dual frequency
and dual polarization.

SLOTTED WAVEGUIDE ARRAY ANTENNAS FOR SPACEBORNE SAR APPLICATIONS

D. E. Bostrom, G. A. Carnegis, B. Golvin, and A. C. Knoell
Hughes Aircraft Company
El Segundo, California

I. INTRODUCTION

Starting with mission definitions and constraints for the NASA proposed Shuttle Active Microwave Experiments (SAMEX) and Free-Flying Imaging Radar Experiment (FIREX), Hughes Aircraft Company has compiled and studied the technology available for slotted waveguide planar array antennas suitable for spaceborne SAR application. Antenna performance is derived, and fabrication techniques are discussed. It is implied that mission requirements will always lead to an aperture subdivided into waveguide modules, thereby validating a module definition for other mission building blocks. Finally, a specific design is proposed for a SAMEX mission using the modules as RF aperture building blocks, resulting in a (nominal) 15.1 meter by 5.5 meter extensile dual polarized L-, C-, and X-band planar array with an associated extensile graphite/epoxy support structure. It is further suggested that antenna development begin with a fabrication method development study involving a representative portion of an antenna module.

II. RF DESIGN

Waveguide arrays are an excellent design choice for spaceborne SAR applications. Slotted waveguide array antennas with multifrequency, dual polarization, and wide swath capability have the advantages of high aperture efficiency, precise aperture illumination control, planar packaging for storage, uniform solar illumination, small surface errors, and small feed losses. The antenna apertures are divided into modules or subarrays with a corporate feed; this arrangement provides increased bandwidth, allows for thermal expansion joints, simplifies fabrication, and facilitates folding. Table 1 shows the performance requirements used as a basis for study.

Selection of the antenna is primarily influenced by the fact that a slotted waveguide transmission line incorporates a space-efficient low-loss radiator with a low-loss transmission line. The need for dual polarization and low cross-polarization levels (CPL) leads to use of dual apertures for each frequency band. Standing wave feeding, rather than traveling wave feeding, is advantageous and selected because (1) the beam does not scan with frequency, (2) impedance matching is simple for short arrays, (3) no power is dissipated in a load at the end of an array element, and (4) mutual coupling is well accounted for in the design procedure.

Essential features of an antenna and a typical module are shown in Figs. 1 and 2. Figure 3, the circuit representation of the module, indicates the flexibility possible in module design. Each circuit element can be controlled individually, so that designs with different aperture distributions and internal impedance levels can be easily realized using well-known radiating and coupling slot characteristics.

The aperture size for each frequency band is derived from individual mission constraints upon look angle and swath width for a range of altitudes; consideration of these constraints leads to the selection of the beamwidths and hence to the size of the array. The array is assembled from modules whose number is determined by bandwidth considerations.

The basic module size for each band is determined primarily by the required bandwidth and the longitudinal constraints. The resulting module size for the requirements of Table 1 are shown in Table 2 for each band. Table 3 shows electrical performance for the typical array. Figure 4 shows the dimensions of each panel and the module layout. The height of the integrated (L/C/X-band) antenna, derived from RF considerations, is 5.48 meters. It should be noted that an antenna of this height, when deployed, may obscure portions of the thermal control system of the transport vehicle.

III. MECHANICAL DESIGN DEVELOPMENT

The mechanical design review is a compilation of information obtained from the literature (foreign and domestic) and from vendors. The preferred array design concept, shown in Fig. 5, consists of a lightweight, foam-filled (for L-band cell size only) aluminum waveguide planar array supported on a lightweight, thermally-stable graphite/epoxy truss structure. The array is composed of several 2.5-meter-wide panels that are mechanically decoupled from each other but are otherwise supported on the truss structure. In this way, thermal distortion effects are confined to a maximum panel length of 2.5 meters. The supported structure consists of a collapsible GR/E truss for minimum storage volume in the shuttle bay. Metal Matrix Composite (MMC) designs, cambered aluminum designs, and graphite/epoxy (GR/E) designs were studied and rejected.

The proposed design consists of a (nominal) 15.1-meter by 5.5-meter extensile dual polarized L-, C-, and X-band planar array with an associated extensile GR/E support structure. The array consists of six 2.5-meter by 5.5-meter subarray dual polarized panels joined with discrete hinges. The subarray panel for each polarization consists of L-, C-, and X-band modules in a layout pattern as shown in Fig. 6.

The array consists of thin-walled (nominal 0.010-inch thick) aluminum waveguide cells; the cells of the L-band array are filled with low-density dielectric foam. The foam maintains cell stability during vibration and reduces dynamic wall stresses through increased structural damping. The weight of the entire array, less mechanisms, support structure, and thermal control deployment hardware is approximately 663 pounds.

A packaging design is suggested that consists of an extensile array of six 2.5 x 5.5 meter subarrays with 5 hinge joints. The array is packaged within the pallet and unfolds along the Shuttle axis (Fig. 7). The results of the preliminary mechanical design analysis are shown in Fig. 8 (a, b, c).

A significant highlight of the study is the development of a reliable, low-cost, fabrication approach to manufacturing the L-band portion of the planar array antenna. This approach consists essentially of using sheet metal construction methods for making the waveguide aluminum cells and ultrasonic welding techniques for joining the cells into an array. The manufacturing method is illustrated in Fig. 9.

RFERENCES

1. "Large Space-Qualified X-Band Planar Array Antenna", HAC Report No. 2753/712.

2. Bostrom, D. E., Lewis, D. J., and Rupp, F. C., "Waveguide-Excited Slot Arrays for Synthetic Array Radar Application," Antenna Department, Radar Systems Group, Hughes Aircraft Company, El Segundo, California.

3. "Development of Graphite-Reinforced Metal Matrix Composite Waveguide Elements," Conference with DWA Composite Specialties, Inc., Chatsworth, California, September 1981.

4. Frisch, E., Siegling, H-F., and Fasold, D., "Development, Manufacture and Testing of a Planar-Array L-Band Antenna," Messerschmitt-Boelkow-Blohm Gmb H, Munich, West Germany.

5. Wagner, R., and Braun, H. M., "Slotted Waveguide Array Antenna from Carbon Fibre Reinforced Plastics for the European Space SAR," Federal Republic of Germany, 1AF 1979 Meeting, Munich, September 1979.

TABLE 2. MODULE SIZES

Band	Freq, GHz	Bandwidth MHz	Bandwidth %	EL X AZ, meters	Module Size No. Waveguides	X	No. Slots Per Waveguide	Polari- zation
L	1.275	50	3.9	0.999 X 0.839	6	X	5	VERT
					5	X	6	HOR
C	5.3	150	2.8	0.240 X 0.315	6	X	8	VERT
					8	X	6	HOR
X	9.6	300	3.1	0.133 X 0.155	6	X	7	VERT
					7	X	6	HOR
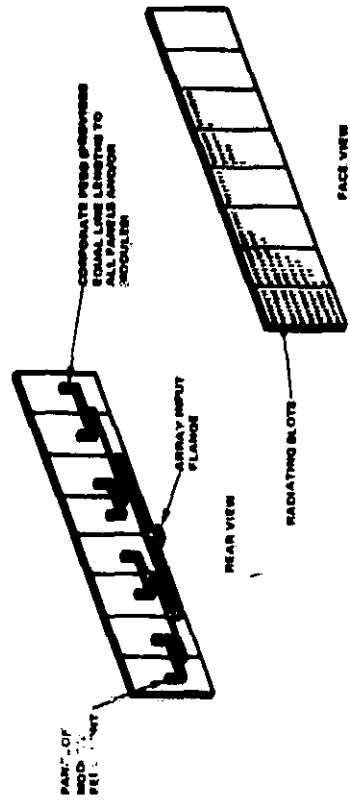
Figure 1. Subdivided Aperture
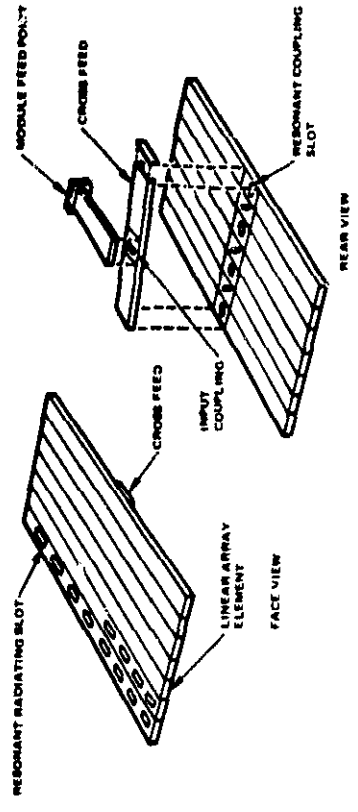
Figure 2. Typical Module Construction

TABLE 1. PERFORMANCE REQUIREMENTS

Altitude, km	250-400
Swath Widths, km	30-120
Look Angles, degrees	15-60
Center Frequency, GHz	
L-Band	1.274 ± 0.025
C-Band	5.3 ± 0.075
X-Band	9.6 ± 0.150
Polarization	HH, VV, HV
Peak Power, kW	
L-Band	1.5
C-Band	10.0
X-Band	16.0
Maximum Sidelobe Level, dB	
Range (Elevation)	-18
Doppler (Azimuth)	-14
Cross-Polarization Level	-27 dB over -6 dB processed level of 2-way pattern
Antenna Height, meters	
L-Band	2.10
C-Band	0.51
X-Band	0.28
Antenna Length, meters	12-18

TABLE 3. ELECTRICAL PERFORMANCE

	L-band	C-band	X-band
Frequency, GHz	1.275	5.3	9.6
Bandwidth, MHz	50	150	300
Net Gain, dB			
Area Gain	37.1	41.4	40.6 (42.6)*
	38.4	44.5	47.1
Aperture Distribution Loss	0.4	0.4	0.4
Other Losses	0.9	2.7	6.1 (4.1)*
Beamwidth -3 dB, Degrees			
EL	6.76	6.76	6.76
AZ	.85	.21	.11
Maximum Sidelobe Level, dB			
EL	-18	-18	-18
AZ	-16	-16	-16
Cross Polarization Level, min. dB	-30	-30	-30

*Over-moded waveguide for panel corporate feed.
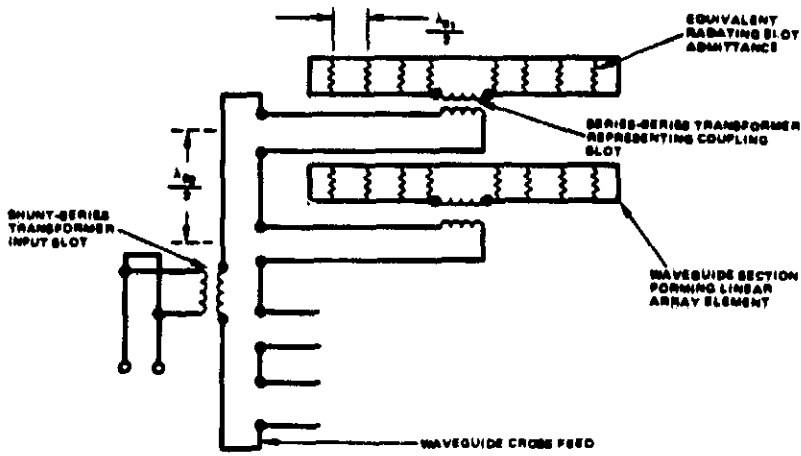
Figure 3. Equivalent Circuit of Module
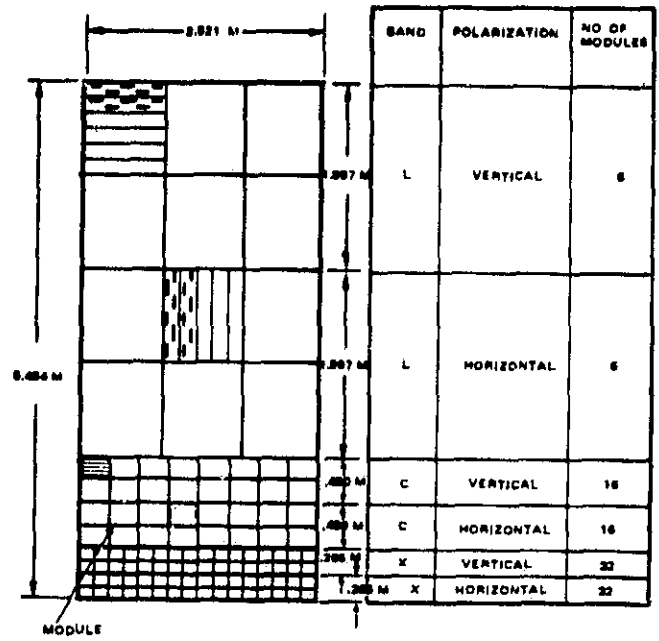
Figure 4. Module Layout of Panel, SAMEX 3,4
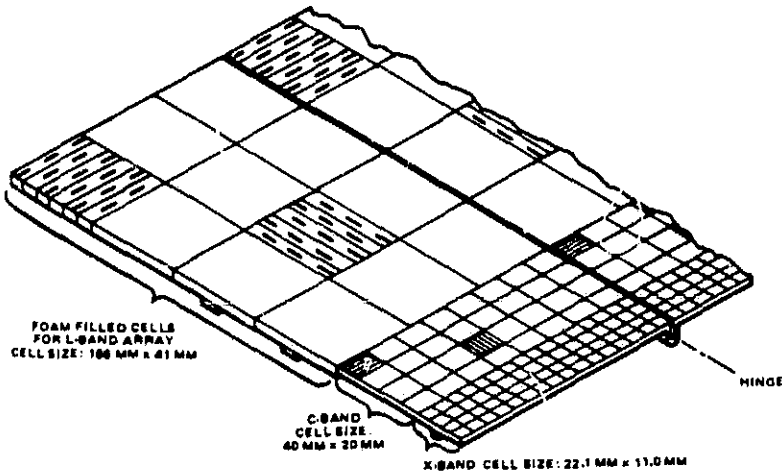
Figure 5. Antenna Planar Array Design Concept for
Aluminum, Foam-Filled Waveguide Array
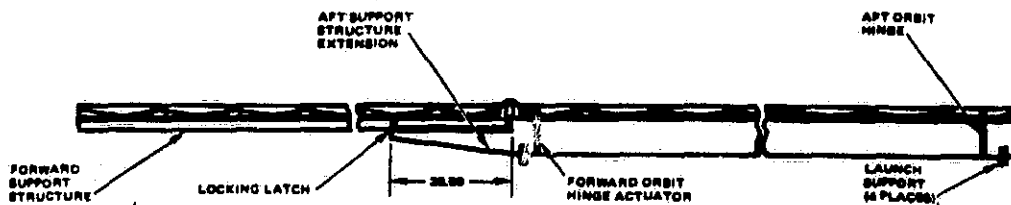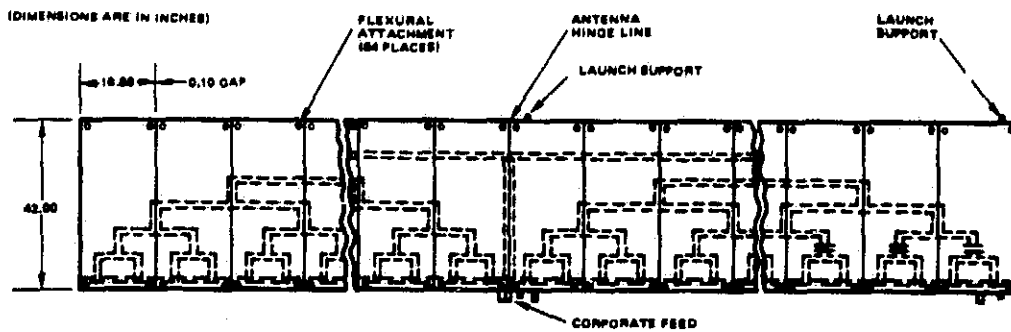
Figure 6. Structural Arrangement of Folded Antenna and Support

39
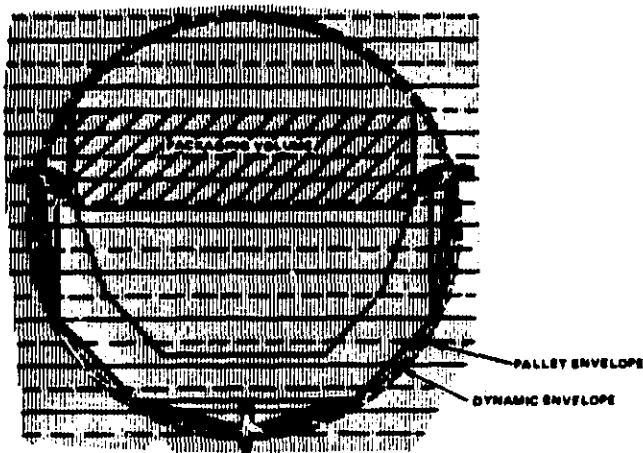
Figure 7. Array Packaging Scheme
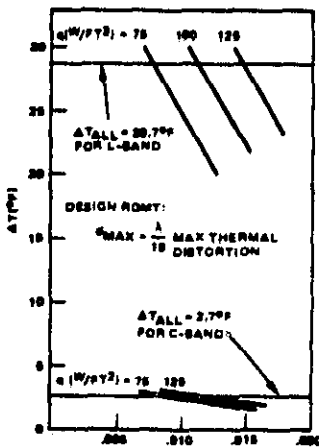
Figure 8a. Stress Analysis
of SAR Antenna
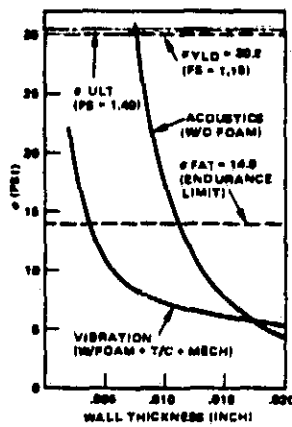
Figure 8b. Thermal Distortion
of SAR Antenna
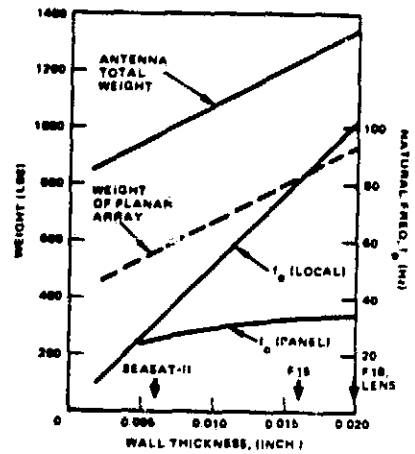
Figure 8c. Weight and Natural
Frequency of SAR Antenna

(4) REPEAT (2) AND (3) AS REQUIRED
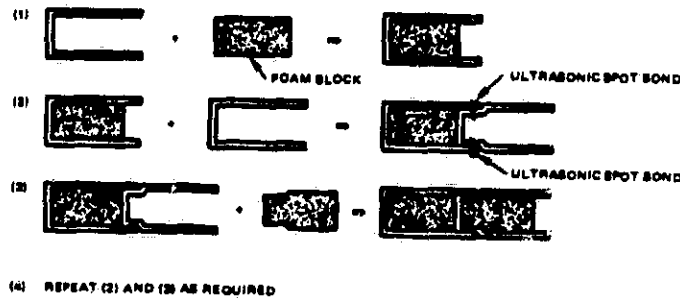
Figure 9. Manufacturing Method for L-band Array

40

SOLID STATE TRANSMITTERS FOR SPACEBORNE RADARS

T. R. Turlington
Westinghouse Electric Corporation
Defense and Electronics Center
Baltimore, Maryland

I.   SEASAT-A

The Seasat-A synthetic aperture radar, the first spaceborne SAR, utilized an all-solid-state RF signal synthesizer and L-band transmitter to drive a corporately fed flat plate array. The RF signal synthesizer generated a linear FM "CHIRP" waveform and provided stable CW reference signals used by JPL to upconvert the received signal to a unified S-band downlink channel, and to synchronize JPL's satellite control logic. Figure 1 shows a simplified block diagram of the Seasat-A transmitter.

The transmitter generated 1200 watts peak RF power (66 watts average) at a center frequency of 1.275 GHz from 354 watts of dc prime power. Linear FM CHIRP swept symmetrically around the center frequency with a bandwidth of 19.05 MHz and a pulse duration of 33.8 µsec. Pulse repetition rate was variable from 1647 to 1944 pps. These transmitter signal parameters combined with the flat plate 34 x 7.5 ft aperture at an orbital altitude of 498 miles and a look angle 20° off nadir gave the SAR an 85-foot resolution over a 15.5-mile-wide swath.

II.   CIRCUIT TECHNIQUES

The exceptionally sharp imagery processed from Seasat-A SAR data is the result of circuit designs that were free of spurious AM and PM sidebands and minimized frequency and phase shifts as a function of temperature and time.

III.   STALO

The stable reference oscillator utilized a 91.059 MHz AT cut 5th overtone quartz resonator. The thermal mass of the STALO design and its thermal time constant, in combination with the AT cut crystal's thermal response, provided oscillator stability measured as fractional frequency deviation $(\Delta f/f_0) < 3 \times 10^{-10}$ for sample times $\tau = 7 \times 10^{-2}$ seconds, under dynamic thermal change at rates of 1.4°C per minute. Frequency stability was better than 1×10^{-10} for stable thermal conditions.

IV.   LINEAR FM GENERATOR

A 91-MHz quartz SAW dispersive delay line capable of generating 0.562 MHz per nsec dispersion was impulsed with a 32.9 nsec sample of the reference oscillator signal. The sin x/x shaped spectrum of the impulse had 60.7 MHz bandwidth between the first nulls and a 3-dB bandwidth of 26.8 MHz.

The central portion of the sin x/x spectrum was dispersed, gated, amplified and limited to produce the 33.8-μsec-long, 19.05-MHz-bandwidth, linear FM pulse at center frequency 91 MHz.

The final transmit frequency at 1.275 GHz ($14\ f_0$) was synthesized by upconverting. The final up conversion $14\ f_0 = 18\ f_0 - (4f_0 \pm \Delta f)$ caused inversion of the linear FM.

V. TRANSMITTER

After up conversion to $14\ f_0$, the signal was applied to a 3-way power split, amplified by three parallel drivers and three parallel power amplifiers, recombined in a stripline combiner, and circulated to the antenna.

Three driver amplifiers each obtained 45 watts peak RF output (2.47 watts average) with 54-dB gain. Driver DC to RF conversion efficiency was 28.7%. Microwave circuit fabrication techniques used in the driver were microstrip on alumina substrates.

Three power amplifier modules, each generating 500 watts peak (27.5 W average), with 10.5-dB gain, developed the 1200 watts that finally reached the antenna input. Power added efficiency for the power modules was 24.3%. Except for the output circuit of each power module, RF circuits were microstrip on alumina (Fig. 2).

The RF power outputs of the three power amplifier modules were combined in a stripline combiner that contained a lowpass filter, circulator and output monitor detector. Insertion loss of the flat plate combiner was 1.0 dB.

The synthesizer-transmitter circuitry was packaged in vented, machined aluminum chassis that were all assembled with their interconnecting cables into a 32 x 16 x 9-inch vented housing which was machined from a solid block of aluminum (Fig. 3). The entire transmitter assembly weighed 65 lbs.

The synthesizer-transmitter was designed and fabricated at the Westinghouse Defense and Electronic Center, Baltimore, Maryland. The flat plate corporately fed array was designed and fabricated by Ball Brothers.

VI. FUTURE SPACE-BASED RADAR

Synthesizer and transmitter designs for future space-based radars will be dictated by radar functions. Synthetic aperture systems like Sesat will most likely continue to use corporately fed flat plate arrays of passive radiating elements, whereas target acquisition and track systems will require electronic scannability. The latter requirement will be satisfied with arrays of active transmit-receive modules having gallium arsenide monolithic microwave circuit chips performing low noise amplifier, T/R switching, phase shifting, and transmitter power generation functions. Gallium arsenide field effect transistors will be used in SAR systems at and above 2 GHz.

Stable reference frequencies will be generated by bulk acoustic resonators which will provide frequency stability and the capability of multichannel operation. Variable time-bandwidth product CHIRP waveforms will be generated by digital techniques to provide resolution control and variable-pulse-width linear FM.

Transmitters will utilize GaAs FETs in Class B circuit configurations providing power added efficiencies up to 60%. More efficient RF power combining techniques will provide greater power levels from solid state circuitry at frequencies up to 18 GHz. Newly developed soft dielectric microwave circuit techniques will undoubtedly be used to fabricate high-power solid-state amplifiers like the 500-watt 18-dB gain L-band module shown in Fig. 4.
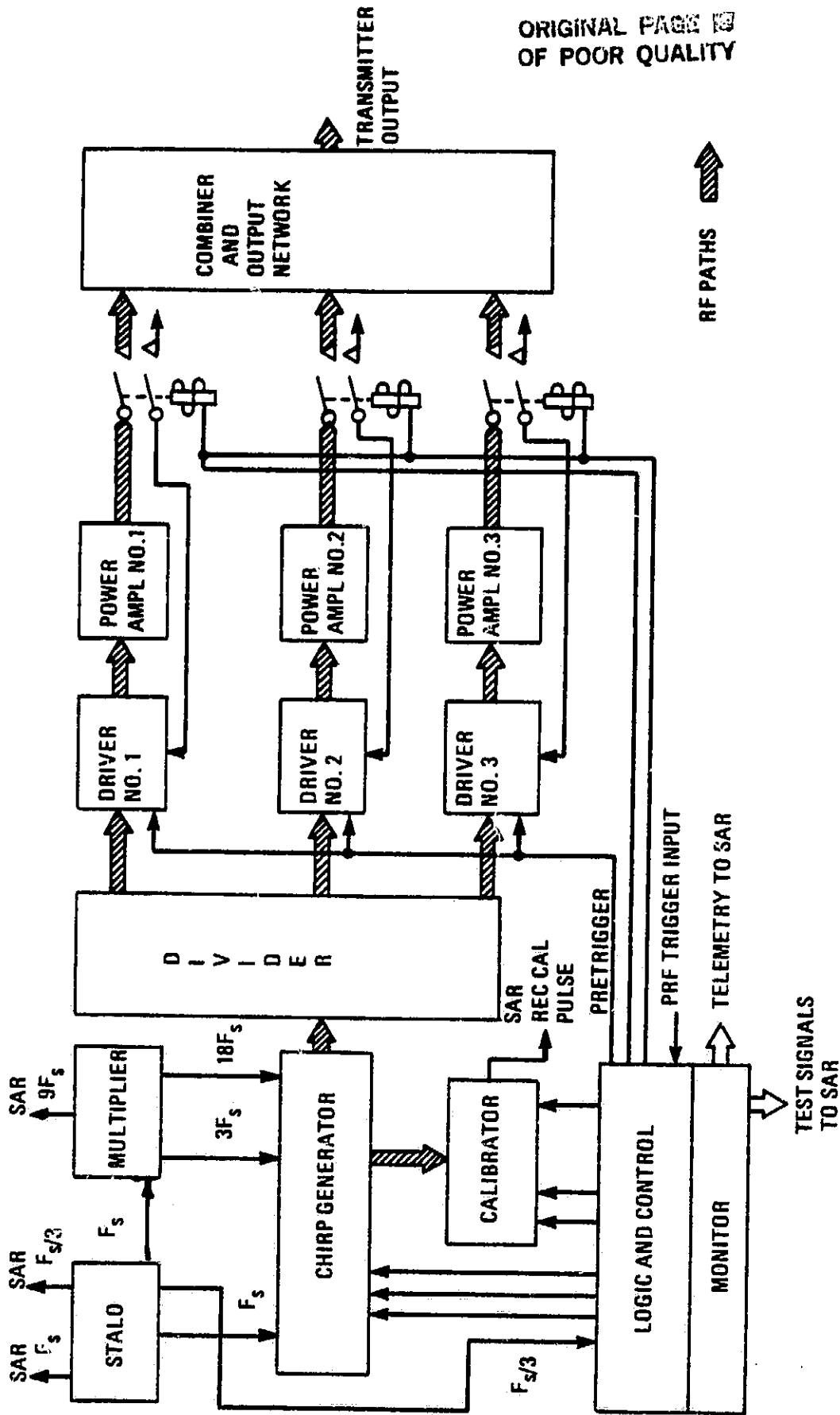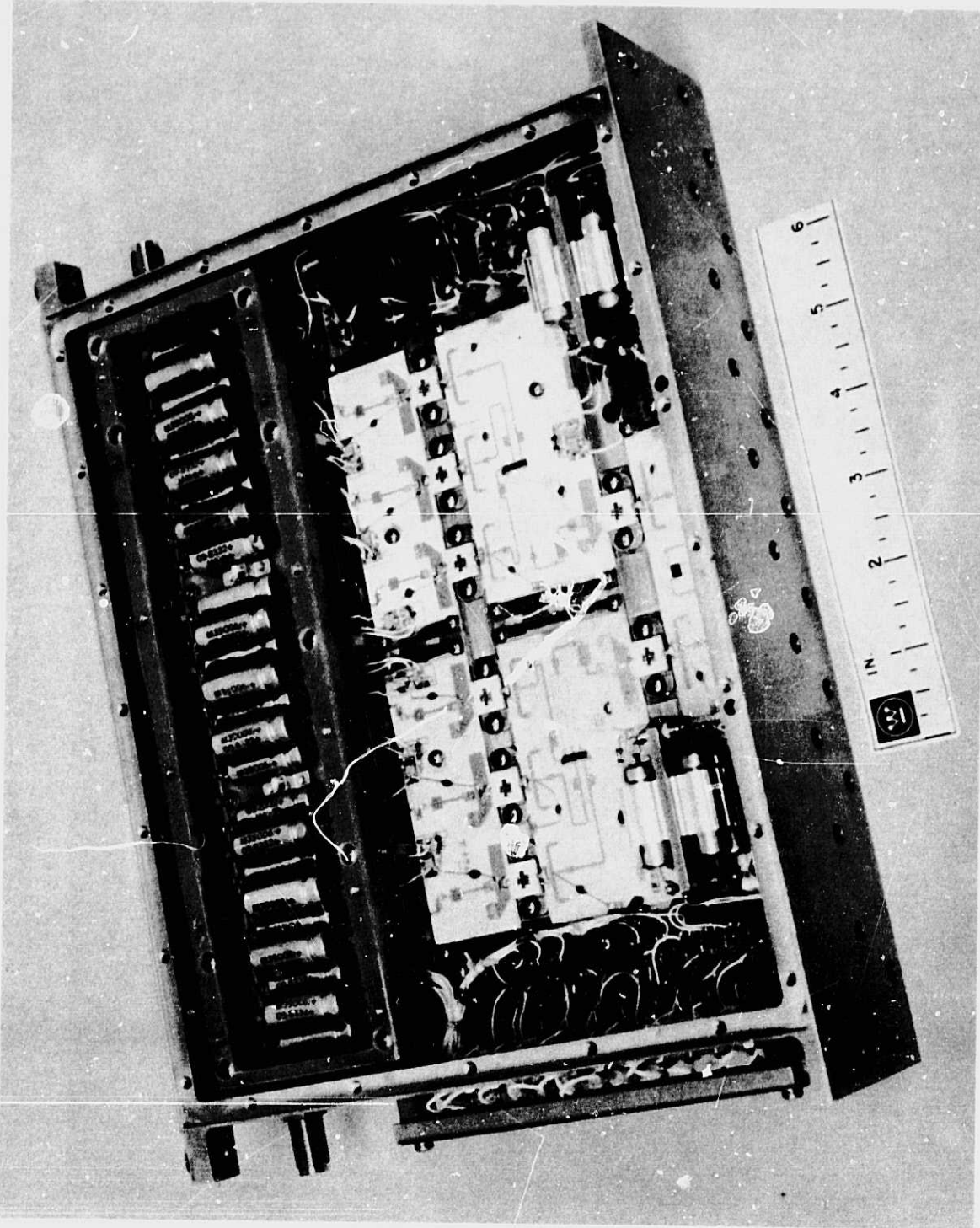
Fig. 1. Transmitter.

Fig. 2. Transmitter power amplifier.
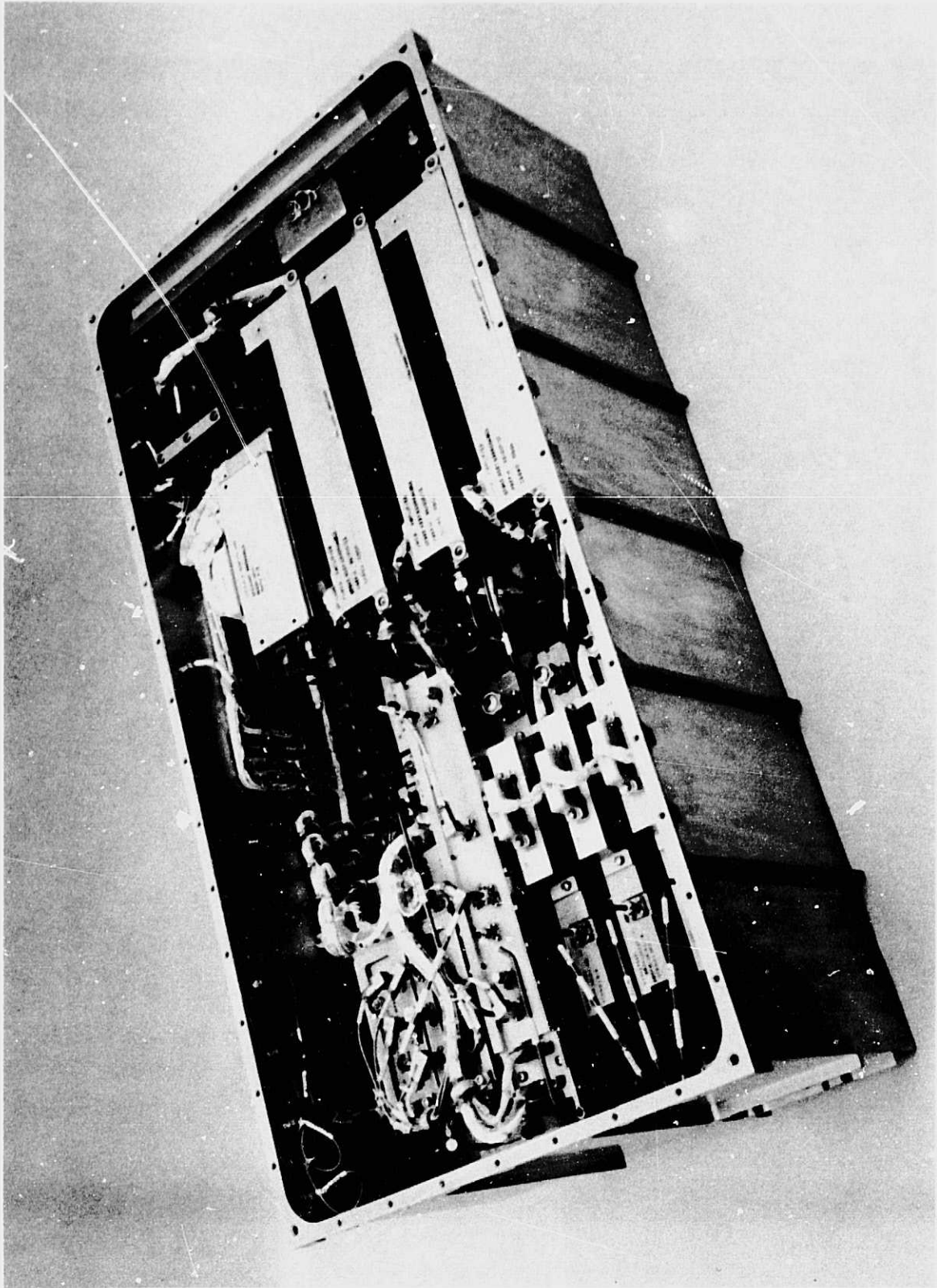
Fig. 3. Seasat-A SAR transmitter.
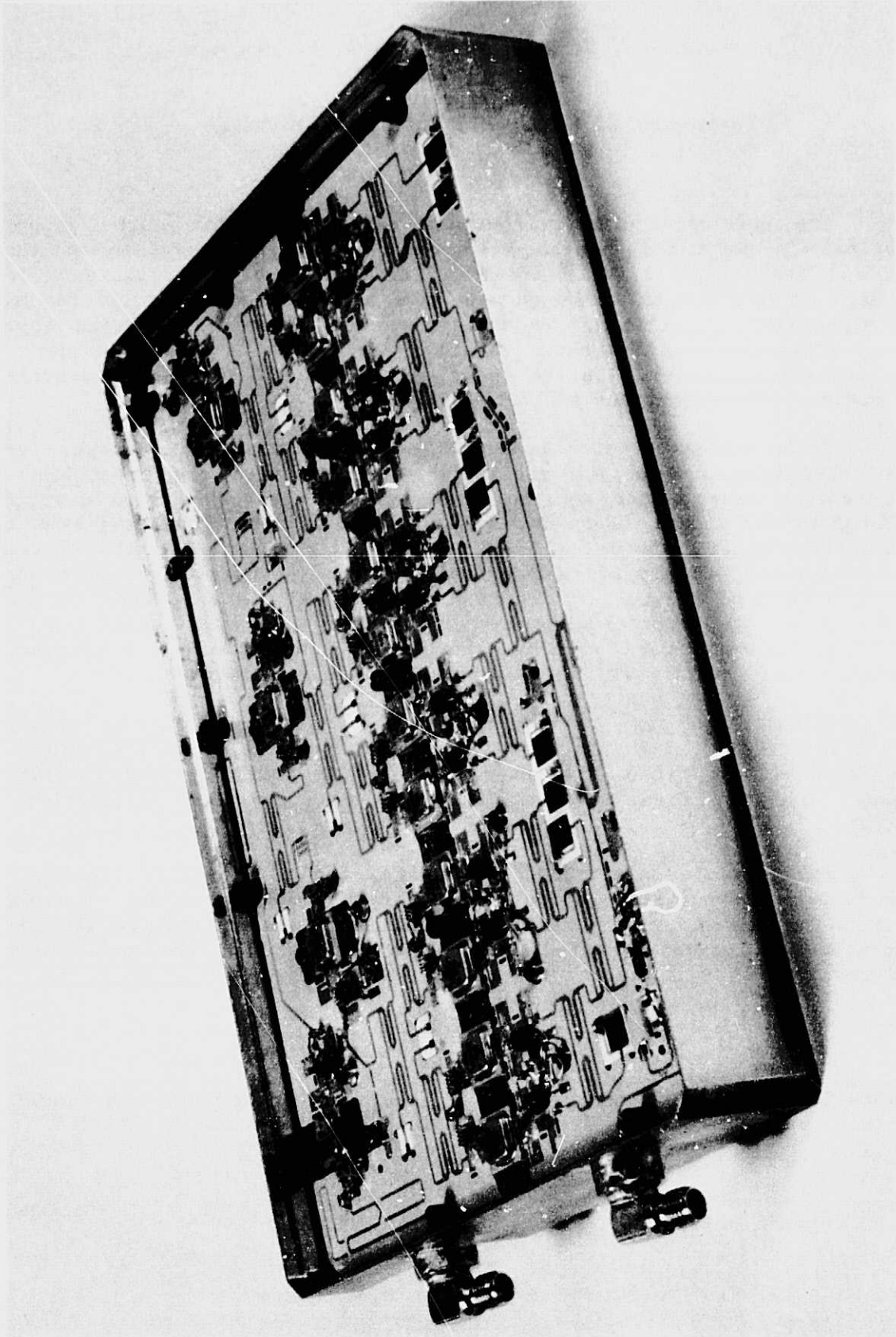
Fig. 4.   500-watt L-band module.

SAR CALIBRATION: A TECHNOLOGY REVIEW[1]

R. W. Larson, D. T. Politis, and R. A. Shuchman

Radar Division
Environmental Research Institute of Michigan
Ann Arbor, Michigan

The use of Synthetic Aperture Radar (SAR) for earth resource applications is motivated by the all-weather day/night operation of these systems and their capability of providing fine resolution microwave reflectivity data at long ranges. SAR systems have been used successfully for many years, especially in military reconnaissance and target acquisition applications. These applications have primarily exploited the SAR image data to provide information related to the position, shape, and the relative reflectivity distribution of various scattering objects.

There are many earth resource SAR applications in geology, agriculture, oceanography, and ice monitoring which require the capability of making absolute radar cross section measurements. Moreover, when designing target acquisition radars, necessary inputs for most detection algorithms are the radar cross section characteristics of tactical targets and ground clutter. The complexity and variety of targets and terrain types as well as the presence of both natural and cultural contaminating objects make it very difficult to derive a useful theoretical model to predict microwave reflectivity in general. It is therefore necessary to depend heavily upon experimental measurements that can be obtained only from a calibrated SAR.

A SAR system may be calibrated either in a relative or absolute sense. A relatively calibrated system allows us to make exact comparison of measured data values. If one is interested only in obtaining high resolution SAR images that are free of system effects, then relative calibration is sufficient.

For absolute calibration capability, the total system function of the SAR must be known exactly to permit data from different passes or different days to be compared. For example, if soil moisture comparisons are to be made between SAR images collected over a one-month period, absolute calibration is required.

Beginning early in 1980, ERIM has been involved in a SAR calibration technology program with NASA, Johnson Space Center (JSC). This program is a part of a cooperative US Air Force and NASA effort. The objectives of this cooperative effort are to: (1) develop and standardize SAR calibration technology and techniques; (2) demonstrate calibration techniques in aircraft flight experiments using the AF-ERIM test bed radar; and (3) provide calibration technology for future NASA application SAR missions. The JSC-SAR calibration program first reviewed various technologies applicable to this problem. This was followed by generation of a test plan that details a calibration procedure for SAR. Present plans call for two calibration flights to be flown, one in 1983 and the other in 1984.

To illustrate the above calibration procedures, a summary of various US Air Force-sponsored calibration programs conducted at ERIM will be discussed.

In this presentation, various potential applications of amplitude-calibrated SAR systems are briefly described, along with an estimate of calibration performance requirements. A review of the basic SAR calibration problem is given with discussion of some of the factors that affect our ability to calibrate a SAR. For background purposes and to establish consistent definition of terms, various conventional SAR performance parameters are reviewed along with three additional parameters which are directly related to calibrated SAR systems. Techniques for calibrating a SAR are described; important aspects that must be considered when designing a calibrated system and various error sources that affect reflectivity measurements will be reviewed.

Included in the results presented are: (1) calibration philosophy and procedures; (2) review of the calibration signal generator technology development with results describing both the development of instrumentation and internal calibration measurements for two SAR systems; (3) summary of analysis and measurements required to determine optimum retroreflector design and configuration for use as a reference for the absolute calibration of a SAR system; and (4) summary of techniques for in-flight measurements of SAR antenna response.

Earth Resources Research

STEREO IMAGING WITH SPACEBORNE RADARS

F. Leberl
Technical University and Graz Research Center
A-8010 Graz, Austria

M. Kobrick
Jet Propulsion Laboratory, California Institute of Technology
Pasadena, California

Stereo viewing is a valuable tool in photointerpretation and can be used for the quantitative reconstruction of the three-dimensional shape of a topographical surface.

Stereo derives from the greek word "stereos" (hard, solid). Stereo viewing refers to a visual perception of space by presenting an overlapping image pair to an observer so that a three-dimensional model is formed in his brain. Some of the observer's function can be performed by machine-correlation of the overlapping images - so called automated stereo corre-lation. The direct perception of space with two eyes is often called natural binocular vision; techniques of generating three-dimensional models of the surface from two sets of monocular image measurements is the topic of stereology.

Stereo viewing of side-looking radar images has been a topic of discussion since 1963, when La Prade (1963) reported on first experiments. The most commonly discussed stereo imaging arrangements with radar have either both flights at the same side or each of the two flights at opposite sides of the object. Other arrangements have been discussed in theory but have not materialized.

Satellite radar images have been produced in the Apollo 17 ALSE project of the Moon, in the Seasat-SAR and Space Shuttle SIR-A missions; all missions resulted in overlapping side-looking radar imagery suitable for stereo viewing. However, from orbits, the standard aircraft radar flight arrangements with parallel "same" or "opposite-side" stereo do not exist at all times: a considerable portion of overlapping images is from non-parallel flight lines.

All three past satellite-radar missions have been investigated for their resulting variation of overlapping radar images for stereo viewing. These were used to obtain indications of the capabilities and limitations of stereo radar. Apart from mere verification of the physiological stereo-viewability there exists a requirement to evaluate its quality by numbers. This can be by defining an exaggeration factor and a reconstruction accuracy of the three coordinates. Both measures of quality were obtained for the satellite radar mission and are shown in Table 1.

The exaggeration factor is sometimes used in photogrammetry to compare the real base-to-height ratio of imaged objects with the visually perceived base-to-height relationship. This factor is thus a measure of flatness of the stereo model: a value of zero is the flat reproduction of the surface; a value of 3-5 corresponds with results known in photography.

The accuracy is obtained by comparing object height differences from radar measurements with those in nature. A wide range of values results; they indicate that the accuracy is so far not well suited for operational topographic height mapping on Earth, with errors amounting to more than ±100 m (Leberl, 1979).

However, stereo radar height measurements can be of value in image analyses that depend on control of topographic effects. A digital height model (DHM) is only rarely available for a study area and is difficult to accurately register to a radar image. A DHM computed from stereo radar is directly registered to the images and should be accurate enough to correct the radar data for radiometric and geometric defects due to surface slopes.

Satellite radar images have been used to develop and demonstrate correction techniques once a DHM is available; and they have addressed the question of obtaining a DHM from radar images themselves. For this purpose the images from SIR-A were of particular interest, since some typical and novel radar stereo configurations were produced: flight lines intersect at angles up to 35° and still permit one to obtain a valid stereo impression. This set of data resulted in an experimental DHM obtained from overlapping SIR-A images alone.

The stereo viewability of radar image pairs cannot be investigated in a convincing manner with the small variation of existing stereo image configurations. The viewability depends on radar look angles, stereo intersection angle, type of terrain and flight line arrangements. Most available imagery is taken at similar, hardly variable look angles. To exploit the full range of possibilities one can take advantage of image simulation. Several initiatives have been developed recently, among them those of Kaupp et al. (1982) and of Leberl et al. (1982). Indications are that intersection angles of 60° or so produce good stereo radar image pairs.

More work is required to expand radar image simulation: squinted mode operation, intersecting flight lines, eccentric satellite orbits, tone and texture variation are needed to cover a wide range of potential satellite radar parameters.

REFERENCES

Kaupp V., L. Bridges, M. Pisaruck, H. MacDonald, and W. Waite, Comparison of Simulated Stereo Radar Imagery. IGARSS '82, 1-4 June 1982, Munich, Paper TAU.

La Prade G. (1963), An Analytical and Experimental Study of Stereo for Radar, Photogrammetric Engineering, Vol. XXIX.

Leberl F. (1979), Accuracy Analysis of Stereo Side-Looking Radar, Photogrammetric Engineering and Remote Sensing, Vol. XLV, pp. 1083-1096.

Leberl F., J. Raggam, and M. Kobrick (1982), Stereo Viewing of SAR Images, Manuscript, 20 pages, Graz Research Center, submitted for publication.

Table 1. Exaggeration factors and height accuracy achieved with
satellite radar (after correction polynomial was applied)

Radar mission	Look angle, deg	Intersection angle, deg	Flying height km	Exaggeration factor	Height accuracy, m	Comment
Seasat	22	4.8	800	3.8	121	Granite mtn.
Apollo ALSE	10	1.9	116	17	150	
SIR-B	47	37	264	3.0	162	Cephalonia flight-lines intersect

SIR-A AIDS REGIONAL GEOLOGY: COMPARISONS
OF SIR-A IMAGERY WITH SLAR AND LANDSAT
OVER GUYANA, VENEZUELA, NICARAGUA AND MALI

P. H. A. Martin-Kaye and G. M. Lawrence
Hunting Geology and Geophysics Limited,
Boreham Wood, Hertfordshire, England

This paper considers SIR-A data from contrasted regions of rain forest and desert and the results of experiments in the combination of SIR-A with SLAR and with Landsat imagery.

I.   SIR-A OVER RAIN FORESTS

A.   The Pakaraima Mountains, Guyana

SIR-A Data Take 34 covers a strip from the Atlantic Coast of Guyana to the sub-Andes in Peru, almost continuously over rain forest throughout this 2000 kilometer distance, much of it logistically very difficult ground. We here deal with the Pakaraima Mountains, which occupy the Venezuela-Guyana borderlands. SIR-A may have provided the first images of these from space that are completely unobstructed by cloud (Fig. 1).

The geology of Northern Guyana, apart from young cover rocks of the coastal belt and superficial deposits, is of partly remobilized Lower Protero-zoic geosynclinal metavolcanics and sediments cut by granites and overlain by the more or less horizontal formations of the Roraima Group (Reid 1973), also Proterozoic. The Roraima Group, which forms the tabular Pakaraima Mountains, is mainly of quartzites, arkoses, and conglomerates but also contains some shales and jaspers, and includes thick interleaved basic sills age dated about 1,800 m.y. The entire sequence from folded basement to the tabular intrusions in the Roraima thus ranges in time around the Trans-Amazonian orogenesis (2,000 - 1,800 m.y.).

Despite the limitations of scale, which varies across the track, and resolution in SIR-A, comparison of the imagery with maps of the Geological Survey of Guyana quickly shows that a number of substantial positioning errors occur in the map work. This is not surprising; the problems of survey in these remote forests are severe.

The Roraima Group, long known as the Roraima Formation, was pro-posed for elevation to Group status by Reid (1973). It produces a highly distinctive scenery of elevated tablelands, mesas and escarpments. Spectac-ular waterfalls (Kaiteur, Utschi, Angel, etc.) drop from the plateaus. The morphology is excellently expressed in the SIR imagery (Fig. 1). The quart-zites give rise to smooth-surfaced, more or less horizontal, tabular blocks, many square kilometers in extent. Rectilinear major joints or fractures, rather sparsely distributed in these Eastern Pakaraima Mountains, are in various stages of opening-up by the river system.

In profile the formation rather consistently gives rise to three or four steps (Martin-Kaye 1952). Figure 2 is a geological map of the SIR-A swath across this part of the Pakaraima Mountains which shows the interpreted distributions of these surfaces. The uppermost (Level 4) is represented by the top of the high mesas of Roraima itself (over 8,000 feet), Kukenaam, etc., and, in the part covered by SIR-A, by the Illutipu group of mesas (probably over 6,000 feet). Level 3 caps the large mesas of the divide between the Kako and Kamarang Rivers; Level 2 forms the widespread upper plateau; Level 1 forms the outer eastern scarps of the Pakaraima Mountains and the floors of some of the valleys in the upper plateau.

Reid (1973) recognized from the St. Elena area of Venezuela three formations, the Uairen, Cuquenan and Uaimapue Formations, within the Group. The arenaceous-conglomeratic Uairen Formation, deposited by a meandering river system, is overlain by fissile silty shales of the Cuquenan Formation which reaches 50 - 100 m in thickness in the type area. Shales which may correlate with the Cuquenan occur in the Kako and Kamarang valleys and outcrop in the escarpments of Level 2. This suggests that the lower step of the Pakaraimas (Level 1) in the region of the Upper Mazaruni River crossed by SIR is equivalent to Reid's Uairen Formation, and that the Upper Plateaus between the Kako, Kamarang, and Ekereku, are, at least in part, of the Cuquenan Formation.

The upper plateaus (Level 2) are capped by arkoses, conglomerates, and sandstones which, in these respects, fit Reid's description of his Uaimapue Formation. The latter also contains cherts and jaspery horizons. Kako is the Indian name for jasper, which presumably occurs in the Kako River basin. Reid's uppermost unit in the Roraima Group, the Mataui Formation, was defined for mapping purposes as comprising the prominent mesas that cover the border between Venezuela, Guyana and Brazil. Illutipu and similarly very high mesas nearby which fall within the SIR-A swath belong to this group.

Level 3 falls between the high mesas and the main upper plateau of the Kamarang/Kako divide and may represent the Uaimape Formation. It is probably the equivalent of the intermediate surface of the Roraima vicinity depicted in Barrington Brown's sketch (Chas. B. Brown, 1875, p. 264). It may be part of Reid's Uaimapue Formation but otherwise could be of gabbro sill.

The same level forms the top of the large isolated mesa, Eboropu, overlooking the mouths of the Kamarang and Kako.

It can be concluded that a morphologic subdivision of the Roraima sequence established from SIR-A imagery probably translates fairly closely to the lithological subdivisions determined in the field by Reid. However, there is a problem in deciding whether Reid's Uaimapue Formation correlates with Level 2 or 3 or both.

Diamonds occur in the alluvials of many of the rivers draining the Pakaraimas. Some of the rivers on the plateaus carry diamonds, e.g., the Ekereku which has its headwaters immediately to the north of the SIR-A swath. Reid notes that diamonds occur in the Uairen Formation. If they are restricted to this formation, they would be expected only in gravels on Level 1.

In the Gran Sabana area of Venezuela there are two or three centers recognizable on SIR-A upon which major linears converge. The primary source of the diamonds of Pakaraimas is not yet known; these centers may possibly mark kimberlitic pipes.

Within the Pakaraima highlands gabbro sills commonly form the floors of principal valleys (i.e., parts of the Kamarang and Mazaruni) but also occur in valley sides and in the mesas. They produce undulant surfaces by comparison with the smooth surfaces of the Roraima deposits themselves and much of their general distribution within the mountains can be delineated within the imagery on this basis. Substantial areas of the diagnostic style of terrain can be seen to occupy reaches of the Mazaruni valley where it doubles back across the SIR-A swath above the Roraima escarpment. This sill also extends up the Kamarang River. However, not all the outcrop produces this distinctive terrain. Some areas in the Kako and Kamarang of smooth textures and even tones are known to be of gabbro. The forest clearing and airstrip at the mouth of the Kamarang, visible on the imagery, are upon gabbro.

B.   Nicaragua

In 1971 Westinghouse's real aperture K_a band radar in a DC6B aircraft was used to image the whole of Nicaragua. Also in November but ten years later SIR-A traversed the country enabling comparison of the two types of imagery to be made. Despite the lapse of time few if any cultural changes likely to be of consequence to the study are believed to have occurred in the selected test areas.

SIR-A Data Take 24C crossed Nicaragua in a southeasterly direction from Honduras, passing over the Rio Coco at the border, and the Rio Bocay, the Sierra Isabella, the mining district of La Luz-Rosita-Concepcion, and the coastal plain, crossing the shore of the Caribbean between the mouths of the Rio Prinzapolka and the Rio Grande de Matagalpa. The changing textures of the terrain shown in the imagery differentiate major rock assemblages. Intricate patterning on the Honduran side of the border marks Palaeozoic metamorphics. These are replaced in the Rio Coco Valley by Mesozoic rocks, signatured by conspicuous ridges rising from the valley floor; the Tertiary volcanics of the Sierra Isabella southwestwards are coarsely textured and strongly fractured. In the east the volcanics are cut near Rosita by a granodiorite intrusive which is readily distinguishable. They give way to volcanogenic, then to lagoonal and littoral deposits of the plain.

The major features can equally well be differentiated on imagery of the SLAR and of the spaceborne SAR, although these are very different radar systems. The airborne radar (AN/APQ97) had higher resolution (nominally 10 m) and dynamic range. These characteristics and the acquisition scale of 1:220,000 enabled enlargement satisfactorily to about 1:50,000 scale. The speckle in SIR-A imagery becomes obtrusive at about 1:100,000 scale, and fine detail observable on the SLAR products is filtered out by the lower resolution (nominally 40 m).

The advantages are, however, by no means one-sided. The relatively uniform moderate incidence angle across much the wider (55 x 20 km) swath

brings a consistency to the synoptic view by SIR-A not obtained by the air-
borne system. Synoptic views are replicated effectively by SLAR mosaics, but
the imaging is by a wider range of inspection angles. In the AN/APQ97 imagery
over mountainous areas, terrain textures tended to be expressed largely in
highlight and shadow. The consistently moderate look angle of SIR-A produces
more evenly illuminated surface data.

Figures 3 and 4 are of an area of about 144 sq km in the lower
reaches of Rio Lawira and Rio Basilikira, both tributaries of the River
Prinzapolka which they join about 15 km inland from the coast. This is an
area of pine and swamp savanna upon alluvial flats of the rivers and the
gravelly/clayey Plio-Pleistocene Bragman's Bluff Formation. Several such
scenes of both SLAR and SIR-A were digitized and warped for mutual fits. They
were then composited interactively with a digital image processor. The
resultant color images are thus simulations of imagery from a dual-frequency
(K_a and L-band) radar (Fig. 5).

Figure 6 shows the categorization of a color composite of the Rio
Lawira – Rio Basilikira area, the hues and intensities in the composite
depending upon the relative and absolute strengths of the returns registered
by the systems. These are indicated by the symbols annotated to the diagram.
An interpretive note (courtesy J. W. Trevett) is appended to the legend.

The composites are an effective way of representing dual-channel
data, significantly expanding interpretive potential, as is the case of a
color composite Landsat image over separate considerations of the individual
MSS bands.

II. SIR-A OVER ARID TERRAIN: ADRAR DES IFORAS, NORTHEAST MALI

The Adrar des Iforas, a desert area in northeast Mali forms a
southwest extension of the central Sahara Hoggar or Tuareg Shield, and com-
prises Upper Proterozoic and reworked older Precambrian basement sliced by
major north-trending shears and comprehensively intruded by granitoid intru-
sives and volcanics. These are part associated with a Pan-African (Upper
Proterozoic) collision zone between the Hoggar Shield and West African
craton. The central shear-bounded rocky outcrop of the Iforas granulite unit
(Archaean and/or Eburnean age) is well shown on both Landsat and SIR-A (Figs.
8 and 9). The landscape is of sand and gravel plains surrounding rocky hills.

The area has been mapped in detail by geologists at the University
of Montpellier (Black, et al., 1979, Caby, et al., 1981, Bertrand and Davison,
1981, and others) (Fig. 7). The prominent Younger Granite ring-intrusions of
alkali granite are conspicuous on the SIR-A (Fig. 8) and Landsat images (Fig.
9). The associated rhyolite and other dyke swarms, however, are far more
distinct on the SIR-A image. They cut the low relief ground of late
Proterozoic granite batholiths, which appears dark on the radar images. The
dykes, which produce trains of blocky debris (under a meter across usually)
are not well resolved by the Landsat. The combination of better resolution
and response to the "roughness" of these blocks results in their excellent
depiction on SIR-A.

Comparison of enhanced Landsat and SIR-A over the Iforas area discloses a considerable number of features observable on SIR-A that are not seen on Landsat. A Landsat sub-scene (Fig. 9) shows distribution of low relief fine gravel plain (light), and rocky areas (dark). Minor scrub vegetation is seen along some wadis (dark). A pronounced rectangular edge to the main gravel plain suggests fault control, and a circular gravel-plain is probably a granite intrusion. The SIR-A over the same area displays a remarkably more complete image. Over the rectangular gravel plain a network of small drainage channels is now introduced. Over the circular area, and elsewhere, the dyke swarms only hinted at on the Landsat are clearly delineated, in spite of the fact that the width of the trains of debris from dykes is mostly much less than the SIR-A spatial resolution. A completely unsuspected circular feature, contained within the larger circle is revealed by the SIR-A.

The minor drainage of the 'rectangular' area is well defined on the radar. The channels have a filling of dry blown sand that absorbs the incident pulses and hence appear black on the positive image. Enhanced Landsat shows a very small proportion of these drainage courses; in fact, the surface in this area appears rather uniform. As reports of the region state that the surface largely is of gravel and cobbles set in a sandy, part saline matrix, we must assume that the SIR-A signal is being returned from shallow sub-surface over a fairly wide area. This phenomenon has been reported for a locality in Sudan and Egypt by McCauley et al. (1982).

III. CONCLUSIONS

SIR-A's geological orientation was fully justified by the results. Large contributions to geological mapwork, hydrology and desertification studies may now be predicted for spaceborne radar, most suitably in Shuttle missions.

SIR-A geological results over tropical forest lands, as elsewhere, benefitted from the consistency of expression across the swath, and the synoptic view obtained from the wide swath.

Over arid lands, results exceeded expectation in the clarity of depiction of structures and certain lithologies.

Prior to SIR-A few people argued for radar imaging over dry arid areas. The useful application appeared small by comparison with the wet tropics. The clear atmosphere and often extensive outcrops enable good airphoto and Landsat cover and good geological data content. The point of adding radar was uncertain. Although Seasat and some earlier work had given indications of the effectiveness of mapping radars over such regions (e.g., Sabins et al. and Schaber et al., 1976), incontrovertible demonstration awaited SIR-A.

SIR-A made traverses across the Saharan and Arabian Deserts, deserts in Australia and Asia, and several other desiccated areas. The clear message that has come from examination of the imagery is that spaceborne radar

over deserts has important statements to make in geological mapping, desertification and hydrogeological studies, and in oil and mineral exploration. Not the least of the discoveries is that the L-band SIR-A radar, at least at the 43° incidence angle, can penetrate flat-lying dry surface sand and fine gravel and return backscatter from a shallow buried rough surface (McCauley et al., 1982).

The moderate depression angle of SIR-A led to improved expression of hill and mountain lands as compared to Seasat imagery, in which some high relief areas are not effectively interpretable. However, more subtle terrain textures, useful for categorization of units, are often below resolution level. This is most noticeable in forested areas.

The results of compositing K_a band imagery with SIR-A clearly indicate a large increase in interpretive potential will be available in dual or multispectral radars.

REFERENCES

Bertrand, J. M. L., and Davison, I., 1981, Pan-African granitoid emplacement in the Adrar des Iforas mobile belt (Mali): a Rb/Sr isotope study, Precambrian Research, 14, 333-61.

Black, R., et al., 1979, Outline of the Pan-African geology of Adrar des Iforas (Republic of Mali), Geol. Rundschau, 68/2, 543-564.

Brown, C. Barrington, 1875, Reports on the Geology of British Guiana.

Caby, R., Bertrand, J. M. L., and Black, 1981, Pan African ocean closure and continental collision in the Hoggar-Iforas segment, central Sahara, Precambrian Plate Tectonics, Kroner, A. (ed.), Chapter 16, 407-451, Elsevier, Amsterdam.

Elachi, C., 1982, Radar images of the earth from space, Scientific American, Dec., 46-53.

Elachi, C., et al., 1982, Shuttle imaging radar experiment, Science, 3 Dec., 218, 4576, 996-1003.

Martin-Kaye, P. H. A., 1952, (a) The Roraima Formation in British Guyana, and (b) The Roraima Formation in the neighbourhood of the Kamarang and Upper Ekereku Rivers, Bull. 22, Geol. Surv. Brit. Guiana.

McCauley, J. F., et al., 1982, Subsurface valleys and geoarcheology of the eastern Sahara revealed by Shuttle radar, Science, 3 Dec., 218, 4576, 1004-1020.

Reid, A. R., 1972, Stratigraphy of the Type Area of the Roraima Group, Venezuela. Memoria de la Nov. Conf. Geol. Inter Guayanas. Publ. Espec. No. 6 Bo.. de Geologia, Minest. de Minas e Hidrocarburos. Venezuela, p. 343.

Sabins, F. F., Jr., et al., 1982, SEASAT radar image of San Andreas Fault, California. Amer. Assoc. Petrol. Geol., Bull. 64/5, 619-628.

Schaber, G. G., et al., 1976, Variations in surface roughness within Death Valley, California; geologic evaluation of 25 cm wavelength radar images. Geol. Soc. Amer., Bull. 87, 29-41.

Settle, M., Taranik, J. V., 1982, Use of the Space Shuttle for remote sensing research: recent results and future prospects, Science, 3 Dec., 218, 4576, 993-995.

Fig. 1.   SIR-A image part Data Take 34 of Pakaraima Mountains, west Guyana, showing massive slabs of Roraima Formation and prominent faults. Nominal scale 1/500,000.
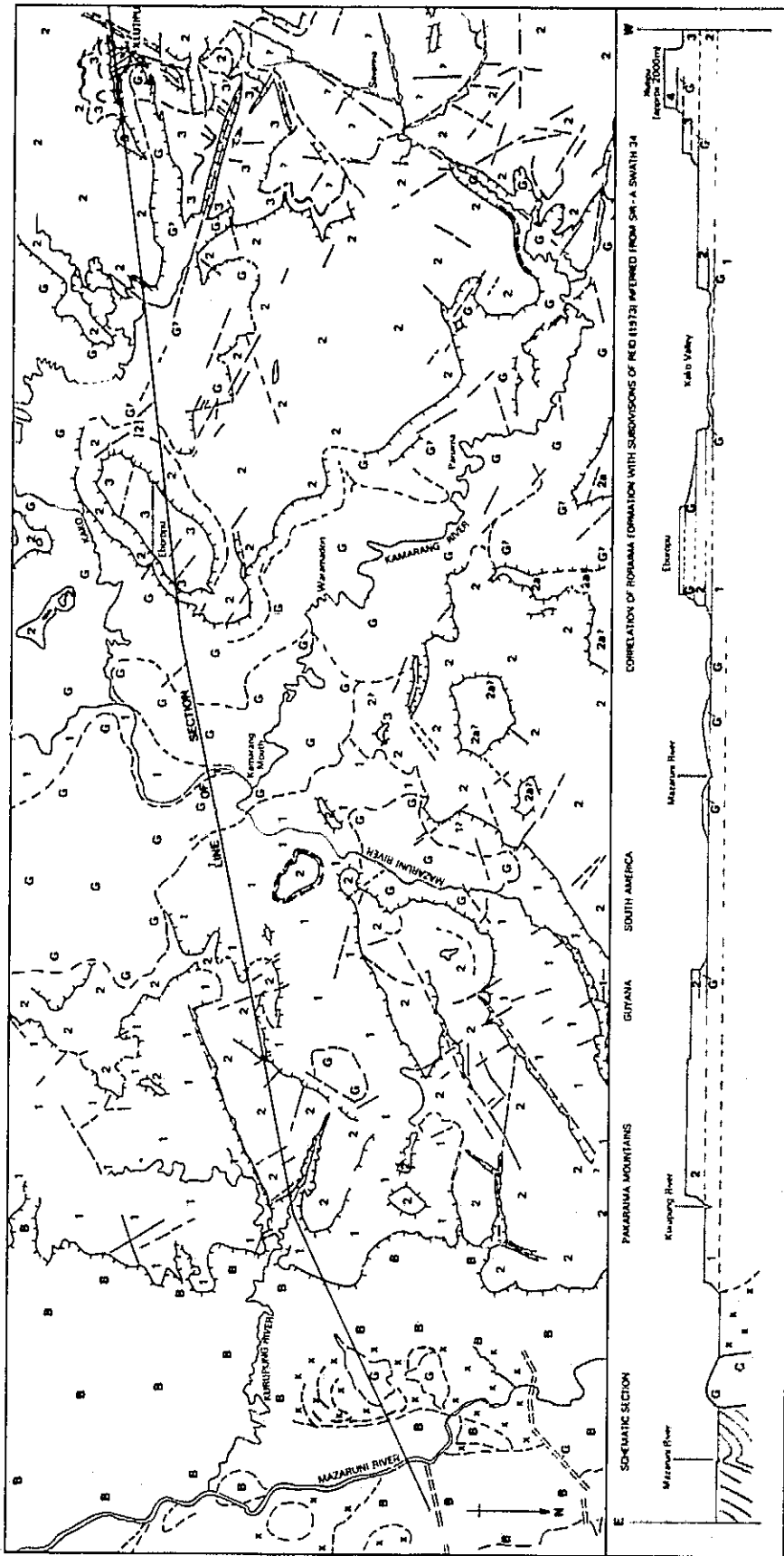
Figure 2. Traverse of the northern Pakaraima Mountains, Guyana, by SIR-A: Sub-division of the Roraima Formation.

Tentative correlations with Reid (1973)

G   Younger Basic Intrusives

(4) = Mataui Fm (Reid 1973)

(3), (2a), (2) = Uaimapué Fm (Reid 1973)

(2) overlies Cuquenan Fm (Reid 1973)

(1) = Uairen Fm (Reid 1973)

x x = Granite

B = Undifferentiated Basement

        Dike

        Escarpment

        Formation boundary

        Bedding trace

        Fracture, Linear

NOTE:

The unconventional orientation of N. to the bottom of the page is necessitated by the direction of radar illumination, (from the south).

Legend for Figure 2
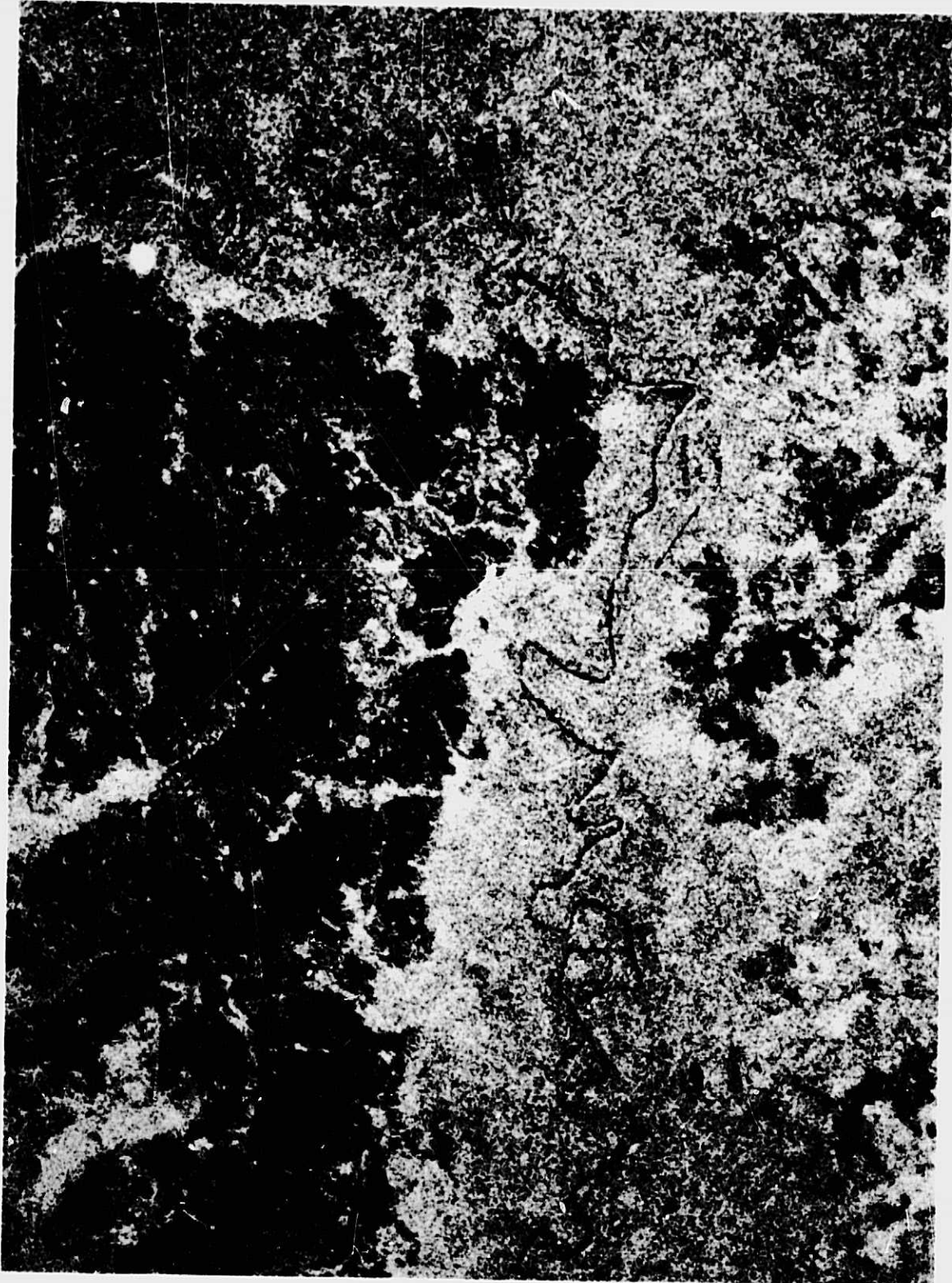
Fig. 3.   SIR-A and SLAR image of area of Alimikamba/Rio Prinzapolka area,
          northeast Nicaragua at 1/100,000 scale: L-band, SAR, SIR-A image
          (Part DT 24C; Nov. 1981).

Fig. 4. As Fig. 3: Westinghouse K_a real aperture SLAR (Nov. 1971).
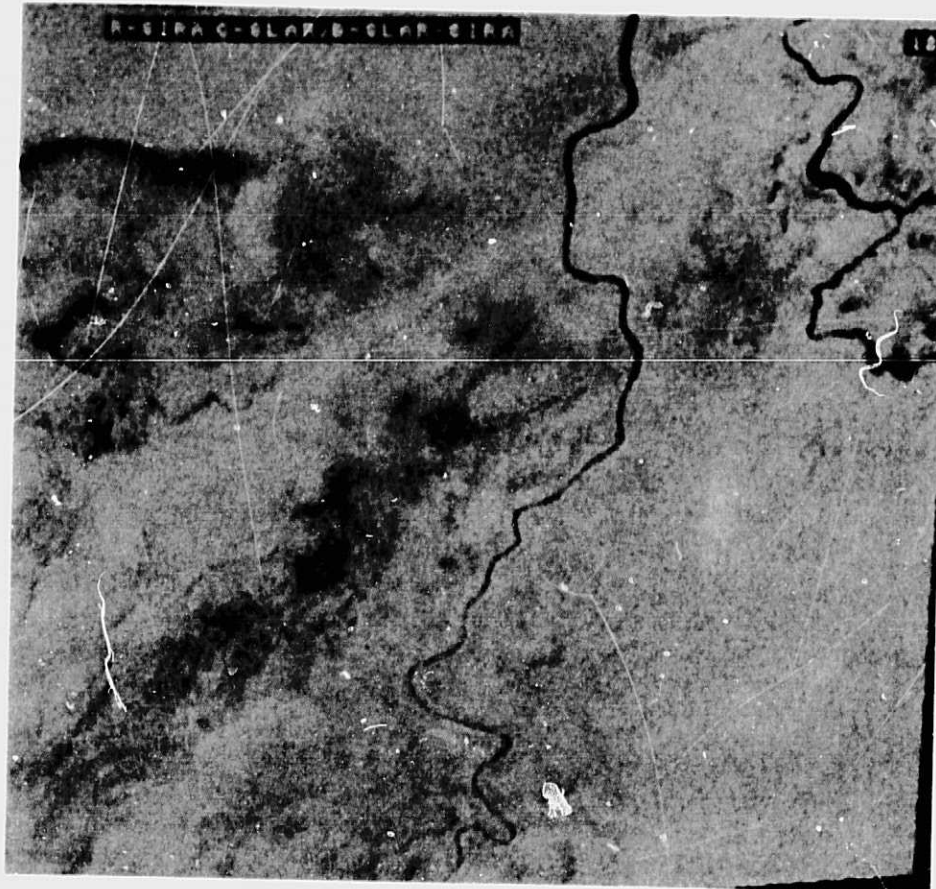
Fig. 5. Composite of SIR-A and SLAR; northeast Nicaragua.

Parts of Rio Lawira and Rio Basilikira,
tributaries of the Lower Rio Prinzapolka, E. Nicaragua.
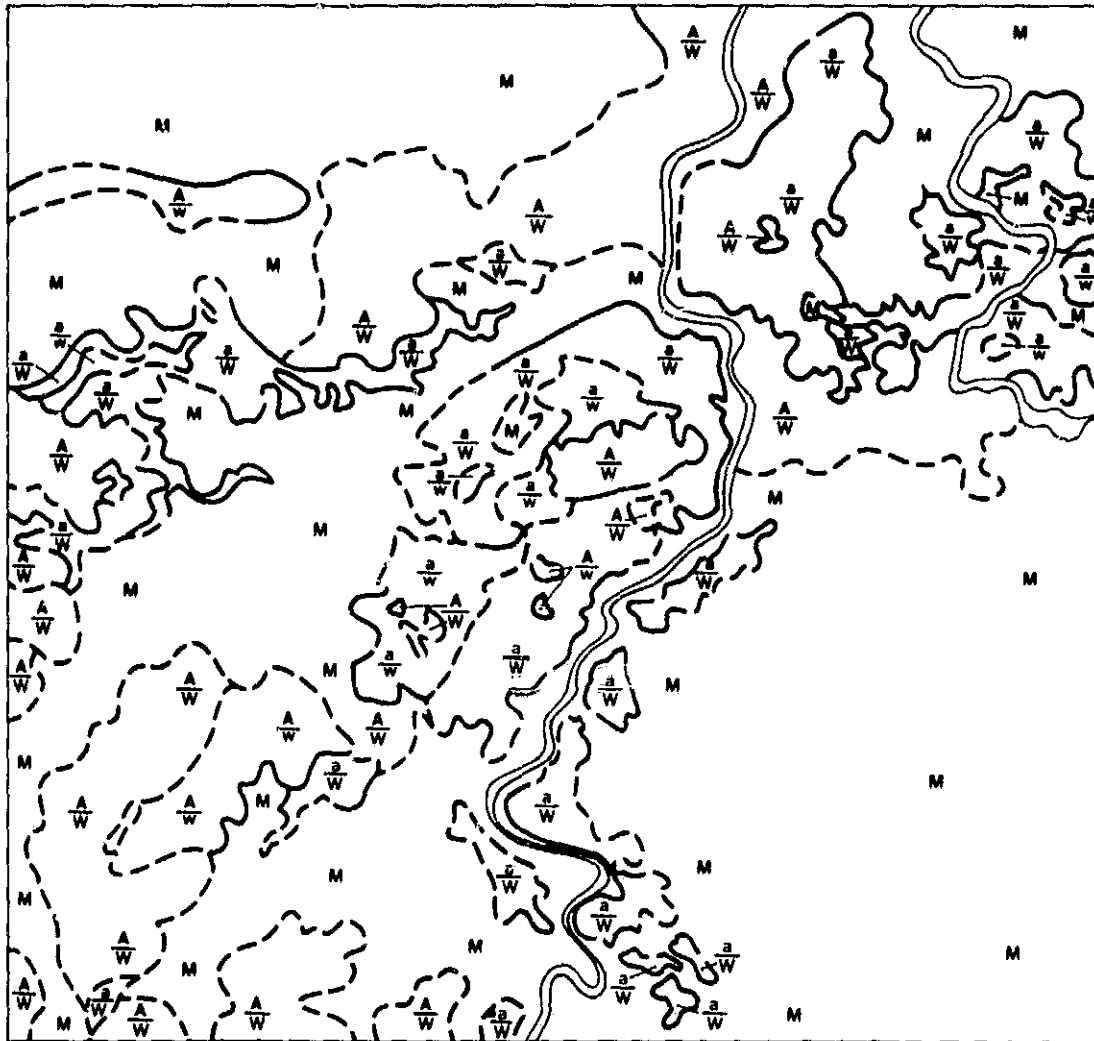
0   2   4   6 Km (approx)

Legend.

Strength of radar responses.
SIR–A

     A = Strong or Moderate.

     a = Weak.

Westinghouse SLAR

     W = Strong or Moderate.

     w = Weak.

     M = Moderate returns, both systems.

Explanation

$\frac{A}{w}$, M and $\frac{A}{W}$ are believed to be varying

hardwood forests with $\frac{A}{W}$ the most dense.

$\frac{a}{W}$ is swamp forest, $\frac{a}{w}$ is mangrove swamp.

Fig. 6. Categorization of composite of SIR-A and SLAR (of Fig. 5).

69
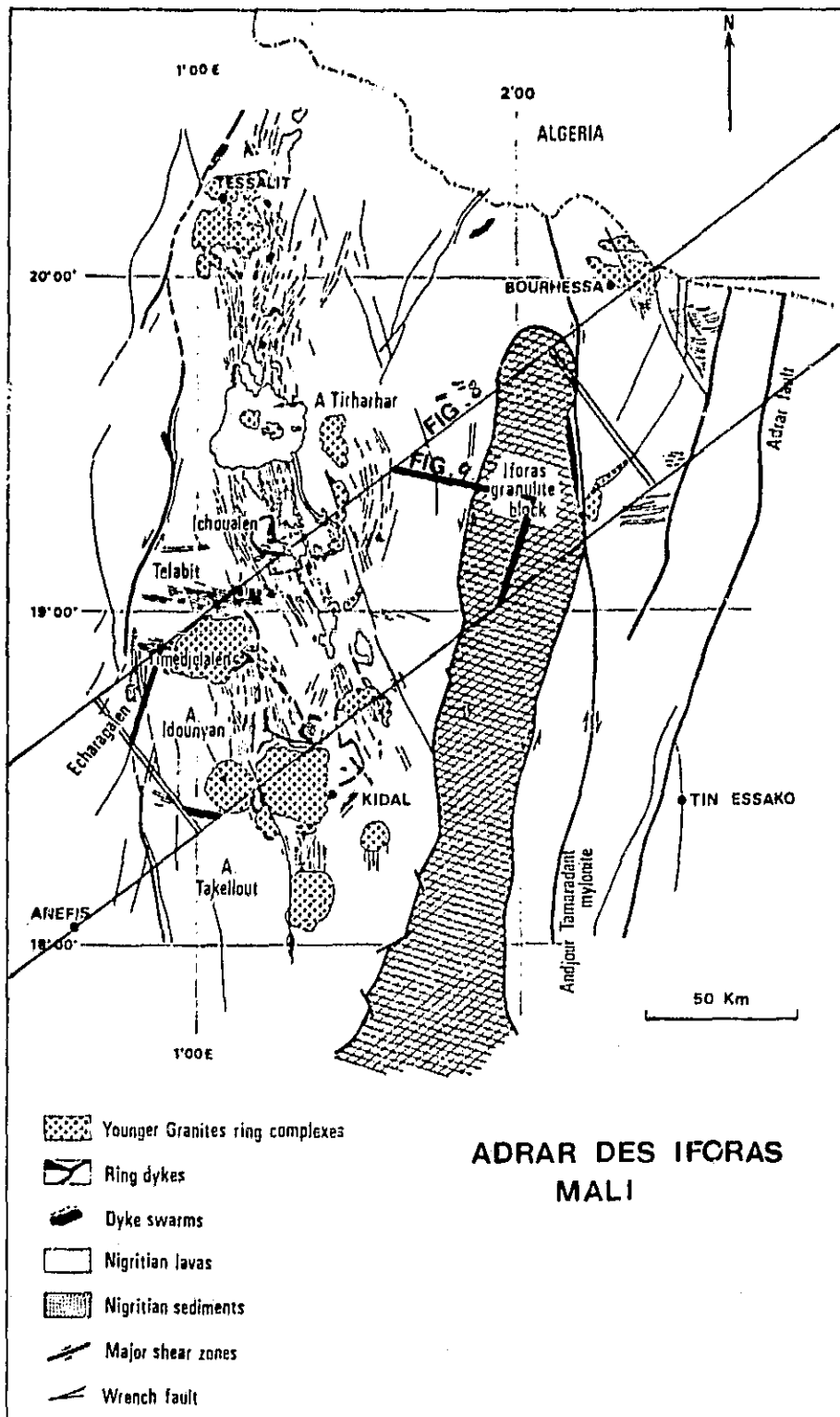
Fig. 7. Geology of Adrar des Iforas, northeast Mali, after
         Black, R., et al. (1979).

Fig. 8. SIR-A image of Idounyan and Kidal area, Adrar des Iforas, Mali. Nominal scale 1/500,000. (North to top right corner.)

Fig. 9. Landsat MSS sub-scene of Idounyan and Kidal area, Adrar des Iforas, Mali. Nominal scale 1/500,000. (Bands 7 enhanced and mosaicked on Hunting's image processor HIPAS.)

USE OF RADAR IMAGE TEXTURE IN GEOLOGIC MAPPING

Tom G. Farr

Jet Propulsion Laboratory,
California Institute of Technology
Pasadena, California

I. GENERAL

Radar images of heavily vegetated areas are dominated by diffuse backscatter from the vegetation canopy. Little or no energy is returned from the underlying ground surface. Since radar backscatter cross-section is inversely proportional to the local incidence angle for vegetation canopies (Birrer et al., 1982), brightness in radar images of these areas is a function of slope. Slope variations are expressed on these radar images as tonal variations on the scale of a few picture elements (pixels) to a whole image. Tonal variations on this scale are termed "image texture."

Brightness is greatest for slopes oriented normal to the radar beam; hence radar sensors are most sensitive to slope angles nearly equal to their nadir angles. For example, the small nadir angle of the Seasat SAR enhances small slope angles near its nadir angle (20 degrees). In contrast, the Shuttle Imaging Radar (SIR-A) was more sensitive to larger slope angles, near its nadir angle of 47 degrees. The two systems are therefore complementary, with Seasat best at portraying small slope angles and SIR-A better for steeper slopes.

The complementary nature of images obtained at different nadir angles was pointed out by MacDonald and Waite (1971), and has been exploited in the case of Seasat and SIR-A (Farr, 1982). Further variation in nadir angle will be obtained by SIR-B, scheduled for 1984, which will obtain images at six nadir angles from 15 to 60 degrees.

The analysis of image texture has been the subject of studies for several years (e.g., Haralick, 1979; Irons and Petersen, 1981). Techniques developed to analyze texture make use of statistical or Fourier transforms of image subareas to describe different scales of tonal variations.

Geologic interpretation of the information contained in Fourier transforms of radar images has received little attention. However, Pike and Rozema (1975) used one-dimensional variance (power) spectrum analysis to study topographic profiles over various sites of differing rock type, climate, and geomorphic history. They found that: (a) the integrated variance spectrum is a good measure of overall "roughness", (b) the slope of the variance spectrum in log-log coordinates was proportional to the relative strengths of large- vs small-scale topography, and (c) topographic periodicities were observed as peaks in the variance spectrum. The integrated variance can be related to the resistance of the rocks underlying the area, its tectonic history, or climatic factors. Thus, it may be inversely proportional to the geomorphic "maturity" of an area. The slope of the spectrum is also probably related to geomorphic maturity through the effects of the development and integration of small-scale drainage. Periodicities in the variance spectrum may be the result of jointing or bedding indicative of granitic or sedimentary rock types.

Detailed study of small subareas of images can lead to better understanding of the geologic and geomorphic factors operating in small areas, but it is also desirable to produce a map of geologically meaningful textural variations over large areas. One technique that can be used to map textural variations was described by Blom and Daily (1982). The technique involves production of images that represent only certain scales of texture. This is accomplished by filtering the Fourier transform of an area into several spatial frequency bands and producing an image for each of these bands. These bandpass images are then used in a standard, unsupervised classification algorithm to produce a map, the units of which represent unique textural signatures. One could also use images in which pixels represent local variance, or other statistical quantities, in different size boxes in the classification algorithm. These techniques not only discriminate units based on texture, but produce a spatial frequency signature for the units as well. These signatures allow comparison of units between maps and may allow identification of rock types if adequate knowledge exists about climate, tectonic history, and the response of different rock types to these factors.

II. CONCLUSIONS

The techniques discussed here are being developed to aid in the geologic interpretation of SAR images. The application presented here is for an area of heavy vegetation, where very little other data can be obtained directly from remote sensing images. As understanding of the relationships between image texture, topography, lithology, geomorphology, and climate improves, textural information from SAR images may be used for the identification of rock types as well as the discrimination of units. An active program is being pursued at JPL to integrate textural information from radar images directly with backscatter data from the same images, and with compositional information derived from visible-near infrared sensors such as Landsat (e.g., D. L. Evans, this symposium). The role of quantitative textural information in this type of multisensor analysis promises to be significant.

ACKNOWLEDGMENTS

REFERENCES

Birrer, I. J., E. M. Bracalente, G. J. Dome, J. Sweet, and G. Berthold, 1982, σ^0 signature of the Amazon rain forest obtained from the Seasat scatterometer, IEEE Trans. Geo. Rem. Sens., Vol. GE-20, 11-17.

Blom, R., and M. Daily, 1982, Radar image processing for rock type discrimination, IEEE Trans. Geo. Rem. Sens., Vol. GE-20, 343-351.

Farr, T. G., 1982, Geologic interpretation of texture in Seasat and SIR-A radar images, Proc. Int. Soc. Photogram. Rem. Sens., Vol. 24-VII/1, 261-270.

Haralick, R. M., 1979, Statistical and structural approaches to texture, Proc. IEEE, Vol. 67, 786-804.

Irons, J. R., and G. W. Petersen, 1981, Texture transforms of remote sensing data, Remote Sens. Env., Vol. 11, 359-370.

MacDonald, H. C., and W. P. Waite, 1971, Optimum radar depression angles for geologic analysis, Mod. Geol., Vol. 2, 179-193.

Pike, R. J., and W. J. Rozema, 1975, Spectral analysis of landforms, Ann. Assoc. Amer. Geog., Vol. 65, 499-516.

MAPPING AND MONITORING RENEWABLE RESOURCES WITH SPACE SAR

F. T. Ulaby, B. Brisco, M. C. Dobson, and S. Moezzi

Remote Sensing Laboratory, University of Kansas
Lawrence, Kansas

An examination of Seasat-A SAR and SIR-A imagery was conducted to evaluate the quality and type of information that can be extracted and used to monitor renewable resources on Earth. Two tasks were carried out: (1) a land-cover classification study utilizing (a) two sets of imagery acquired by the Seasat-A SAR, (b) one set by SIR-A, and (c) one Landsat set (4 bands) and (2) a change-detection study that examines differences between pairs of Seasat-A SAR images and relates them to hydrologic and/or agronomic variations in the scene.

I. LAND-COVER CLASSIFICATION

On November 11, 1981, the SIR-A system acquired SAR imagery of Oklahoma (Data Take 22, Orbit 18). A low-altitude aircraft obtained color infrared (CIR) photography of a portion of the area imaged by the SIR-A radar, on the same day, for ground-truth purposes. During August of 1978, the Seasat-A satellite imaged an area, part of which was the same as that described above, on both descending (August 20, Rev. 774) and ascending (August 21, Rev. 795) orbits. The overlap region of these data sets determined the location of the study area for the Oklahoma land-cover classification analyses.

Five categories that dominated the land-cover in the study area were selected for the analyses: cultivated (bare, grain, and hay fields) forest, pasture, urban, and water. Both per-pixel and per-field (on a sub-field basis) maximum-likelihood supervised classifications were performed on each SAR image and on dual-channel Landsat data (bands 5 and 7). The radar and Landsat data were then combined on a per-field basis, in various combinations, and then reclassified using the same algorithm. All classification results were calculated as a weighted overall percent correct classification of the testing data. A 10-percent random training sample, with a 90-percent testing sample, was used for the per-pixel analyses, while the per-field analyses utilized a random 50-percent training sample with the remaining 50 percent sample used for testing purposes.

The best per-pixel classification, 71.8 percent correct classification, was achieved with the SIR-A data. Both Seasat-A passes produced similar accuracies of approximately 50 percent. The Landsat dual-channel data produced an intermediate accuracy of 62 percent. In all cases the per-field classification accuracy was greater than the per-pixel results. This improvement was much better for the SAR data (14 percent) than for the Landsat data (4 percent). This was attributed to a reduction in fading of the SAR data by the averaging process.

The combination of Landsat data with SAR data always resulted in increased classification accuracies. This improvement was least for the SIR-A

data (1.8 percent) and greatest for the ascending Seasat-A image (25.8 percent). An intermediate increase (12.9 percent) in classification accuracy was achieved by combining the descending Seasat-A image with the Landsat data. The overall best classification accuracy was obtained with a combination of all three SAR data sets (97.44 percent). This was largely due to the combination of the ascending Seasat-A pass with the SIR-A data, which produced 96.77 percent correct classification. The combination of the descending Seasat-A image with the SIR-A data produced an accuracy of 87.1 percent. An accuracy of 82.1 percent was achieved by combining the two Seasat-A data sets.

II. CHANGE DETECTION

The second component of this study treats the potential of orbital SAR imagery for change detection over land surfaces, and specifically the application of multi-date Seasat-A SAR imagery to hydrology and agronomy. The radiometric stability and geometric characteristics of digitally processed Seasat-A SAR imagery are briefly discussed with respect to multi-date machine processing for change detection. SAR imagery from three ascending orbital tracks over Garden City, in southwestern Kansas, during late September and early October 1978 provides examples of (a) soil moisture change related to incident rainfall and irrigation with subsequent evapotranspirative dry-down, and (b) change related to field tillage practices such as planting and harvest.

The Garden City study area encompasses a region characterized by intensive irrigation, carried out largely by center-pivot sprinkler systems but also by gravity-flood systems. The prevalence of irrigation decreases from southwest to northeast across the area. The area is split by the Arkansas River which, in general, demarks a region of silt loam soils to the north and sandier soils to the south. From September 17 to 21, 1978, rainfall fell primarily on the extreme southeastern portion of the study area, and a subsequent storm on September 25 and 26, 1978, deposited additional rainfall on the eastern portion of the study area. The latter storm is bracketed by Seasat-A SAR overpasses on September 22, October 1, and October 7, 1978. Based upon a series of control points, defined by identifiable extended targets such as center-pivot irrigated fields, the ground area common to all three SAR images is clipped and translated into a common coordinate system; no rotation or rescaling was necessary to achieve coregistration judged accurate to within +/- 1.5 pixels, or within about 30 meters. Additional image clipping to delete areas with range ambiguities and/or offsets reduces the net registered study area to 72 km in range by 40 km in azimuth. Each of the three images is then resampled as a 2 x 2 average both to reduce the total size of the matrix and, most important, to reduce speckle related to Rayleigh fading. The resultant subscenes are then subjected to differencing and ratioing to yield a measure of change in backscatter response between SAR overpass dates. Subsequent filtering and digital enhancement yield change maps that are related to both the hydrodynamics and the agronomic activities that transpired between image acquisition dates. The magnitude of change is approximately related to physical changes within the scene based upon truck-mounted and airborne scatterometer measurements at 1.6 GHz with HH polarization at angles of incidence near 20 degrees.

The most significant conclusions of this study are:

(1)   The detection of volumetric soil moisture change related to incident rainfall and subsequent evapotranspirative dry-down appears to be on the order of 0.01 to 0.02 g/cm^3 from Seasat-A SAR.

(2)   Change is readily detectable within agronomic field units and can be related (not necessarily unambiguously) to field tillage operations and/or irrigation. Thus a strong potential exists for monitoring irrigation scheduling and the seasonal progression of field preparation, planting, and harvesting.

(3)   The geometric fidelity of Seasat-A SAR imagery readily facilitates multi-date image registration, and system-related range offsets are readily detectable (although not necessarily correctable).

(4)   Radiometric fidelity of the digitally processed Seasat-A SAR imagery related to gain offsets can be detected and approximately corrected.

(5)   Filtering of the four-look images is necessary prior to change detection analyses in order to reduce the high spatial frequency speckle related to Rayleigh fading.

(6)   A combination of filtering and digital enhancement can yield map products of low spatial frequency change related to the interaction of meteorologic events and soil-water dynamics and of high spatial frequency change related to agronomic practices on a field-by-field basis.

CROP IDENTIFICATION OF SAR DATA USING DIGITAL TEXTURAL ANALYSIS

Daniel R. Nuesch
Department of Geography
University of Zurich, Switzerland

This paper reports on a study which has been conducted in order to assess the technical value of augmenting Landsat MSS data with Seasat SAR imagery. State-of-the-art analyses were applied to both Landsat and Seasat data collected during the 1978 growing season over a NASA test segment in Jasper County, Indiana, USA. After preprocessing Seasat SAR data which included slant to ground range transformation, registration to Landsat MSS data and appropriate filtering of the raw SAR data in order to minimize coherent speckle, textural features were developed based upon the spatial gray level dependence method (SGLDM) so as to compute Entropy and Inertia as textural measures. The results obtained indicate that the consideration of texture features are very important in SAR data analysis. The Seasat SAR data were found to be useful for the improvement of field boundary definitions and also for an earlier season estimate of corn and soybean area location than is supported by Landsat alone.

I. INTRODUCTION

In the preparation period of future spaceborne radar missions like the American SIR-B, the European ERS-1 or the Canadian Radarsat, it seems appropriate to dedicate some time to basic research in order to be able to handle the enormous problems which will occur after launch date for the data analysts. One of these problems is the fact that due to the coherent nature of SAR data, it is difficult to successfully adapt statistical pattern recognition methods as they were applied to Landsat MSS data.

Several studies have demonstrated that microwaves may be used to discriminate different crop types (Refs. 1-5) but no investigations have yet been reported in which large area crop inventories were carried out successfully using digital SAR data. Although texture is one of the more important characteristics used by humans to identify objects of interest in an image, the application of classification procedures involving image texture to remote sensing agricultural surveys has remained primarily a research topic due to the magnitude of the computational resources required to achieve a reasonable throughput. In this paper I am going to review the filtering approach as well as the use of digital texture measures for classification of SAR imageries.

II. DATA PREPROCESSING

The whole process of data preparation as recording, digitization, slant to ground range correction, and registration to Landsat MSS data is discussed in Ref. 6. The presence of coherent speckle in SAR imagery precludes a pixel-by-pixel classification unless the data are highly smoothed. I applied a nonlinear isotropic filtering algorithm using neighborhood processing as implemented in ERIM's Cytocomputer TM (Ref. 7). Neighborhood processing allows spatial processing to be done directly in the image domain (Refs. 8, 9).

The underlying image algebra allows digital processing algorithms to be expressed in terms of probing images with other images (structuring elements) in a translationally invariant way. In particular, neighborhood processing can be used to reduce speckle noise while preserving field boundaries. Isotropic filtering consists of a sequence of dilations and erosions using structuring elements shaped like disks. Disks of small radius are employed to clean up noise; disks of larger radii increasingly eliminate deviations from the average tone, providing a local approximation to the mean value of individual agricultural fields. The result of this procedure is called a "local tone" image.

When local tone is subtracted in the next step from the original SAR image, an image is obtained which contains textural features, namely local spatial distributions of tonal values within an image. Adding a bias value of 128 enables both positive and negative deviations from the local tone to be easily viewed on a digital display. In a sense this image called "texture-image" depicts the information which would be discarded if analysis was limited to the local tone image and therefore served as input to the following texture analysis.

III. TEXTURE ANALYSIS

Reviewing the literature on texture models (Refs. 10, 11), there is strong supportive evidence, that the Spatial Gray Level Dependence Method (SGLDM) is representative of the best texture algorithms currently available. Initially, it is assumed that the texture context information in an image is contained in the overall or "average" spatial relationship which the gray tones in the image have to one another. This relationship can be characterized by a set of co-occurrence matrices $P(i,j)d, \theta$ whose i,j^{th} element is the relative frequency with which two neighboring picture elements separated by distance d in a direction θ occur in the image, one with gray tone i and the other with gray tone j.

The computation of the texture measurement values involved three steps. First the "texture" image was level-sliced into a smaller number of intervals in order to ease the computational burden. The next step consisted of calculating the co-occurrence matrices over a moving window using a displacement distance d = 2 and four different angles $\theta = 0^{\circ}$, 45°, 90° and 135°. Textural features (scalar functions) were then computed from these co-occurrence matrices. In order to obtain texture measures which are insensitive to the orientation of the sensor, I chose to use the average value of a texture measure over all four angles. The scalar functions which were employed are called Contrast or Inertia and Entropy. Their mathematical definitions are:

$$\text{Inertia} \quad d,\theta = \sum_{i=1}^{N_G} \sum_{j=1}^{N_G} (i-j)^2 P(i,j)$$

$$\text{Entropy} \quad d,\theta = \sum_{i=1}^{N_G} \sum_{j=1}^{N_G} P(i,j) \log P(i,j)$$

where N_G is the number of gray levels used.

What makes the co-occurrence approach so valid is its character-
ization of the spatial interrelationship of the gray tones in a textural
pattern in a manner which is invariant under monotonic gray tone transform-
ations. Moreover, as implemented here, no a priori knowledge of the location
of field boundaries is required.

Although the spatial resolution element of the Seasat SAR is sub-
stantially larger than the row spacings in wheat, corn or soybean fields,
certain within-field textural variations are evident in the image. In
relating the computed texture measurement values to specific crop types, the
texture feature information will not be regarded as a replacement but rather
as an addition to the other features such as spectral, temporal and spatial
information. Up to this point no machine classification of the "Inertia- or
Entropy-Image" has been performed, because the data are not gaussian distri-
buted. However, the images were quantized empirically and in the case of corn
and soybean discrimination the thresholded Inertia image produced a fairly
good representation of the soybean field. The major sources of error came
from the inclusion of grass, pasture, trees and grain and could be eliminated
by using information from an early Landsat acquisition data to separate out
areas which were healthy green vegetation prior to the time when corn and
soybeans had greened up.

ACKNOWLEDGMENTS

REFERENCES

1. Schwarz, D. E., and Caspall, F. C., 1968, "The Use of Radar in the Dis-
    crimination of Agricultural Land Use," in Proc. 5th Int. Symp. on Remote
    Sensing of Environment, pp. 233-248.

2. Haralick, R. M., Caspall, F. C. and Simonett, D. S., 1970, "Using Radar
    Imagery for Crop Discrimination: A Statistical and Conditional Prob-
    ability Study," in Remote Sensing of Environment, Vol. 1, pp. 131-142.

3. Bush, T. F., and Ulaby, F. T., 1978, "An Evaluation of Radar as a Crop
    Classifier," in Remote Sensing of Environment, Vol. 7, pp. 15-36.

4. Brisco, B., and Protz, R., 1982, "Manual and Automatic Crop Identifi-
    cation with Airborne Radar Imagery," in Photogrammetric Engineering and
    Remote Sensing, Vol. 48, No. 1, pp. 101-109.

5. Ulaby, F. T., Li, R. Y., and Shanmugan, K. S., 1982, "Crop Classification
    Using Airborne Radar and LANDSAT Data," in IEEE Trans. on Geoscience and
    Remote Sensing, Vol. GE-20, No. 1, pp. 42-51.

6. Nuesch, D. R., 1982, "Augmentation of LANDSAT MSS Data by SEASAT SAR Imagery for Agricultural Inventories," Reprint of NASA-Report IT-E2-04233 in the Remote Sensing Series, Vol. 7, Dept. of Geography, University of Zurich, Switzerland.

7. Sternberg, S. R., 1979, "Automatic Image Processor," U. S. Patent, 4.167.728, Sept. 11, 1979.

8. Lougheed, R. M., et al., 1980, "The Cytocomputer: A Practical Pipeline Image Processor," 7th Annual Int. Symp. on Computer Architecture, La Baule, France, IEEE Publication 80CH1494-4C, pp. 271-277.

9. Sternberg, S. R., 1980, "Language and Architecture for Parallel Image Processing," Proc. Conf. on Pattern Recognition in Practice, Amsterdam, The Netherlands.

10. Haralick, R. M., et al., 1973, "Textural Features for the Image Classification, IEEE Trans. Systems, Man & Cybernetics, Vol. SMC-3, Nov. 1973, pp. 610-621.

11. Conners, R. W., et al., 1981, "Toward a Structural Textural Analyzer Based on Statistical Methods," in Image Modeling, Azriel Rosenfeld (ed), New York, Academic Press, pp. 29-62.

C - 2

THE SIR-A ATLAS

J. P. Ford
Jet Propulsion Laboratory, California Institute of Technology
Pasadena, California

On November 12, 1981, the Space Shuttle Columbia carried its first scientific payload into Earth orbit. Part of this payload was the Shuttle Imaging Radar system (SIR-A). The objectives of the SIR-A experiment were to acquire radar images of a wide variety of different geologic terrains around the Earth, to demonstrate the capability of the Shuttle as a platform for conducting spaceborne scientific investigations, and to analyze and interpret the data in the radar images. The SIR-A sensor imaged about 10 million km^2 of the Earth's surface. High resolution images were acquired over portions of every continent and some of the oceans between latitudes 41°N and 35°S. The SIR-A incidence angle ranges from 47 deg to 53 deg across an image swath of approximately 50 km.

An atlas of 60 selected SIR-A images has been assembled to demonstrate the capability of this microwave system for perceiving and mapping a wide range of Earth surface features. The geographic location of the images is shown in Fig. 1. Each SIR-A image in the atlas is presented in conjunction with one or more different spaceborne images for comparative purposes, or with a sketch map or photograph for illustration of features described in the text. The companion image or images are subscenes mostly from Landsat multispectral scanner (MSS) or Seasat synthetic-aperture radar (SAR) images. There is one example each of a Heat Capacity Mapping Mission (HCMM) scene and of SIR-A repetitive coverage. Differences in feature perception on the SIR-A images and on corresponding images acquired with Landsat MSS, Seasat SAR, or HCMM are in each case related mostly to differences in the viewing geometry, illumination direction, or wavelength of the respective imaging systems. The interval between the acquisition of the SIR-A image and the corresponding image(s) of each scene ranges from 1 1/2 h to 9 yr and 3 mo. In many scenes the SIR-A and companion images record major changes in surface features that resulted from either natural phenomena or human activities.

Each SIR-A image in the atlas covers an area of approximately 100 km in azimuth by 50 km in range. Together the images represent about 3 percent of the total SIR-A coverage. The images are grouped under nonrenewable resources, renewable resources, oceanographic features and man-made features. The Earth's topography and landforms provide important information concerning this planet's natural nonrenewable resources. Topography is enhanced on SIR-A images, particularly in hilly or mountainous areas where the slopes are 20 deg or more. Structures such as folds, faults, and bedding are readily perceived from the image patterns and the contrasts in image tone and texture. Fold and fracture patterns are clearly displayed on SIR-A images, both in areas of extensive rock outcrop and in areas that are heavily vegetated. Circular features that appear enhanced by the radar response to surface morphology include eroded dome structures, curvilinear fracture patterns, granite plutons, salt domes, and volcanic cones of varying dimensions. Erosional landforms in dissected terrains are enhanced by the strong contrast in radar backscatter from the upland surfaces and the lowland valleys.

The SIR-A coverage provides the first clear spaceborne images of the topography and structures in remote, inaccessible, perennially cloud-covered areas. Limitations that exist in the perception of dune morphology are governed by the orientation and form of the dunes, and by the local incidence angle. In areas where the surfaces are relatively level, such as dry lakes or deltaic plains, the SIR-A image tones of surface features are strongly influenced by the small-scale roughness characteristics of the surface materials. Modulation of the SIR-A backscatter by slope and by surface roughness characteristics provides distinctive image textures in areas of extensive karst topography.

The Earth's renewable resources imaged by SIR-A are grouped here under hydrology - drainage networks, agriculture, forest cover, and urban areas. The perception of drainage channels on the SIR-A images is largely dependent on the local image contrast along and adjacent to the channel. The wide channels of major trunk streams are readily discerned from the dark tone of the water. Narrow channels of low-order tributaries may be outlined by the radar returns from riparian vegetation or, in the case of dry channels, from deposits in the channel. Significant alterations in stream channels that have undergone extensive flooding are apparent by comparing the SIR-A image with the corresponding Landsat MSS coverage acquired years earlier; this technique can also be applied to detect man-made changes on a floodplain. A single example of mountain valley glaciers shows a pronounced structural control of the drainage pattern. SIR-A images of agricultural scenes commonly show image tones inverse of those on Landsat band-5 images. This occurs where an active vegetation canopy yields multiple backscatter at the radar wavelength but is strongly absorptive at the visible-red wavelength. SIR-A backscatter from circular fields is related to multiple reflections from standing crops and to specular reflection and/or Bragg scattering from plowed furrows. Changing patterns of agriculture are evident by comparing SIR-A coverage with corresponding images acquired earlier by Landsat MSS or Seasat SAR. Forest canopy produces a generally uniform tone on SIR-A images. Urban areas show systematic changes in radar reflectivity from buildings; these changes depend on the orientations of the reflecting surfaces.

Numerous oceanographic features were observed with SIR-A despite the high incidence angle and the generally low radar backscatter from the ocean surface. Surface waves, windrows, and large internal wave trains imaged by SIR-A corroborate previous observations of the oceans made by Seasat SAR. Two successive orbital passes, separated by 1 1/2 h provide some information about the formation of surface disturbances due to local wind variations. Examples of other features observed include surface slicks, eddies, squall lines, and the dampening effect of rain cells. Vessels appear as very bright targets, as they do on Seasat SAR images; however very few ships' wakes were observed.

Evidences of human activity or occupation are widely represented in the SIR-A coverage. Structures such as routeways, transmission lines, canals, and bridges may appear bright or dark on SIR-A images depending on the orientation of the reflecting surfaces relative to the radar illumination. Platforms and structures that behave as point-target reflectors appear very bright.
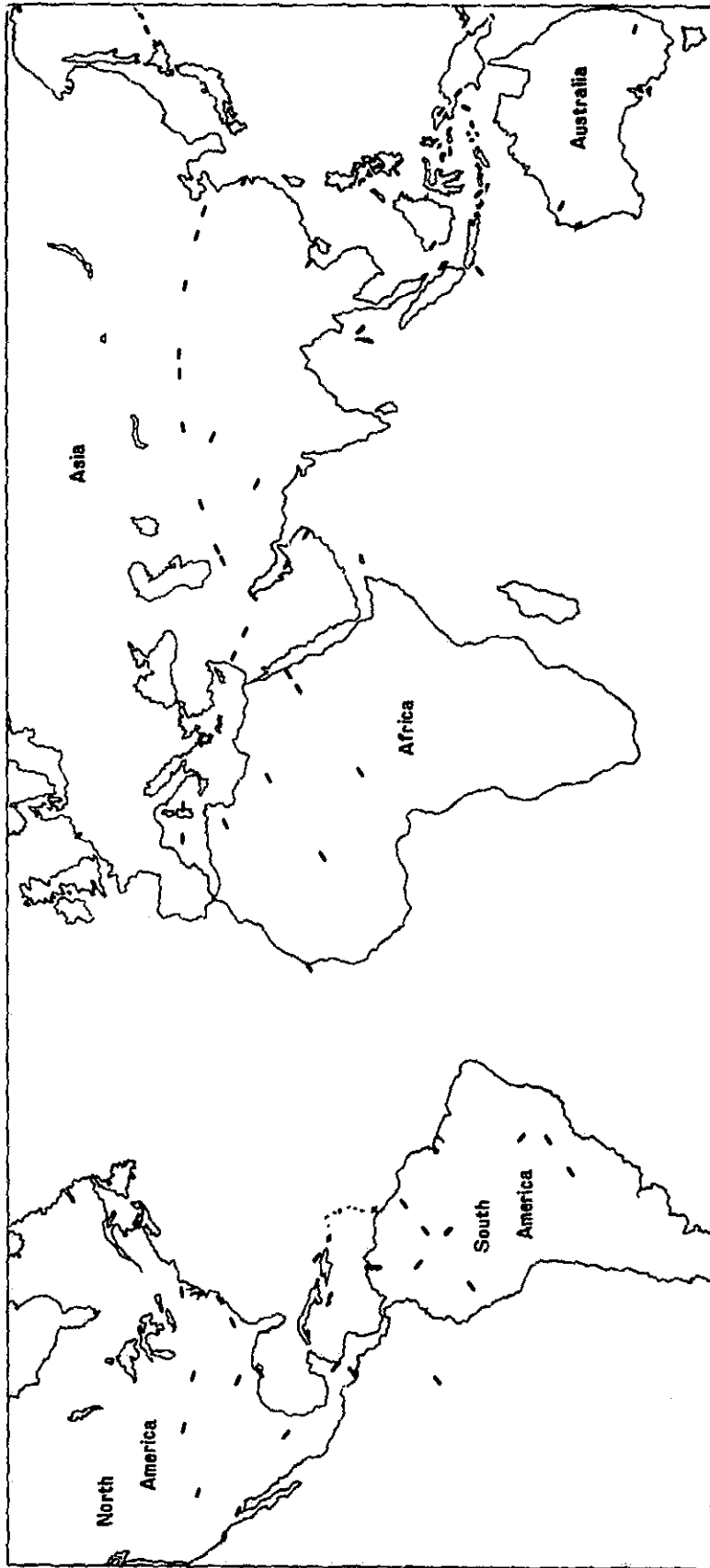
Fig. 1. Black rectangles show geographic location of SIR-A atlas images.

Processor Technology

PROCESSOR ARCHITECTURE FOR AIRBORNE SAR SYSTEMS

C. M. Glass
Goodyear Aerospace
Litchfield Field, Arizona

I. INTRODUCTION

In considering digital processors for spaceborne imaging radars, one is motivated to see how technology developed for airborne SAR systems can be of use. Transferring algorithms and implementation techniques from airborne to spaceborne SAR processors offers obvious advantages. This paper consists of (1) a quantification of the differences in processing algorithms for airborne and spaceborne SARs and (2) an overview of three processors for airborne SAR systems.

II. PROCESSING REQUIREMENTS

To compare processing rates for spaceborne and airborne SAR, assume a side-looking, strip-mapping system such as Seasat. Convolutional matched filtering implemented by FFTs is used for both range and azimuth compression. The range FFT length is the sampled equivalent of the slant range swath width plus one pulse duration. The azimuth batch length is twice a synthetic aperture. For simplicity, both range and azimuth sampled batch lengths are assumed to be integral powers of two.

A.   Range Processing Rate

Range processing is dominated by the multiplications needed to do the FFT operations. Let r_R be the number of real multiplications per second required for range compression; then,

$$r_R = (K/W_{Rs}W_A) \cdot (\log_2 N_R) \cdot (\Delta R_s + c\tau/2)V \quad \text{real multiplications/s,} \quad (1)$$

where the number of N_R of range samples across the swath is given by

$$N_R = (0.885k_{oR}k_R c/2W_{Rs}) \cdot (2\Delta R_s/c + \tau) \quad \text{complex samples.} \quad (2)$$

In these equations, W_{Rs} = slant range resolution, W_A = azimuth resolution, ΔR_s = slant range swath width, c = propagation velocity, τ = transmitted pulse duration, V = vehicle velocity, k_R and k_A are range and azimuth excess bandwidth factors to allow for sidelobe weighting and k_{oA} and k_{oR} are azimuth and range oversampling factors. Constant K is given by $K = 4(0.885)^2 k_{oR}k_{oA}k_R k_A$.

Constant k_{oR} is in the range $1.1 \le k_{oA} \le 1.5$; k_{oA} is in the range $1.25 \le k_{oA} \le 1.5$, and for Taylor weighting, $k_R = 1-(PSLR+13)/65$, where PSLR is the desired sidelobe weighting in dB (and similarly for kA). Resolutions W_{Rs} and W_A are weighted, 3-dB impulse response widths.

If the swath width, resolutions, oversampling factors, and pulsewidth are made identical for the airborne and spaceborne systems, the only parameter which differs is the platform velocity. The real multiplication rate for range processing is then directly proportional to the velocity. Consider an orbiting SAR with $V = 24,000$ ft/s versus an airborne SAR with $V = 800$ ft/s (545 mph).

If the processor is designed so that the arithmetic hardware operates at its maximum rate, then a real-time spaceborne range processor would need $24,000/800 = 30$ times as much arithmetic hardware as would the comparable airborne system.

B. Azimuth Processing Rate

Azimuth processing is also dominated by FFT multiplications. One batch of length $2L_s$, where L_s is the synthetic aperture length, must be processed each integration time T_1, where $T_1 = L_s/V$. Processing requires two FFTs per range cell, and N_R range cells must be processed. The real azimuth multiplication rate, r_A, is then

$$r_A = k_A(8(0.885)k_{oA}N_R/W_A) \cdot (\log_2 2N_A)V \quad \text{real multiplications/s}, \tag{3}$$

where the number N_A of samples in a synthetic aperture is

$$N_A = (0.885)^2 k_{oA} k^2 A\lambda R_{sm}/2W_A^2 \quad \text{complex samples.} \tag{4}$$

Here R_{sm} is the maximum slant range to be imaged. From Eqs. (3) and (4), it is evident that the azimuth multiplication rate depends primarily on velocity but with an additional dependence on slant range. All other parameters can be identical for comparable airborne and spaceborne systems. For example, a spaceborne SAR with $R_{sm} = 1000$ nmi, $V = 24,000$ ft/s and $N_A = 1280$ requires an azimuth multiplication rate 42 times that needed for a comparable airborne system with $R_{sm} = 100$ nmi, $V = 800$ ft/s, and $N_A = 128$. The factor of one hundred translates into a requirement for a great deal of additional hardware for real-time processing.

C. Memory Requirements

The amount of corner-turn memory for the processor is $M = 2FN_AN_R$ real words, where F is a factor the value of which is two to five depending on the architecture used. Consulting the expressions for N_A and N_R reveals that the spaceborne system requires more memory than the comparable airborne system by a factor which is the ratio of the maximum ranges of the two systems. A spaceborne system with $R_{sm} = 1000$ nmi needs 10 times as much memory as does the comparable airborne system with $R_{sm} = 100$ nmi.

D.   Motion Compensation and Range Curvature

Orbital perturbations, asphericity of the earth, and earth rotation are important considerations in motion compensation for orbital SAR; whereas platform maneuvers, both intentional and unintentional, dominate the picture for airborne systems. Processing algorithms are based on a nominal vehicle flightpath. Motion sensing equipment measures deviations from this path and uses these to fine tune the image formation algorithms. The dominant flightpath deviations are along-track velocity and acceleration along the line-of-sight vector from radar to target. Assuming that quadratic phase error dominates and that 90 degrees of center-to-end quadratic phase error is acceptable, the restrictions on uncompensated along-track velocity ΔV_x and line-of-sight acceleration Δa_y are

$$\Delta V_s < (2W_A^2 \lambda) \cdot (V/R_{sm}) \quad \text{and} \quad \Delta a_y < (4W_A^2/\lambda) \cdot (v/R_{sm})^2. \tag{5}$$

The high velocity of an orbiting SAR thus eases the motion tolerances, an effect which is somethat offset by the longer slant range.

Image degradation due to the range curvature phenomenon is negligible if the inequality $W_{Rs} < \lambda^2 R_{sm}/32 W_A^2$ is well satisfied.

Since spaceborne SARs operate at longer ranges than do airborne systems, range curvature becomes a problem for coarser resolutions for the former.

III.   REVIEW OF AIRBORNE PROCESSORS

This section is an overview of three real-time SAR processors which have been or are being developed by Goodyear Aerospace.

A.   HIRSADAP

The High-Resolution, Real-Time Synthetic Array Processor was developed for the Air Force by Goodyear in the 1971-1974 time frame. HIRSADAP had a modest 3.5 Mbit of memory implemented by 1024-kbit shift registers. Directly implemented convolution was used for both range and azimuth compression, although a later modification implemented FFT range processing. Imagery was produced in real-time for either broadside or squinted operation. Platform velocity was 250-900 ft/s, and the swath range was 2 nmi to 40 nmi depending on mode. Performance in some high-resolution modes is still classified, but one of the unclassified modes had 25-ft resolution and a 5-nmi-wide range swath. Both strip map and spotlight modes were included.

B.   SAPPHIRE

The Synthetic Aperture Precision Processor, High Reliability (SAPPHIRE) is a real-time digital SAR processor built by Goodyear Aerospace for the Air Force between 1974 and 1977. SAPPHIRE produces high-resolution imagery from a 10-nmi-mile-wide swath. Its arithmetic rate of 4×10^9 complex operations/second is, to the author's knowledge, unmatched by any other

SAR processor developed to date. Range compression is done by direct convolution. This approach appears to be inefficient compared to FFT methods but SAPPHIRE partially negates the FFT advantages by using a so-called modified interactive algorithm in which the quadratic phase function to compress the transmitted pulse is approximated by a sequence of linear-phase segments. If the number of samples per convolution is properly selected, many of the multiplications become trivial data exchanges or sign changes. The result is that modified iterative range compression is implemented with a substantial hardware savings compared to direct convolution.

SAPPHIRE azimuth processing is done by bandpass filtering the received Doppler spectrum into four subapertures.

The data from each subaperture is compressed by convolutional matched filtering into a low-resolution image. The four low-resolution images are combined coherently into a single high-resolution image. The approach has two advantages: (1) azimuth memory needed to support four subapertures is only 5/8 of that required for a single high-resolution aperture; (2) the effect of range curvature is reduced by a factor of 16 compared to single-aperture processing. This is because range curvature degradation is proportional to the square of synthetic aperture length.

SAPPHIRE algorithms were dictated by the integrated circuits available at the time. Although the processor has "only" 30 Mbit of memory, memory was a design driver using the 2048-bit shift registers available at the time of development.

C.   The Ring Processor

The SAR processing dilemma is that while parallel/pipeline processors can be custom built to meet any reasonable requirements, these devices are quite expensive. On the other hand, commercial array processors are more economical by virtue of being in high volume production, but they suffer from such low computational rates as to be cost ineffective for real-time, high-resolution SAR processing.

Goodyear Aerospace has under development a processor which will bridge the gap between custom processors and array processors. This device consists of a ring of plug-in computing modules distributed around a high-speed ring data bus. Data is routed to the modules under control of a host microcomputer.

Module types are (a) FFT, (b) convolutional FIR filter, (c) reference function generator, and (d) corner-turn memory. Flexibility for various SAR missions is achieved in three ways: (1) the computing modules and the sequence in which they are called are reconfigured under software control, (2) plug-in modules are added or deleted to size the processor, and (3) the entire processor can be treated as a module — as a range subswath processor, for example.

92

PERFORMANCE EVALUATION OF THE JPL INTERIM DIGITAL SAR PROCESSOR

C. Wu, B. Barkan, J. Curlander, M. Jin, and S. Pang

Jet Propulsion Laboratory, California Institute of Technology
Pasadena, California

I. INTRODUCTION

This paper presents the results of a recent evaluation on the performance of the JPL Interim Digital SAR Processor (IDP). The IDP processor was originally developed in 1979 for experimental processing of digital Seasat SAR data [1]. One phase of the system upgrade was made in 1981, which features parallel processing in three peripheral array processors [2], automated estimation for Doppler parameters [3], and unsupervised image pixel location determination and registration [4-5]. Most recently, a significant improvement was made on the method to compensate for the target range curvature effect. A four-point interpolation scheme such as the one used in [6] is implemented to replace the nearest neighbor scheme used in the original IDP. The implementation was made such that the processor still maintains its fast throughput speed. This paper will update users with the current performance and capability of the processing modes now available on the IDP system.

II. CAPABILITY AND PERFORMANCE OF THE CURRENT IDP SYSTEM

Several modes of processing different resolutions and data types are now available on the IDP system. Other than the nominal 25-m resolution Seasat SAR imagery, the additional products include: (1) 6-m single-look Seasat SAR imagery produced by a precise hybrid correlation algorithm [7]; (2) 20-m resolution and multipolarization registered NASA CV-990 aircraft SAR imagery; and (3) 100-m resolution Seasat SAR frames for a survey mode [8].

The image output format can be specified in either the detected pixel intensity or the original complex form which carries the pixel phase data. The unsupervised pixel location capability can determine the absolute location of a specified pixel to within 60 m without reference to ground maps. This technique has been utilized to develop the capability for automated multiframe mosaicking. These services are currently available under special requests from users.

Example of the improved radiometric performance of the IDP using a more accurate interpolation scheme than the original nearest neighbor method is shown in Fig. 1. A quantitative measure shows a 20% improvement in resolution and a 6-dB improvement in the peak sidelobe performance. The improvement is most obvious in the Seasat SAR response to the 9-m antenna, which is the brightest object on the left-hand side of the image. Several improvements in the data handling and processing routines in this version of the IDP software were also made. The period of updating azimuth reference is now every 8 range pixels. With a more efficient overlay procedure, the overall processing time for a 100-km-square Seasat SAR frame is now slightly under two hours.

For the 6-m high azimuth resolution processing, an example is shown in Fig. 2. This picture has five of the nine Goldstone corner reflectors. The picture shown here has been interpolated to show fine details of the processor response to point targets, which closely resembles the sinc function with suppressed sidelobes.

III. SUMMARY

This paper summarizes the current status of the Interim Digital SAR Processor Development. The processor is being adapted to accommodate different types of user's needs, which include high precision and resolution processing, aircraft SAR processing, etc. Further improvement in image quality is anticipated in the design of a software package which will be able to produce a digital SIR-B image in 1984.

ACKNOWLEDGMENT

REFERENCES

[1] C. Wu, B. Barkan, B. Huneycutt, C. Leang, and S. Pang, "An Introduction to the Interim Digital SAR Processor and the Characteristics of the Associated SEASAT SAR Imagery," JPL Publication, 81-26, April 1981.

[2] B. Barkan, C. Wu, W. Karplus, and D. Caswell, "Application of Parallel Array Processors for SEASAT SAR Processing," in Proc. IGARSS '81, Vol. I, pp. 541-547, June 1981.

[3] J. C. Curlander, C. Wu, and A. Pang, "Automated Preprocessing of Spaceborne SAR Data," Proc. of International Geoscience and Remote Sensing Symposium, Munich, June 1982, Vol. 2, FA-2.

[4] J. C. Curlander, "Location of Spaceborne SAR Imagery," IEEE Trans. on Geoscience and Remote Sensing, Vol. GE-20, No. 3, July 1982.

[5] J. C. Curlander and S. Pang, "Geometric Registration and Rectification of Spaceborne SAR Data," Proc. of Inter. Geoscience and Remote Sensing Symposium, Munich, June 1982, Vol. 2, FA-1.

[6] J. Bennettm I. Cumming, and R. Deane, "The Digital Processing of SEASAT Synthetic Aperture Radar Data," Proc. of IEEE '980 Inter. Radar Conf., pp. 168-175, April 1980.

[7] C. Wu, K. Liu, and M. Jin, "Modeling and Correlation Algorithm for Spaceborne SAR Signals," IEEE Trans. Aerosp. Electron. Syst., pp. 563-575, Sept. 1982.

[8] M. Jin and C. Wu, "A Digital Quick-Look SAR Processor," Proc. of the Inter. Society of Photogrammetry Conf., Ottawa, Canada, 1982.
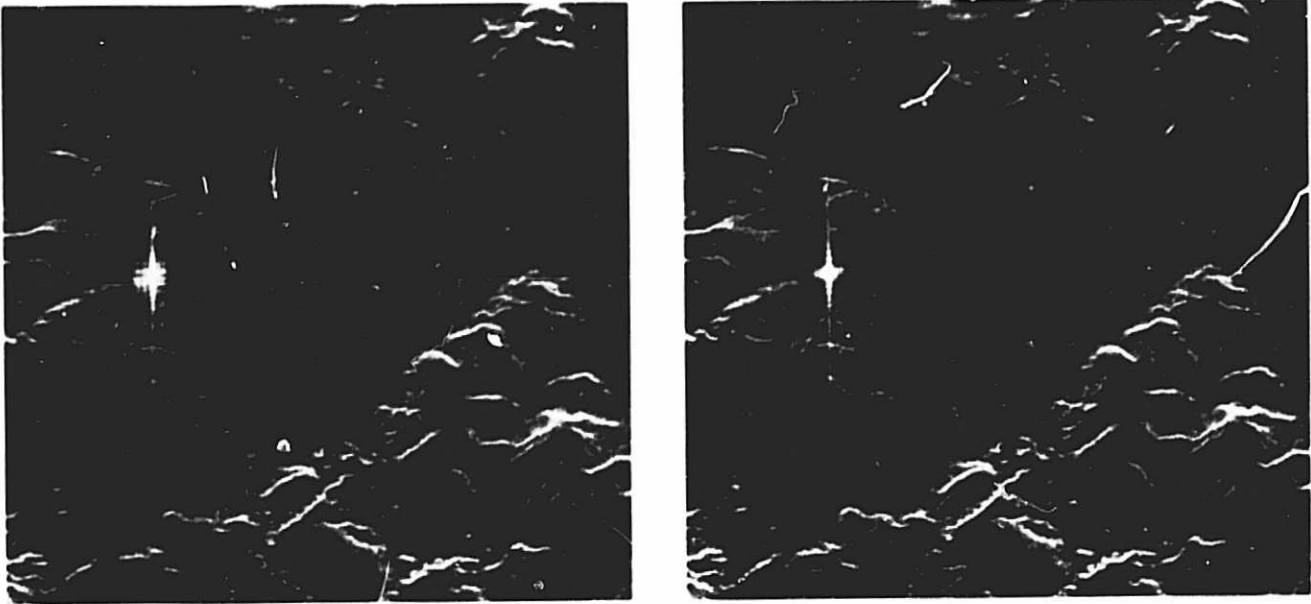
Fig. 1. Original (left) and upgraded performance (right) of the IDP on Rev. 882 Goldstone corner reflector scene.

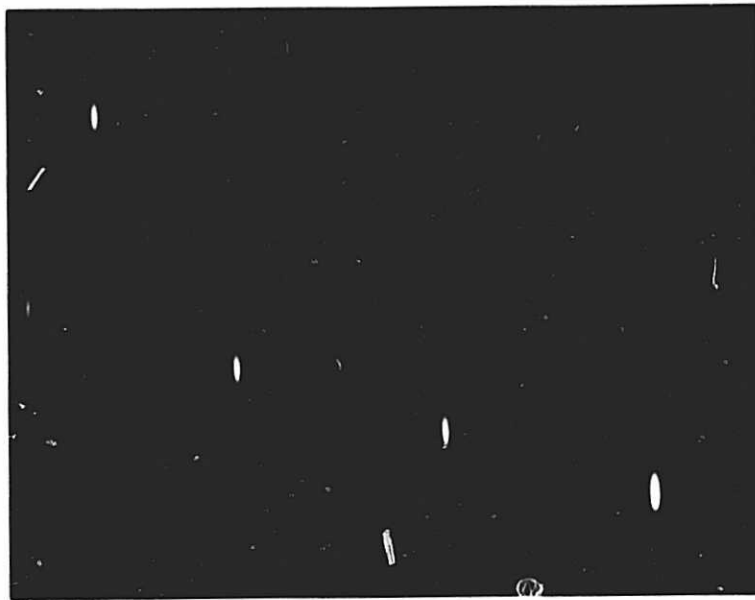Fig. 2. 6-m azimuth resolution image of five corner reflectors.

95

REAL-TIME DIGITAL PROCESSING OF SAR DATA

T. Bicknell
Jet Propulsion Laboratory, California Institute of Technology
Pasadena, California

Current SAR data processing techniques for spaceborne SAR systems utilize commerical equipment (such as array processors) to carry the computation load. For a data set such as Seasat, the resulting throughput rate is two to three orders of magnitude slower than real-time. Such rates impede the progress of scientific investigations and preclude the potential for any practical operational SAR mission. Using existing technology, a set of special-purpose hardware can be designed for efficient SAR data processing so that real-time rates are both practical and affordable.

Preliminary design of such a system has been completed. A block diagram of the overall system is shown in Fig. 1. The high input and output data rates to the system require special high density tape drives as I/O devices. These devices play back (or record) data in a continuous serial bit stream. Interfaces are required for sync detection, buffering and formatting. The remainder of the system hardware between the input and output interfaces is essentially the FFT-convolution algorithm implemented in a pipeline architecture. Although there are a large number of well-defined discrete operations, the diagram shows them grouped into four major top-level functions: range processing, corner turn memory, azimuth processing, and multi-look processing. Detailed hardware control is performed by an 8086 μprocessor in communication with a VAX 11/730 minicomputer which computes processing parameters.

The primary function in the range processor is the FFT-convolution which includes a forward FFT, a reference function multiply, and an inverse FFT. The system uses an FFT large enough to transform the whole input range line. The two FFT modules are identical and can be programmed to perform a forward or inverse FFT, FFT of real or complex input, and FFT of any length line that is a power of 2 from 2 to 2^{14} (16,384). The continuous data rate capability in each FFT is 20 MHz, resulting in a 16,384 length FFT in about 0.8 milliseconds, or for example, four 4096 point FFT's in the same time. All computations are performed with floating point arithmetic. This speed is approximately 150 times the rate of an AP120B array processor. Other functions which are performed in the range processor (when necessary) are data buffering to append zeroes to arbitrary line lengths to make them of length 2, linear interpolation for range walk by multiple reference function selection, and spectral shifting for high Doppler correction.

The corner turn memory does not involve any computation but simply performs (as its name implies) a matrix transpose. The memory is divided into three sections of 8 megawords each. Range compressed data is input in range line order into one section at 10 MHz while it is being read out of the other two in azimuth order at a total rate of 20 MHz. The double data rate is required for 50% overlap in the azimuth processing.

The azimuth processor contains two FFT modules, identical to the range FFT's, with several key elements between them operating in the azimuth transform domain. Following the forward FFT is a buffer memory and four point interpolator to resample the data along the range migration paths. In the basic processing mode, all range migration compensation is performed at this stage. Next, the reference function is supplied by a quadratic function generator and applied to the data in a complex multiplier. The data is then spectrally separated into 2, 4, 8, or 16 segments (for 2, 4, 8 or 16 looks, respectively) and input into the inverse FFT module which has been programmed for the appropriate length FFT. The single look images are detected and output to the clutter-lock and auto-focus processing as well as to the multi-look processor. Auto-focus and clutter-lock calculations are sent to the VAX host computer via the 8086 μprocessor. The VAX will determine reference function coefficients and send them back to the hardware.

In the multi-look processor, multiple looks can be obtained within a single azimuth line as well as between consecutive processing blocks. When the forward azimuth FFT is more than twice as large as the actual coherent reference function length, overlap between the successive looks within a single azimuth line will occur and they must be summed appropriately. Another large memory (totaling 32 megawords) performs two buffering functions in the multi-look processor. The first buffer stores the intermediate results of the partially summed multi-look data. The second buffer performs the transpose operation on the fully summed images to convert them back to range line order before recording.

The overall throughput of the system is up to 10 MHz (complex word rate), requiring about 6 billion floating point operations per second. Swath width capability is up to 8K complex pixels (with 1K azimuth reference function). The output is continuous slant range image corrected for Doppler skew.
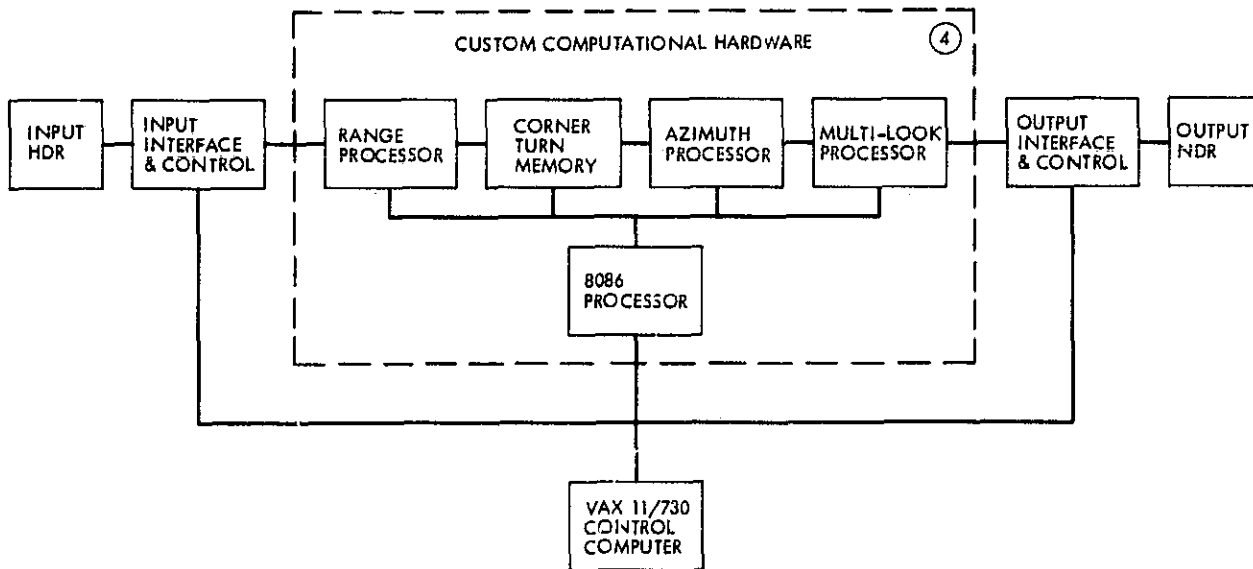
Fig. 1. ADSP (Advanced Digital SAR Processor) system diagram.

A FAST, PROGRAMMABLE HARDWARE ARCHITECTURE FOR
SPACEBORNE SAR PROCESSING

J. R. Bennett, I. G. Cumming, J. Lim, and R. M. Wedding
MacDonald, Dettwiler & Associates, Ltd.
Richmond, B. C., Canada

I. INTRODUCTION

Several countries and organizations are currently in the advanced planning stages for the launch of spaceborne SARs during the 1980's. These include Germany, USA, ESA, Japan and Canada. The satellite SARs in particular create a requirement for high quality and high throughput ground processors. Compression ratios in range and azimuth of greater than 500 and 150 respectively lead to frequency domain processing and data computation rates in excess of 2000 million real operations per second for C-band SARs under consideration. Input data rates greater than 8×10^6 samples per second and control loading up to 10^6 machine level instructions per second present further challenges to the High Throughput SAR Processor (HTSP) hardware designers. The body of this paper examines various hardware architectures, selects two promising candidates and proceeds to recommend a fast, programmable hardware architecture for spaceborne SAR processing. The concepts of Modularity and Programmability are introduced as desirable attributes for the purpose of HTSP hardware selection.

II. REVIEW OF HTSP HARDWARE ARCHITECTURES

Among the hardware architecture candidates reviewed for HTSP implementation are the following:

(1)   Commercially available:

-   Supercomputers
-   Multiple minicomputers or microcomputers
-   Mainframe computers with array processors (APs)

(2)   Custom-built:

-   Dedicated hardware systems
-   Programmable Signal Processor (PSP) systems

Based on their Modularity and Programmability as well as other factors the two candidates selected for further consideration are Mainframe or Host/AP systems and Programmable Signal Processor systems.

Limitations of Host/AP implementations of a High Throughput SAR Processor (HTSP) are examined from historical, economic and technical perspectives. General vector computing tasks which inspired array processors are discussed briefly and compared to specific SAR vector tasks. A resistance to improvement in cost to speed ratio for SAR operations is analyzed. Finally, technical difficulties encountered for the SAR application are discussed in

terms of hardware configurations and software development risks. Major concerns with respect to a Host/AP architecture for HTSPs are summarized in terms of cost and risk.

In response to the difficulties encountered with Host/AP architectures in high speed SAR applications a Distributed Control and Data Path Processor (DPP) architecture has been derived. The DDP is comprised of Programmable Signal Processing Elements (PSPEs). Figure 1 depicts a typical high speed processor implementation of this architecture. The distributed control applies both to the microprocessors of the Processor Control Systems (PCS) and the micro and nano controllers of the PSPEs themselves. Advantages of vertical and horizontal control partitioning are described. Data handling and fully concurrent control and data computation strategies are outlined. Advantages of the PSPE architecture are summarized in terms of low incremental unit cost, predictable system costs and low technical risk.

The performance of a Programmable Signal Processing Element (PSPE) designed at MDA is discussed in the next section. A laboratory bench model of the PSPE was demonstrated to operate at full speed in March 1982. The PSPE has a 200 nanosecond compound operation cycle time and can perform 5 million FFT butterflies per second, a rate which is comparable to that of new generation high speed array processors (APs). The physical dimensions of the PSPE kernel are approximately 9" x 8" x 17", compared to 30" x 54" x 60" for a new generation AP operating at similar speeds. The reduced PSPE volume is a reflection of reduced functionality and lower cost per repeat unit.

The internal architecture of the MDA PSPE is shown in Fig. 2. The separate input/output buffers and working buffers shown in the diagram support fully concurrent data transfer and data computation within the PSPE.

III. SUMMARY

To summarize qualitative arguments in a concrete form, a graph of cost versus speed appears in Fig. 3, providing a comparison between Host/AP and PSPE architectures for typical C-band satellite SAR processors. The base cost of the Host/AP curve is lower than that of the PSPE curve, due to the different stages of evolution in system engineering as well as the type of system development. The Host/AP curve rises sharply at 1/200 of real-time by virtue of increased hardware costs in multiple moderate or high speed AP systems. The PSPE architecture costs curve does not climb steeply as it approaches real-time. The distributed control and data path processor incorporating PSPEs is designed to allow increased throughput at low incremental unit cost, as described in the body of the paper.

The Host/AP approach to SAR processors is more cost effective than the PSPE approach at speeds slower than 1/500 of real-time or roughly one 100 km x 100 km image in one and one-half hours. Some uncertainty in cost estimates is shown by the double lines of each architecture curve. These lead to a shaded transition region between 1/250 and 1/50 of real-time where the PSPE approach becomes more cost effective than the Host/AP approach. Because of a trend from experimental SARs toward fast delivery or operational systems, it is expected the HTSP speeds faster than 1/50 of real-time will be required. A

SAR processor development program which will not lead to restrictive cost impacts at faster than 1/50 of real-time indicates the selection of the PSPE architecture. This choice is seen as the path of the future for satellite SAR processors.

ACKNOWLEDGMENTS
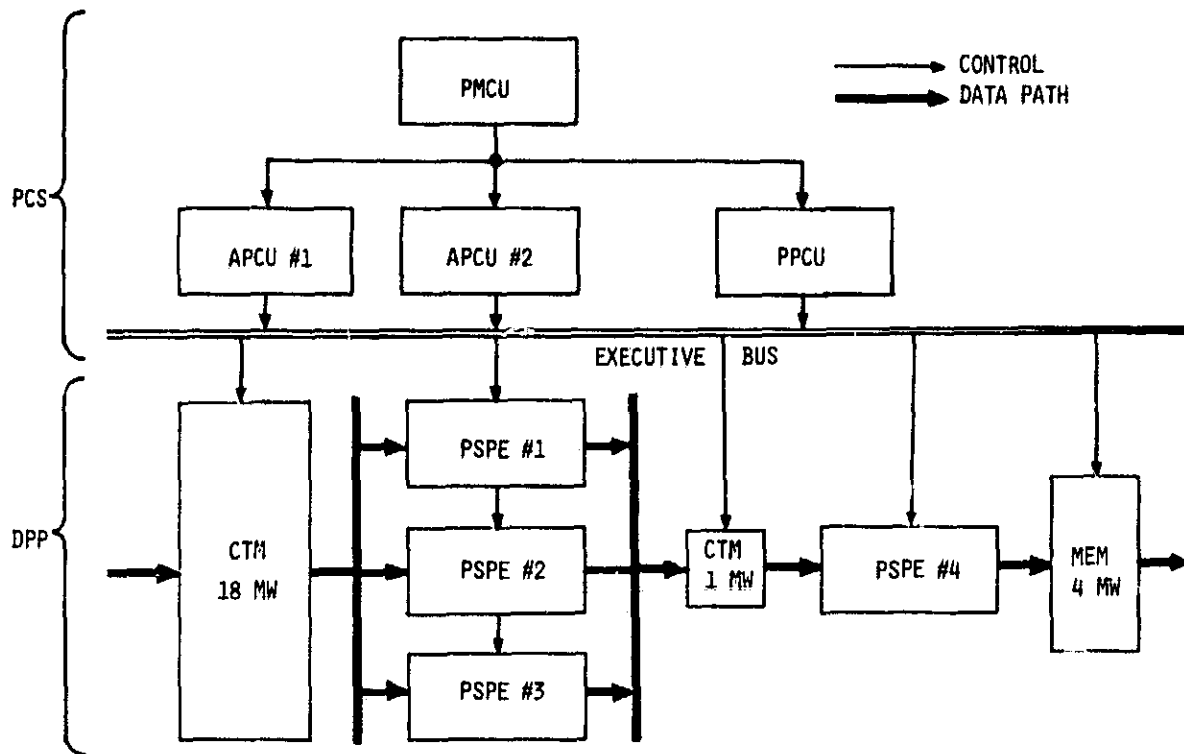
PMCU - Pipeline Master Control Unit*
APCU - Azimuth Process Control Unit*
PPCU - Post Process Control Unit*
CTM   - Corner Turn Memory
MEM   - Deskew Memory
PSPE - Programmable Signal Processing Element
PCS   - Processor Control System
DPP   - Data Path Processor
MW   - Megawords (I & Q)

* Each control unit is one microprocessor.

Fig. 1. MDA PSPE configuration for ESA ERS-1
1/8 real-time azimuth compression.
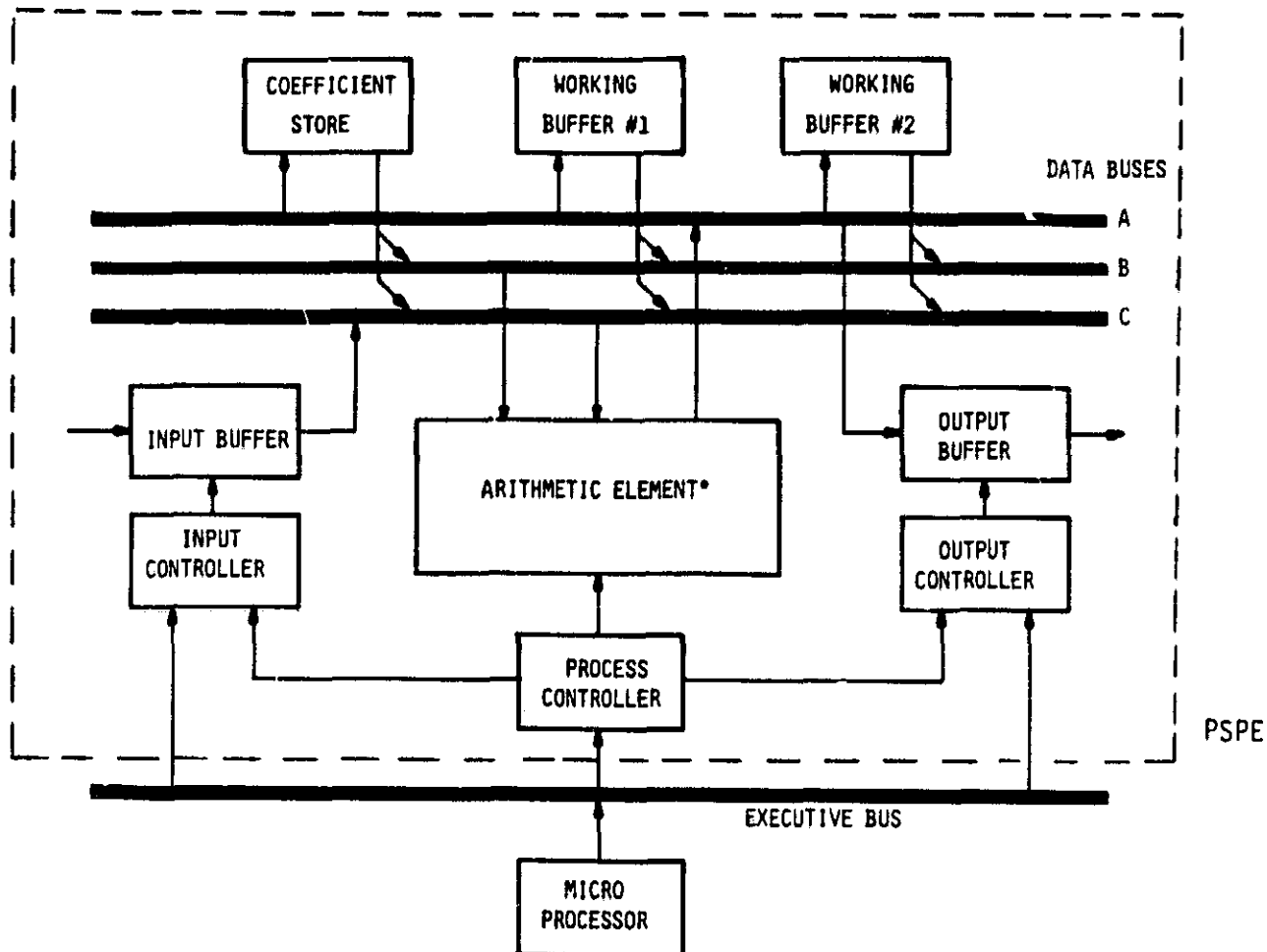
* Arithmetic Element is comprised of:

    DAU - Data Arithmetic Unit
    SAG - Source Address Generator
    DAG - Destination Address Generator
    BC   - Buffer Controller

Fig. 2.   MDA PSPE internal architecture.
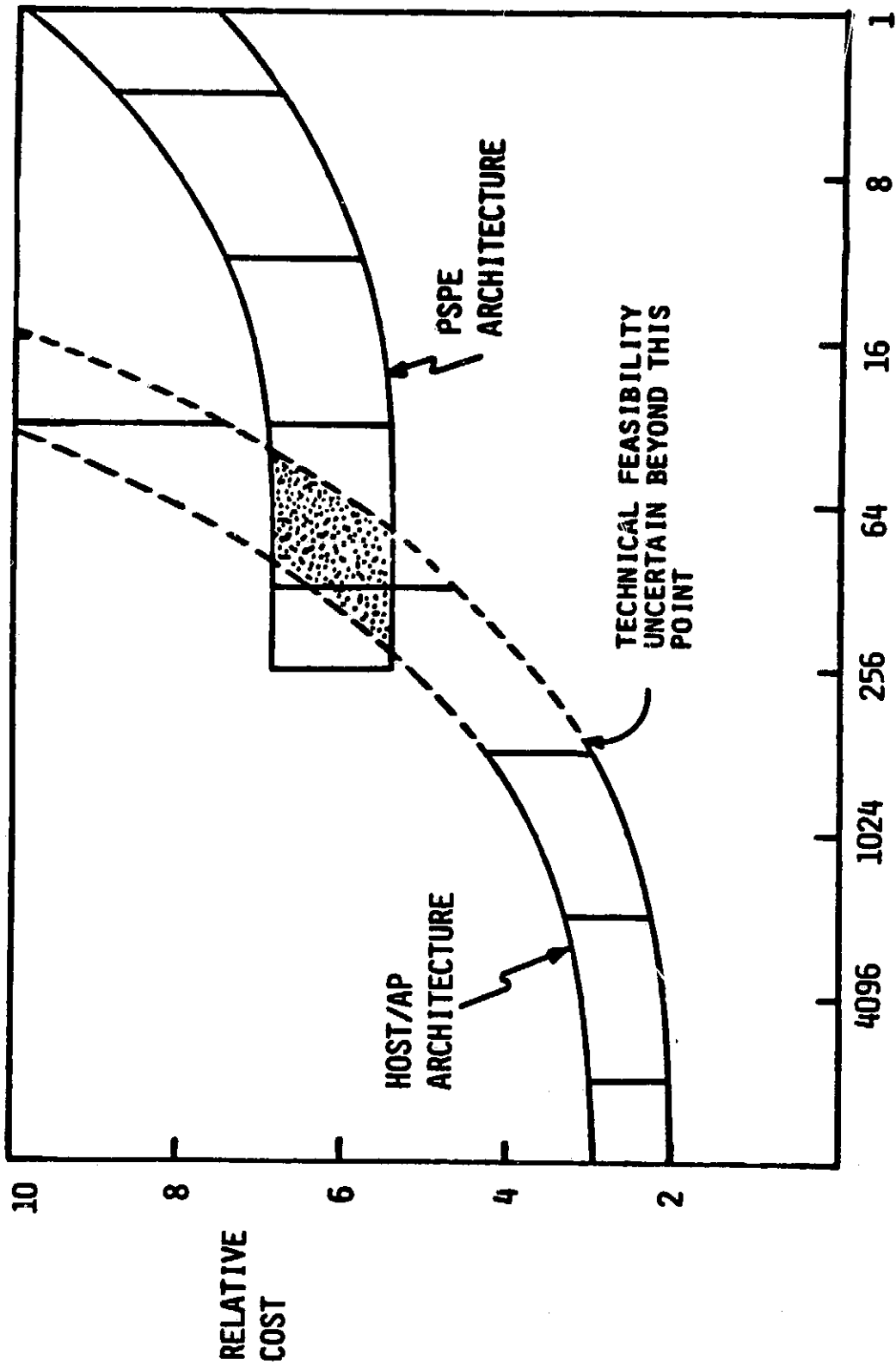
Fig. 3. Cost/speed comparison of two HTSP architectures.

ACOUSTO-OPTIC/CCD REAL-TIME SAR DATA PROCESSOR

Demetri Psaltis
California Institute of Technology
Pasadena, California

Optical methods have been successfully used for over 20 years in SAR image formation. Present optical systems are film based and they are typically large systems that are operated in a laboratory environment. In modern radars it is often necessary to form SAR images in real-time with an on-board processor. This requirement cannot be fulfilled by the film-based optical processors. Even though the advances in digital signal processing technology make it possible in some instances to use digital techniques, in some applications serious problems remain unsolved with this approach - perhaps most importantly, power consumption and cost.

In recent years very significant advances have been made in the state-of-the-art of optical computers. Most of the advances are a direct consequence of the emergence of mature electro-optic device technologies. Laser diodes, acousto-optic devices, semiconductor detectors and electro-optic spatial light modulators that are now available to the designer of an optical signal processing system, coupled with computer-aided lens design and in some instances integrated optics, have led to the development of a new generation of optical computers that operate at high data rates, are compact and power efficient.

The SAR processor that will be presented uses an acousto-optic device as the input electronic-to-optical transducer and a 2-D CCD image sensor, which is operated in the Time-Delay-and-Integrate (TDI) mode. The CCD serves as the optical detector, and it simultaneously operates as an array of optically addressed correlators. A schematic diagram of this processor is shown in Fig. 1. The radar signal is applied to the acousto-optic device in plane P_1 of the figure. The SAR image is compressed in the range dimension by the focusing action of lenses L_3 and L_5. The image is focused in the cross-range (azimuth) direction by integrating on the CCD many range-compressed radar returns each appropriately weighed by a mask placed before the CCD and delayed by transferring the photogenerated charges on the detector. The lines of the focused SAR image form continuously (at the radar PRF) at the final row of the CCD. The principles of operation of this processor, its performance characteristics, the state-of-the-art of the devices used and experimental results will be presented. The methods by which this processor can be made flexible so that it can be dynamically adapted to changing SAR geometries will also be discussed.
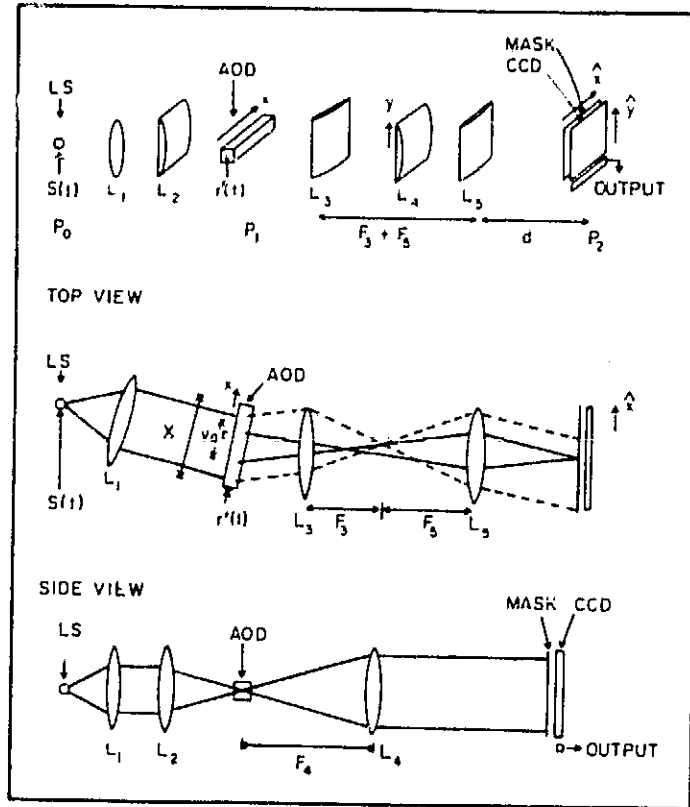
Fig. 1. Processor schematic diagram.

REAL-TIME SYNTHETIC APERTURE RADAR IMAGE FORMATION UTILIZING AN ELECTROOPTIC SPATIAL LIGHT MODULATOR

I. Abramov, Y. Owechko, and A. R. Tanguay, Jr.
University of Southern California
Los Angeles, California

T. J. Bicknell
Jet Propulsion Laboratory
California Institute of Technology
Pasadena, California

In the process of synthetic aperture radar data acquisition, each point target in the terrain to be imaged is illuminated by numerous consecutive radar pulses during an azimuthal terrain traverse by the radar platform (typically aircraft or space vehicles). Thus a given point target contributes a return signal that mimics the radar pulse shape, at a time that depends on the point target range at each radar platform azimuth, and at a center frequency Doppler-shifted by the instantaneous relative velocity of the platform with respect to the target. Recovery of the point target location and scattering strength from such a two-dimensional (range and azimuth) signal record is exceedingly complex, since the return signal amplitude at any given time is comprised of scattered components from all points in the illuminated terrain.

The image formation algorithm from synthetic aperture radar data involves the two-dimensional deconvolution of the recorded phase and amplitude history of the radar return from the radar pulse shape in the range dimension, and from the Doppler-induced phase modulation in the azimuth dimension. For ease in digital processing using fundamentally sequential architecture machines, the two-dimensional deconvolution is typically replaced by two one-dimensional deconvolutions in the azimuth and range dimensions. The reference function utilized in the azimuth deconvolution is a function of range, and hence is inherently space-variant. Since the reference functions employed typically require of order 1000 sampled elements to maintain high resolution in the reconstructed image, such computations are quite cumbersome and often prohibitive.

Optical reconstruction of synthetic aperture radar images can be readily accomplished by recording the return signal phase history on an image storage device such as photographic film. The two-dimensional amplitude that results from a given point target forms a zone plate that is self-focusing in both dimensions when coherently illuminated. Since the azimuth and range focal lengths are functions of distinct parameters, they must in general be brought into coincident focus by cylindrical lenses oriented to act separately on the range and azimuth dimensions.

A number of advantages accrue to such optical SAR processors due to the inherent parallelism of the optical processing algorithm. The inherent speed advantage allows real-time systems to be envisioned that are small, lightweight, and low power. Although digital processors are usually characterized by superior computational accuracy, they are typically quite large, expensive, and power consumptive. Many radar applications such as quick-look

or search modes require or would be better served by on-board processing. These SAR systems will require small, lightweight processors, especially for use in conjunction with spacecraft-borne radars.

Present implementations of coherent optical SAR processors share a common limitation, in that real-time operation is obviated by the use of photographic film as an incoherent-to-coherent image transducer. One possible approach to high-speed optical synthetic aperture radar signal reconstruction involves the utilization of two-dimensional real-time spatial light modulators as recyclable replacements for photographic film in the input transducer plane of modified SAR coherent optical processors, as shown in Fig. 1. Leading candidate spatial light modulators include the Pockels Readout Optical Modulator (PROM), CCD-addressed liquid crystal light valves, and CCD-addressed membrane light modulators. The fundamental physical limitations of such real-time devices that affect SAR processor performance characteristics are under investigation. Current research on the PROM is focused on the effects of device operational mode, device constitutive parameters, electrooptic crystal orientation, writing wavelength, frame rate/data overwrite/presumming, erasure completeness and image retention on the overall quality of SAR image formation.

Several modes of addressing such two-dimensional spatial light modulators are under active consideration, including a z-axis modulated x-y laser scanner, an image-intensified CRT display, and an acousto-optic delay line. A promising new device, the Xerox Linear Array Total Internal Reflection spatial light modulator, is under development and evaluation for the page composition function.

The recent development of such novel electro-optic spatial light modulators (both one- and two-dimensional) will allow real-time coherent optical SAR processors to be implemented. It is hoped that the availability of such processsors will initiate new mission applications not presently envisioned due to current digital processor limitations.

SAR IMAGE
RECONSTRUCTION
PLANE

INFINITE
CONJUGATE
IMAGING
LENS

RANGE
COLLIMATOR

TILTED
AZIMUTH
COLLIMATOR

SPATIAL LIGHT
MODULATOR

SLM
DRIVE
ELECTRONICS

FRAMING
BEAM
DEFLECTOR

SCAN
CONTROLLER

MODULATOR

L
A
S
E
R

SAR
SIGNAL
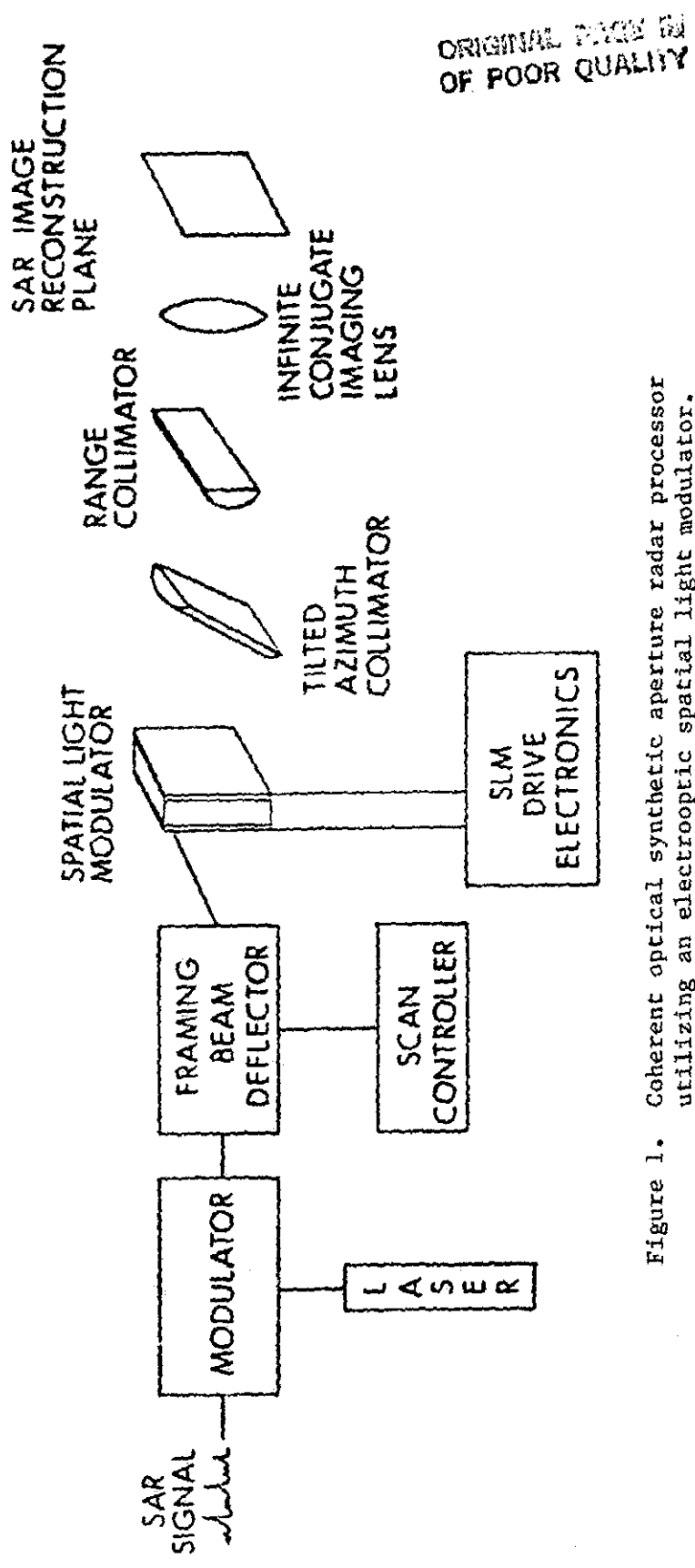
Figure 1. Coherent optical synthetic aperture radar processor
utilizing an electrooptic spatial light modulator.

Ocean and Ice Research

SPACEBORNE SAR AND SEA ICE: A STATUS REPORT

W. F. Weeks
Cold Regions Research and Engineering Laboratory
Hanover, New Hampshire

Of the varied remote sensing systems that have been deployed in satellites to view the earth, none have been designed with the study of the cryosphere in mind. Nevertheless a number of these systems have been very successful in gathering data on the behavior of the world's snow and ice covers. When we consider sea ice which covers over 10% of the world ocean, systems that have proven capabilities to collect useful data include those operating in the visible, near-infrared, infrared, and microwave frequency ranges. Of these, it is the microwave systems that have the essential advantage of being able to observe the ice under all weather and lighting conditions. Without this capability data is lost during the long polar night as well as during times of storm passage - periods when ice activity can be intense. In addition, the margins of the ice pack, a region of particular interest, is shrouded in cloud between 80 and 90% of the time.

What information would scientists and engineers like to obtain about the world's ice packs? A rough list is as follows:

(a)   Ice concentrations - the relative amounts of ice and open water.

(b)   Ice types - the relative amounts of first-year and multiyear ice plus identification of ice islands and icebergs as a starter.

(c)   Ice velocity field - the motions within the ice pack.

(d)   Ice roughness - the amount (areal) of deformed ice and the heights of the roughness elements.

(e)   Ice thickness distribution - the areal percentages of ice of different thicknesses.

(f)   Ice pack geometry - the patterns of open leads, polynyas, floes and pressure ridges.

(g)   Snow and ice surface temperatures.

(h)   Snow cover.

(i)   Surface wind vector field.

(j)   Ocean velocity profile.

(k)   Sea surface temperature.

No one sensor is capable of measuring all of these parameters. In fact it is doubtful if some of this information will ever be obtainable directly from space (items e and j). Nevertheless, microwave systems are capable of major contributions. For instance passive microwave systems can obtain valuable data on (a) and (b). The problem of passive microwave sensors is that the resolution element is large (commonly tens of kilometers) relative to the sizes of floes and leads in the ice pack. Therefore such sensors give averaged values and poor feature definition (this is, of course, an advantage for some applications such as climatic studies). Active microwave systems, on the other hand, are capable of resolutions of a few meters, allowing the detailed examination of the ice cover. It is the opportunity to examine the behavior of the ice in detail that is generally believed to be necessary if we are to advance our current understanding of processes occurring within the ice pack, validate and improve current models for ice forecasting, and obtain data applicable to a variety of operational problems caused by the presence of sea ice. Of the different active microwave systems, it is spaceborne synthetic aperture radar (SAR) that clearly is believed to have the most potential in this regard. Considering that the only spaceborne SAR data was obtained during the brief Seasat mission, that there were no ground-truth observations for this data set, and that as yet there has not been a major geophysical study of this information, this paper reviews why the sea ice community feels that SAR has such great potential for ice studies. This is done by taking an overview of studies completed to date.

These studies, most of which can be categorized as "how to" or "look at that" investigations, show that SAR can definitely provide highly useful information on items a, b, c, d, and f. The exact nature of this information is discussed briefly. It is concluded that although there are still many features on a SAR image of sea ice that are not, as yet, definitely understood or identified, it should not be difficult to resolve most such questions with a straightforward ground-truth program using both surface parties and aircraft underflights. Examples are given of several such "ambiguous" features coupled with possible interpretations.

A practical program for SAR studies of sea ice during the next 10 years would include the following elements:

1.   Studies related to developing improved theoretical models of the electromagnetic characteristics of sea ice. Current models are poorly related to what is known about the internal structure of ice. Advances in this area will undoubtedly require laboratory experimentation on artificially grown ice as well as careful combined radiometric and petrographic field observations.

2.   An experiment using a multifrequency, variable look angle and polarization SAR system deployed in a polar orbit on a Shuttle mission. This experiment coupled with an underflight and surface observation program would improve image interpretation and allow the selection of the optimum system parameters for a SAR designed to study sea ice.

3.   The incorporation of automated image analysis techniques into the processing of SAR imagery of sea ice. The amount of imagery produced by a SAR system is very large and unless there are equally high-speed processing and analysis techniques, the system will rapidly become overloaded and only be useful in a retrospective mode.

4.   The development of the capability to process SAR data in near-
real-time and to effectively transmit the resulting imagery to remote loca-
tions. These capabilities are essential to the needs of many users who plan
to use SAR images to make decisions affecting operations such as shipping.

5.   Deploy a SAR system optimized for the study of ice in a polar
orbiting satellite. This is clearly the most important element in the program
for without the collection of SAR imagery of sea ice, the other portions of
the program become academic. An ideal program for such a launch is that
developed for the proposed joint Canadian/U.S. Radarsat/FIREX mission. In
addition to this proposed program, arrangements should be made to receive SAR
data from the European Space Agency's ERS-1 satellite and from the proposed
Japanese launch of a SAR system. On any of these missions, if coverage is to
be obtained of sea ice areas around Alaska which are of particular importance
to U.S. interests, it will be necessary to establish a SAR receiving station
in Alaska. Even if NASA is not able to participate in the Radarsat/FIREX pro-
gram the establishment of such a station would be valuable in that it would
provide NASA engineers with invaluable experience in resolving the data hand-
ling problems associated with SAR, provide NASA Headquarters with a broad base
of experience that would assist in evaluating the desirability of future
participation in proposed SAR programs and also further sea ice research.
Assuming that the Alaskan SAR station is successful and that suitable SAR
systems are deployed in orbit, NASA should then explore cooperative inter-
national agreements that would lead to the establishment of one or more SAR
receiving stations in the Antarctic. Such receiving stations would provide a
new world of data on the behavior of the ice in the Southern Ocean as well as
of the Antarctic ice sheets and ice shelves.

RADAR IMAGE INTERPRETATION TECHNIQUES
APPLIED TO SEA ICE GEOPHYSICAL PROBLEMS

F. D. Carsey
Jet Propulsion Laboratory, California Institute of Technology
Pasadena, California

The geophysical science problems in the sea-ice area at present concern understanding the ice budget - where ice is formed, how thick it grows and where it melts - and the processes which control the interaction of air-sea and ice at the ice margins. These science problems relate to rather basic questions of sea ice: how much is there; how thick; what is its drift rate; what is its production rate; what determines the morphology of the ice margin; how do storms feel the ice; how do storms at the margin alter the pack; how does the ocean respond to a storm at the margin? Some of these questions are purely descriptive while some require complex modeling of interactions between the ice, the ocean, the atmosphere and the radiation fields. All involve careful measurements of the character of the ice pack, and SAR will play a significant role in the measurements.

The utility of SAR image-data to ice lies in the wide range of backscatter values characteristic of the various ice types. Because of this range, good contrast exists between various ice features in a SAR image, and these features can be identified and located and such properties as their individual total area subsequently estimated. There are two results of this wide contrast range: (1) features can be located in earth-based coordinate frames on images acquired at differen' times so that a small-scale velocity field can be determined; and (2) classification schemes can be devised to make accurate determination of areal coverage of ice species of scientific and operational importance. By these measurements, good estimates can be made of some components of the ice information list of the previous presentation - the ice concentration, type, velocity field and geometry; some information of ice roughness, snowcover and thickness can be developed; and a well designed buoy program can complete the requirements through measurements of temperatures and surface atmospheric pressure. Thus, the role of SAR is clearly to provide key sea-ice data.

A critical element in developing sea-ice information is in timely and quantitative interpretation of images. The tracking of features and the estimation of areal coverages by hand is a forbiddingly labor-intensive process. On the other hand, fully computerized processing - called unsupervised analysis - is at present technologically out of reach because it is still not possible to implement pattern recognition programs sufficient to reliably locate specific ice floes on different images. What is possible is supervised analysis, a computer guided by an investigator in the processing of image data. Two methods of supervised analysis are in development and use at this time: one for tracking features and one for classifying portions of images.

The routine for tracking features is simple in principle. On a split CRT screen, parts of two SAR images are presented containing some common features; the investigator locates a cursor on a pixel (most nearly) common to a feature on each image in turn; and the computer stores the coordinates of

the pixels in an image coordinate system which is later transformed into earth coordinates. At that point, the latitude and longitude of a given feature, such as a pressure ridge, are known for two different times and a Lagrangian velocity field can be produced on a scale as fine as has meaning to the user.

The classification of ice features is more difficult. In fact, no routine exists today which can do a satisfactory job of even a simple or short list of ice types. There are two kinds of routines which provide some success in classification - one which computes attributes such as mean and variance about a given pixel and one which establishes orthonormal sets on which each pixel's local correlation can be expressed as vectors. These schemes suffer from the large scale, in pixels, over which sea-ice texture is defined, and more work over the next 5-10 years is called for. An adequate classification scheme will enable the design of a pattern recognition method for unsupervised tracking and the ultimate automation of extraction of SAR sea-ice data. In order to reach this goal, steady developmental work is required in a number of areas.

D24

# OBSERVATIONS OF INTERNAL WAVES IN THE GULF OF CALIFORNIA BY SEASAT SAR

Lee-Lueng Fu and Benjamin Holt
Jet Propulsion Laboratory, California Institute of Technology
Pasadena, California

Internal waves are among the most commonly observed oceanic phenomena in the Seasat SAR imagery. These waves are associated with the vertical displacements of constant water-density surfaces in the ocean. Their amplitudes are maximum at depths where the water density changes most rapidly — usually at depths from 50 to 100 m, whereas the horizontal currents associated with these waves are maximum at the sea surface where the resulting oscillatory currents modulate the sea-surface roughness and produce the signatures detected by SAR.

Pronounced signatures of internal waves were repeatedly detected in the Gulf of California by the Seasat SAR. There exist over 20 SAR passes in the area, providing by far the most extensive serial imagery of internal waves. This series of images is used to study the time variability of the internal wave activity in the area. It was found that the wave activity was strongly correlated with the tidal cycle (see Figs. 1 and 2), with the maximum occurring during spring tides (strongest tides) and the minimum occurring during neap tides (weakest tides), indicating that the internal waves were forced by tides. Most of the waves were found to the north of $28°$ in the Gulf, where they were primarily generated near the two islands of Angel de la Guarda and Tiburon. Both the bottom topography and the width of the Gulf change rapidly near these two islands, making them the most favorable site for tidal generation of internal waves.

These waves were observed in packets, with their wavelengths decreasing from a few kilometers at the leading edge to a few hundred meters at the trailing edge. Their amplitudes were estimated to be from 10 to 50 meters using a nonlinear dispersion relation.

There are two important aspects of these waves: First, their generation by tides accounts for a certain amount of tidal dissipation, an important concern of tide modelers. Second, the eventual breaking of these waves over shoaling bottom provides vertical mixing which is important for coastal fishery and pollution problems.
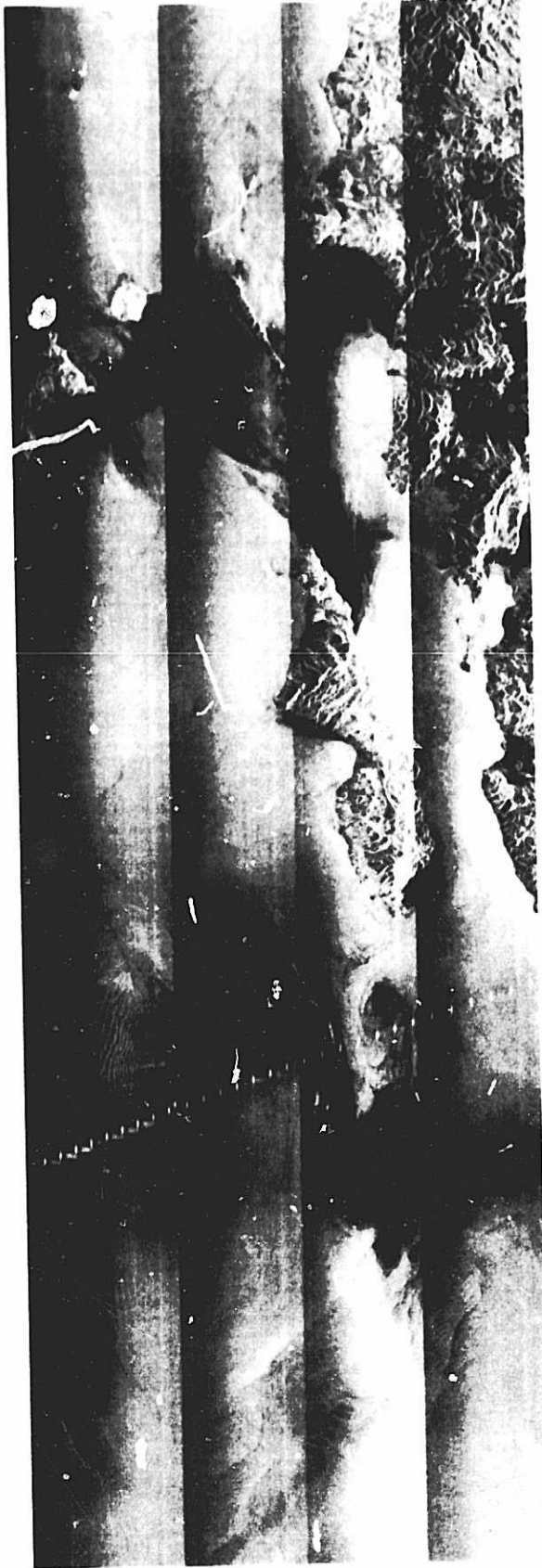
Fig. 1. Image taken September 23, 1978, during a neap tide.
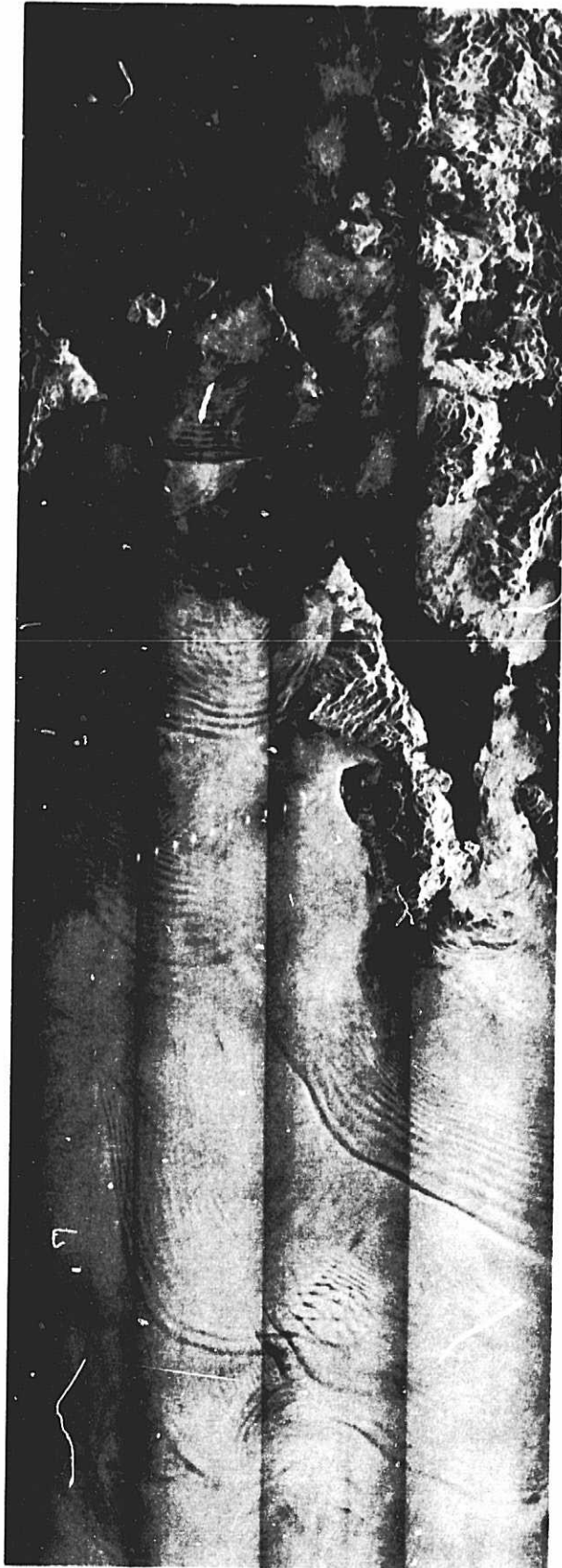
119

Fig. 2. Image taken September 29, 1978, during a spring tide.

120

900 KM OF DIGITAL OCEAN WAVE SPECTRA FROM THE SEASAT SAR

R. C. Beal
Johns Hopkins Applied Physics Laboratory
Laurel, Maryland

I.   INTRODUCTION

One of the primary reasons for including the SAR in the complement of ocean microwave instruments on Seasat was the high priority placed upon global ocean wave spectra. An accurate, timely, and global knowledge of the full two-dimensional or directional surface wave spectra could have great value in both operational wave forecasting and in wave climatology, especially in the Southern Oceans. The sparse sampling obtainable from a single orbiting SAR would by itself be inadequate to reconstruct a global wave field, but when supplemented with auxiliary knowledge of the winds (from, say, a scattero-meter), the SAR might provide essential updates to a global wave model.

II.   ADVANTAGE OF DIGITAL SAR DATA

Prior to the launch of Seasat in 1978, there had been an extensive effort with aircraft to investigate the ability of SAR to obtain useful esti-mates of directional wave spectra. More recently, the aircraft experiments have been supplemented with simultaneous measurements from tower radars, lasers, and in situ measurements. In spite of this intensive attack on the problem, there remains no clear consensus on the part of investigators with respect to the most basic mechanisms of the SAR imaging process.

Early analyses of wave imagery from the Seasat SAR have been sim-ilarly devoid of conclusive statements about the ability of the instrument to usefully estimate directional wave spectra. This surprising state of affairs is due largely to the unknown and variable SAR system transfer function, particularly exacerbated by the lack of calibration, both geometrically and radiometrically, in all of the available optically processed data. Fortun-ately, with the increased availability of well-controlled digitally produced imagery, processor variability need no longer be a problem. The stationary impulse response portion of the total SAR system transfer function can be determined largely by analysis of the actual data (Beal et al., 1983). Even more important, using standard targets or scenes for correction, data from various processors and analyses of many independent investigators can soon be intercompared. This will be an important step, since most Seasat SAR ocean investigators are working with data from diverse geographic regions, and of varying environmental extremes.

III.   ANALYSIS OF PASS 1339 IN THE WESTERN ATLANTIC

Recently we have acquired an extensive set of digitally processed SAR imagery from MacDonald Dettwiler and Associates (MDA) in Vancouver, Canada. The data set spans a 900-km track in the open ocean and coastal areas

just east of Cape Hatteras, North Carolina, from latitude 29.5°N to 37.5°N, and shows a gradually evolving 200-m swell system from a distant storm, and a rapidly evolving 100-m system from a local generating area. Preliminary analysis of the digital SAR spectra along the pass is given in Beal et al. (1983); only the major results will be given here:

(1) The Seasat SAR, when focused for a stationary scene, and when corrected for its stationary impulse response function, shows a definite falloff in azimuth (along track) response, with the falloff becoming more severe in higher sea states. In the data we have analyzed so far, which includes some JASIN data with maximum significant wave height $H_s = 4.4$ m, the minimum detectable azimuth wavelength is given by $\lambda_m \cong (R/V) \, H_s^{1/2}$, where R/V is the range-to-velocity ratio of the platform. For example, with $(R/V) \cong 130$ in Seasat, the minimum detectable azimuth wavelength is $\lambda_{min} \cong 130 (4.4)^{1/2} = 270$ m. This azimuth falloff appears nearly independent of range wave number at all sea states ($1.0 < H_s < 4.4$ m) we have examined, and results in a band of sensitivity along the range dimension whose width varies with sea state.

(2) When the wave system of interest is within the variable band described above, the SAR appears to yield an extremely accurate indication of local wavenumber for local winds 2 m/s $< U_{10} < 12$ m/s, although a spurious rotation of the wave vector toward the range direction can appear at high sea states. In our data set, the rotation was as much as 20°, and was accompanied by significant apparent attenuation of local spectral energy density.

(3) The azimuth falloff appears to behave as a Gaussian type linear multiplication versus azimuth wave number, and therefore may be corrected by multiplying the SAR spectrum by an estimate of its inverse falloff, so long as the signal exceeds the noise. For our spectra, which have been subject to a local smoothing kernel to minimize background noise, correction out to $\lambda \cong (R/V) \, H_s^{1/2}$ appears feasible. The optimum strategy for correction is not clear, however, since the degree of correction depends upon the local sea state, which, of course, is unknown.

IV. IMPLICATIONS FOR FUTURE SAR OCEANOGRAPHIC MISSIONS

The results of our analysis strongly indicate that spaceborne SAR will be severely limited in its ability to track ocean wave systems, especially in higher sea states, unless it is orbited from an altitude significantly lower than that of Seasat (800 km). The SIR-B experiment in 1984 is an ideal opportunity to confirm or reject these implications. If our interpretation of the Seasat results is correct, the SIR-B L-band SAR will have improved azimuth performance of about a factor of 3.5 (800 km/225 km) over that of Seasat at incidence angles around 20°.

REFERENCE

Beal, R. C., D. G. Tilley, and F. M. Monaldo, "Large and Small Scale Spatial Evolution of Digitally Processed Ocean Wave Spectra from the Seasat Synthetic Aperture Radar," _J. Geophys. Res._ 88, 1761 – 1778, 1983.

MECHANISMS FOR SAR IMAGING OF OCEAN SURFACE PHENOMENA: THEORY AND EXPERIMENT

John F. Vesecky
Center for Radar Astronomy, Stanford University
Stanford, California   94305

Observation of ocean surface waves was one of the primary reasons for including the 23-cm-wavelength SAR in the instrument complement of the Seasat satellite. As a natural result, understanding SAR response to surface waves has been a central issue in the analysis of SAR ocean images. Research has included work on both the imaging mechanism for gravity waves and the practical question of just which characteristics of the ocean wave field can be measured remotely using SAR. In the work reported here we base assessments of wave imaging theory primarily on comparisons of the directional wave-height variance spectrum $\Psi(K)$ as measured by <u>in situ</u> buoys with estimates from SAR images. Other criteria can also be used, e.g., the effects of focus adjustments. Most of the SAR and surface data discussed here were collected during the 1978 Seasat-JASIN experiment off the west coast of Scotland (Vesecky et al., 1981, 1982, and 1983). As an <u>initial working hypothesis</u>, we assume that fluctuations in SAR image intensity are proportional to fluctuations in ocean surface height. If this were true, the Fourier power spectrum of a SAR image and corresponding surface measurements of Ψ would coincide. Differences between SAR estimates based on this hypothesis and buoy measurements of Ψ are then used to begin the assessment of rival wave imaging theories.

Although a comprehensive summary of wave imaging theories is beyond the scope of this paper, a few comments are useful. One theoretical view (Alpers et al., 1982) treats the ocean surface as a collection of scattering facets each of which has its own location, orientation, surface roughness, velocity and acceleration. This is sometimes known as the "floating cork" model. An alternative view (Harger, 1981 and 1983) considers a continuous, dynamic surface having a local reflectivity density $g(x,y)$ which varies spatially and temporally in accordance with the gravity wave dispersion relation. In these and other theories the SAR response is governed by three principal factors: the local surface tilt (<u>tilt modulation</u>), local surface roughness (<u>hydrodynamic modulation</u>) and local surface dynamics (velocity and acceleration) which distort the SAR imaging process (<u>surface dynamics distortion</u>). Since each of these factors varies according to location relative to a wavecrest, they can result in ocean waves being imaged by SAR. The details of the imaging process are far from clear and a number of theoretical models exist in addition to the ones mentioned above, e.g., Jain (1981), Ivanov (1982) and Valenzuela (1981). Aside from the Monte Carlo calculations of Alpers (1983) for waves traveling parallel to the satellite ground track, there have been no comprehensive attempts to model the SAR response to a spectrum of waves. In the work reported here we focus on the "ARR" model of Alpers, Ross and Rufenach (1981) and Alpers (1983).

Our approach is to characterize the relationship between the wavenumber variance spectrum of SAR image intensity F_I^2 and Ψ by several linear transfer functions, i.e.;

$$F_I^2 = B^2 H^2 R^2 \Psi$$

REFERENCE

Beal, R. C., D. G. Tilley, and F. M. Monaldo, "Large and Small Scale Spatial Evolution of Digitally Processed Ocean Wave Spectra from the Seasat Synthetic Aperture Radar," *J. Geophys. Res.* 88, 1761 - 1778, 1983.

where B, H, and R correspond to "background fluctuations" related to a given ocean scene, SAR system response and the SAR imaging mechanism (including the tilt, hydrodynamic and surface dynamics factors as well as the radar wave – rough surface interaction) respectively. Using SAR and surface data from the Seasat-JASIN experiment we have calculated $F_I{}^2$ and Ψ. Estimating B^2 and H^2 we find R^2 empirically. The observed characteristics of R^2 can be used to comment on various SAR imaging theories. Although this approach cannot model nonlinear effects, it can indicate their presence.

Perhaps the most difficult part of the SAR imaging problem concerns surface dynamics effects. Theories can be differentiated on the basis of the predictions regarding the effects of changes in focus adjustments during the imaging process. Theories implying an optimum focus related to either the phase (Jain, 1981) or orbital (Alpers et al., 1981) velocities of the observed waves have been proposed. The Seasat SAR images of ocean wave fields during the JASIN experiment showed very little sensitivity to focus adjustment beyond distinguishing between waves approaching or receding from the radar. This is presumably because of the relatively high value of the range-to-platform-velocity ratio (R/V ~ 120).

Besides the transfer function and focus adjustment approaches there are some parametric dependencies which impact the assessment of candidate imaging mechanisms. In particular we note that for the Jasin-Seasat data signal-to-noise ratio (S/N) of $|F_I|^2$ at the dominant wavenumber correlates ($R^2 = 0.53$) with surface measurements of $H_{1/3}$. S/N also correlates with surface wavelength measurements though less well ($R^2 = 0.40$). Estimates of the angular beamwidth of the dominant waves from SAR images agree very well with surface buoy measurements if one "outlier" point is ignored.

For seven cases during the Seasat-JASIN experiment, optically processed SAR images and surface buoy measurements were used to calculate R^2 as mentioned above. In making these calculations the peak of the SAR spectrum was normalized along the spectral density (not wavenumber) axis to the buoy estimate of Ψ. In general, these empirical transfer functions have an "N" shape, having a positive slope (with increasing K) at low K, reaching a peak at K ~ 0.02 to 0.4 m^{-1}, then declining to a relative minimum at K ~ 0.03 to 0.05 m^{-1} and then having a positive slope for larger K. Over the wavenumber range corresponding to wavelengths of 50 to 600 m R^2 lies in the interval 0.2 to 8. These transfer functions reveal that SAR estimates based on the aforementioned working hypothesis are generally biased toward lower K (longer wavelengths). According to the ARR theory this bias should occur and should be stronger as the nonlinearity parameter $c = 1600 \ \Lambda^{-3/2}$ $H_{1/3}$ cos ϕ grows where Λ_m is the dominant wavelength, and ϕ is the angle between the spacecraft ground track direction and the ocean wave direction. While a distinct trend of bias with c is not observed, only large biases occur at larger values of c. This theory also predicts a bias of SAR estimates of dominant wave direction toward the cross-track (range) direction, with the bias increasing with increasing c. Again no distinct trend is evident, but only large biases occur at large c. For K above the dominant wavenumber, the slope of R^2 varies on the average as $R^2 \sim K^{1.2}$. This variation corresponds more closely to the implications of tower experiments (Plant, 1977) than to the theoretical expectations of ARR, namely $|R|^2 \sim K^2$ or K^3.

An interesting implication of the ARR theory is that, as c increases, SAR image resolution along the azimuth direction should be reduced due to surface motion effects. This implies that azimuth traveling waves will be more difficult to image. A plot of SAR signal to noise at the dominant wavenumber (S/N) for the JASIN data set reveals a clear trend toward lower values of S/N as $\bar{c}$ increases. Using the ARR expression for degraded SAR resolution and applying the Nyquist sampling criterion along the azimuth direction we find that waves are very seldom imaged if the Nyquist criterion (two or more SAR resolution cells per wavelength along the azimuth direction) is not fulfilled.

Clearly, study of this problem is far from complete and we have considered only one theory in any detail. Nevertheless, we conclude at this point that the theory of Alpers, Ross and Rufenach (1981) and Alpers (1983) is qualitatively, though not quantitatively supported by the JASIN data set. Further work concerning other theories and digitally imaged data from the JASIN and GOASEX (Gulf of Alaska Experiment) data sets is underway.

REFERENCES

Vesecky, J. F., H. M. Assal and R. H. Stewart, Remote sensing of the ocean wave height spectrum using synthetic-aperture-radar images, in Oceanography from Space (J. F. R. Gower, ed.) Plenum Press, N. Y., 449-568 (1981).

Vesecky, J. F., H. M. Assal, R. H. Stewart, R. A. Shuchman, E. S. Kasischke and J. D. Lyden, Seasat-SAR observations of surface waves, large-scale surface features and ships during the JASIN experiment, in 1982 International Geoscience and Remote Sensing Symposium (IGARSS '82) Digest (J. Nithack, ed.), IEEE, N. Y., WP-3, 1.1-1.5 (1982.)

Vesecky, J. F., R. H. Stewart, R. A. Shuchman, H. M. Assal, E. R. Kasischke and J. D. Lyden, On the ability of synthetic aperture radar to measure ocean waves, Proceedings of the IUCRM Symposium of Wave Dynamics and Radio Probing of the Ocean Surface, (O. M. Phillips, ed.) Plenum Press, N. Y. (1983).

Alpers, W. R., Monte Carlo simulations for studying the relationship between ocean wave and synthetic aperture radar image spectra, J. Geophys. Res., in press (1983).

Alpers, W. R., D. B. Ross and C. L. Rufenach, On the detectability of ocean surface waves by real and synthetic aperture radar, J. Geophys. Res., 86, 6481-6498 (1981).

Harger, R. O., SAR ocean imaging mechanisms, in Spaceborne Synthetic Aperture Radar for Oceanography (R. C. Beal et al., ed.), Johns Hopkins Press, Baltimore, 110-127 (1981).

Harger, R. O., The SAR imaging of short gravity waves on a long gravity wave, Proceedings of the IUCRM Symposium on Wave Dynamics and Radio Probing of the Ocean Surface (O. M. Phillips, ed.) Plenum Press, N. Y. (1983).

Ivanov, A. V., On the synthetic aperture radar imaging of ocean surface waves, IEEE J. Ocean Engr., OE-7, 96-102 (1982).

Jain, A., SAR imaging of ocean waves: Theory, IEEE J. Ocean Engr., OE-6, 130-139 (1981).

Valenzuela, G. R., An asymptotic formulation of SAR images of the dynamical ocean surface, Radio Sci., 15, 105-114 (1980).

Plant, W. J., Studies of backscattered sea return with CW dual-frequency, X-band radar, IEEE Trans. Antennas and Propagat., AP-25, 28-36 (1977).

Future Missions

SPACEBORNE RADAR RESEARCH IN THE '80s

Charles Elachi
Jet Propulsion Laboratory
California Institute of Technology
Pasadena, California

The Seasat SAR (1978) and Shuttle Imaging Radar SIR-A (1981) experiments have successfully demonstrated that spaceborne synthetic aperture radars provide synoptic images of land and ocean features. Radar images clearly show geologic structures, morphologic features, clear cutting, subsurface features (in very arid regions), agricultural and urban land use, ocean surface waves, current boundaries, internal waves, ice floes and numerous other ocean features which affect the surface roughness.

The Seasat SAR and SIR-A provided information about the surface radar signature with very limited observation parameters. Both sensors operated at a single frequency (L-band, 25 cm), single polarization (HH) and fixed incidence angles ($20°$ for Seasat, $50°$ for SIR-A). During the '80s the main thrust in spaceborne radar research is to understand the basic properties of the radar signature of surface features as they related to the radar signal frequency, polarization and illumination geometry. This requires the development of sophisticated flexible sensors. This is the objective of the U.S. Shuttle Imaging Radar (SIR) program, which consists of a series of progressively more sophisticated sensors to be flown on the Shuttle every two years. The SIR-B will be flown in August of 1984. It will be an L-band sensor with controllable illumination angle between $15°$ and $60°$ (Fig. 1). The SIR-C will consist of a dual (L and C) frequency sensor with polarization diversity. It is planned for early 1986. It is also possible to fly the German MRSE (X-band) in conjunction with SIR-B. More sophisticated sensors are planned for later flights.

A number of experiments/missions are planned to address specific geoscientific research topics. A Shuttle polar ice sheet sounder (Fig. 2) can acquire, in one flight, global sounding data over the whole Antarctic Continent and provide an accurate map of the Antarctic bedrock and of the ice sheet volume. A Shuttle scanning radar altimeter (Fig. 3) operating at 36-40 GHz can provide global digital topographic data, with 150-200 m spatial resolution in two Shuttle flights. In the planetary arena, an imaging radar will be put in orbit around Venus in 1988 to map the surface of the cloud- hidden planet to better than 500 meters resolution. A mapping radar is also being considered for imaging the surface of Titan.

In addition to the research oriented missions, a number of radar carrying satellites are planned with quasi-operational activities. The European Space Agency is planning to orbit an imaging radar on the ERS-1 satellite in 1988. The objective is to acquire long-term monitoring capability of ocean features. The Canadian Radarsat (1990) will provide the capability of continuous monitoring of the polar ice cover. In addition, Japan and the U.S. are planning radars on free flyers in the early '90s.

PRECEDING PAGE BLANK NOT FILMED

In summary, the `80s will most likely be the golden age of space-borne radar research where radar remote sensing techniques will catch up with visible and IR imaging techniques, leading to observational capability through the whole electromagnetic spectrum.

|	
ORBITAL ALTITUDE:	225 km
ORBITAL INCLINATION:	57°
FREQUENCY:	1.28 GHz
WAVELENGTH:	23.5 cm
POLARIZATION:	HH
LOOK ANGLES:	15°-60°
SWATH WIDTH:	30-60 km
PEAK POWER:	1 kW
ANTENNA DIMENSIONS:	10.7 x 2.16 m
BANDWIDTH:	12 MHz
NUMBER OF LOOKS:	4
AZIMUTH RESOLUTION:	25 m
RANGE RESOLUTION:	58-17 m
OPTICAL DATA COLLECTION:	8 h
DIGITAL DATA COLLECTION:	≥ 25 h
DIGITAL LINK CAPABILITY:	46 Mbps
COVERAGE (million sq km):	≥ 40
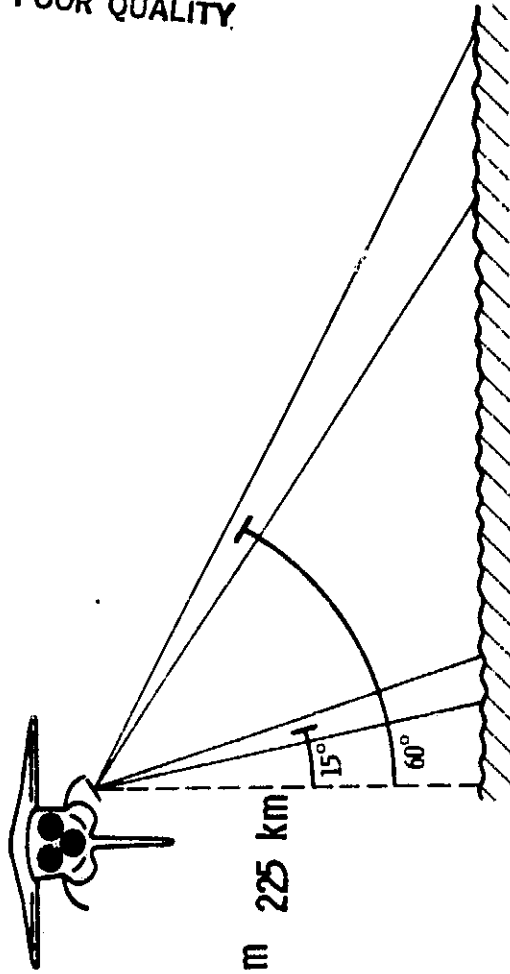
Fig. 1. Shuttle Imaging Radar - B system characteristics and geometry.

133
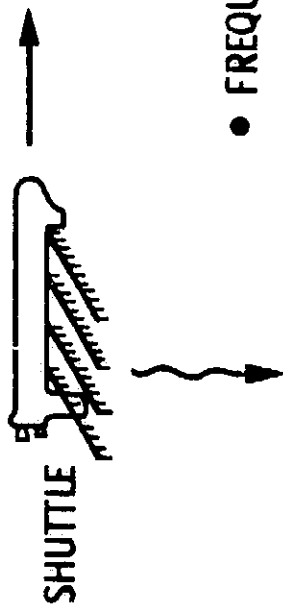
SHUTTLE

- FREQUENCY: 60-200 MHz
- ANTENNA: LARGE ARRAY OF YAGIs
- USE SYNTHETIC APERTURE
- ONE FLIGHT TO MAP THE ANTARCTIC CONTINENT
  - BEDROCK TOPOGRAPHY
  - ICE SHEET VOLUME
  - ICE SHEET INTERNAL STRUCTURE
  - LIMITED BEDROCK IMAGING

Fig. 2. Shuttle polar ice sheet sounder.

- FREQUENCY: 30-36 GHz

- ELECTRONIC SCANNING BEAM

- ANTENNA: 4.6 m - 13.0 m

- DISTRIBUTED SOLID STATE TRANSMITTER

- GLOBAL DIGITAL TOPOGRAPHIC MAP WITH ONE SHUTTLE FLIGHT

  - 5 m HEIGHT ACCURACY

  - 150 m TO 400 m FOOTPRINT

SHUTTLE

SCANNING BEAM

Fig. 3. Global topographic mapping of the earth's surface.

135

RADAR ACTIVITIES OF THE DFVLR INSTITUTE FOR
RADIO FREQUENCY TECHNOLOGY

W. Keydel
D.F.V.L.R., Germany

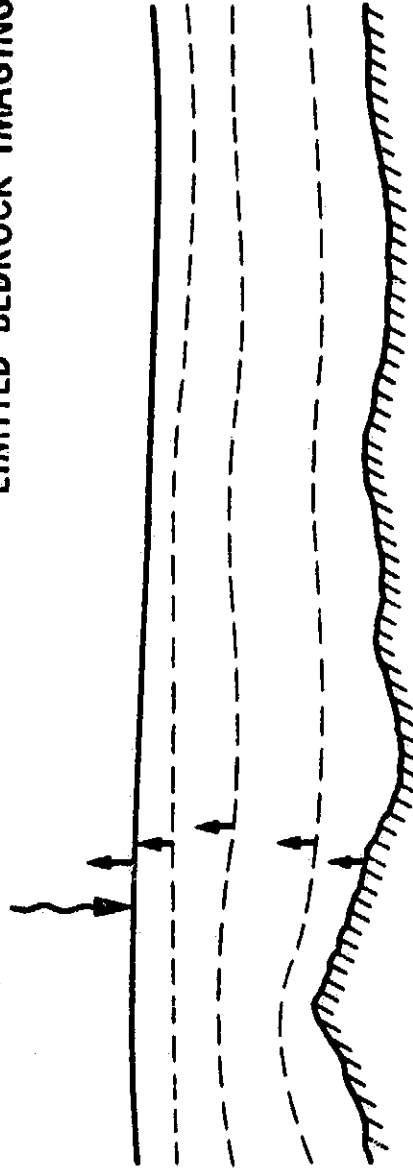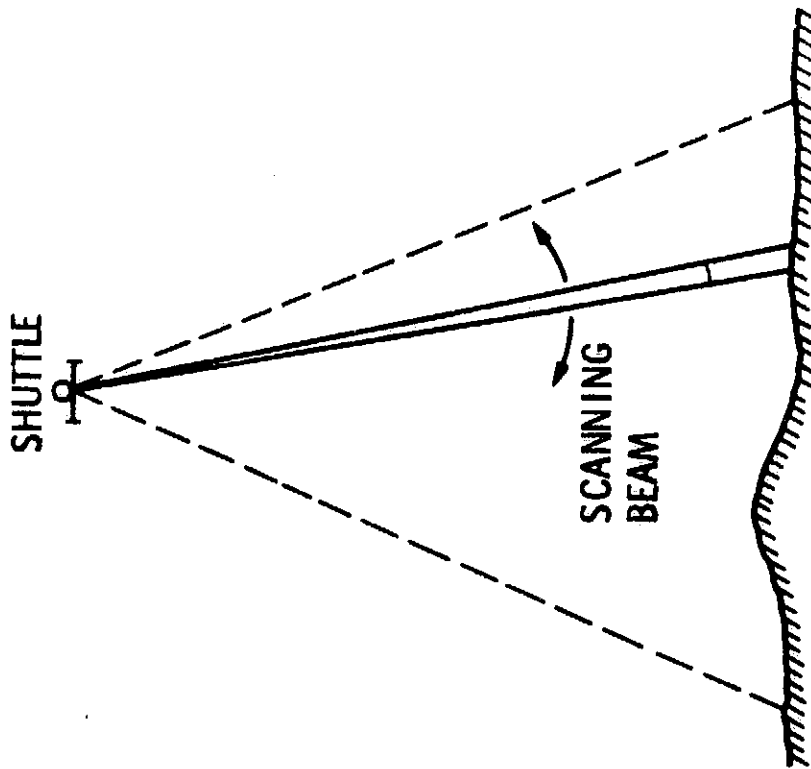The DFVLR, the German Aerospace Research Establishment, is concerned with aerospace research together with the respective applications and agency tasks. Within this frame the research institute for radio frequency technology covers the microwave tasks with respect to remote sensing, position finding and communication. The radar activities are directed at point targets, area targets and volume targets, they center around signature research for earth and ocean remote sensing, target recognition, reconnaissance and camouflage and imaging and area observation radar techniques (SAR and SLAR). The radar activities cover a frequency range from 1 GHz up to 94 GHz. Table 1 shows the radar instruments presently available and planned for 1983. These instruments support the radar program of the institute, which is oriented to four possible application levels: ground, air, shuttle orbits and satellite orbits. Therefore, ground-based studies and measurements will be conducted, airborne scatterometers and imaging radars will be considered, built and operated, a space shuttle radar, the MRSE, has been outlined and will be operated, and follow-on experiments are under consideration. Finally, the institute is strongly involved in German and European satellite activities, i.e., the activities around the planned ERS-1.

The aims of the signature research activities are mainly to understand the interaction between radar waves and the respective targets and to extract the maximum information content for target identification and classification. Within this frame, electromagnetic theory models will be established and simulations will be conducted. A main point in this respect is the dependency of σ and σ_0 on frequency, incidence angle and polarization. The results of airborne measurements will be used for more extended understanding of the ground-based results. Especially for imaging radar applications the complex of phase errors, motion compensation, calibration and SAR-simulation are the main tasks. Experiments will be conducted for the verification of simulation results and for the optimization of SAR parameters. A 2-frequency L-band scatterometer, built in the institute, will be extended to a SAR for small aircraft (SARSCAT). Furthermore, the frequency range of this L-band, SAR-SCAT, will be extended to C-band, the 5.3 GHz of ERS-1. All these activities should be seen in the context of future radar activities with the Space Shuttle (MRSE, ROSE) and satellites (ERS-1) (Table 2). This holds for preparing and conducting pilot projects and data interpretation tasks and for test site, ground truth and experiment preparation as well.

The basis for shuttle experiments is the Microwave Remote Sensing Experiment (MRSE). It is a 3-mode instrument containing a SAR, a two frequency scatterometer and a microwave radiometer. All modes are operating at 9.6 GHz. The first flight is planned for September 1983. Further missions of MRSE, together with SIR-C for instance, are under consideration.

With respect to satellite-borne remote sensing, the ERS-1 is within the focus of interest. The institute gives integrated and functional support to ESA during Phase B and C/D. Focal points of work are: simulations for system and parameter optimization, evaluation and control of calibration concepts, preparation of test sites and pilot projects, and studies on data interpretation.

Table 1. Active microwave instruments for remote sensing.

Instrument	Type	Frequency, GHz	Carrier	State of development
mm radar	Coherent pulse	35	Stationary, airborne	Operational
Rantec radar	Coherent short pulse	8-18 continuously, 94	Stationary	Operational
E-SLAR	Incoherent pulse	10	Airborne	Operational
2-frequency scatterometer	Coherent	1.3	Stationary, Airborne	Operational
C-scatterometer 2 FS-extension	Coherent pulse	5.6	Stationary, airborne	Planned for October 1983
L/C SAR 2 FS-extension	Coherent pulse	1.3 5.6	Airborne	Planned for December 1984
mm radar	Coherent pulse, 2 channel	35	Stationary, airborne	Planned for June 1983
MRSE	SAR SCAT Rad.	9.6	Spaceborne	Ready, launch 1983

Table 2. Radar Programs of Institute for Radio Frequency Technology DFVLR.

	1983	1984	1985	1986	1987
Satellite					ERS-1 (C)
Shuttle	MRSE (X)			MRSE+SIR (L,C,X) 2 polarization X	
Airborne experiments with scatterometer and imaging radar	Accomp. MRSE (L, X) Oil pollution (X), Sea observation (X, C) Modification: L-SCAT → C-SCAT L-SCAT → SAR SAR-data interpretation	Accomp. SIR-B (L, X) Oil pollution (X), Pilot proj. ERS-1 Basic L/C-SAR SAR interpretation	Pilot proj. ERS-1 (3 m res.) L/C SAR Motion comp. SAR interpretation	Pilot proj. ERS-1 Accomp. shuttle L/C SAR Motion comp. 2 polarization SAR interpretation	Accomp. ERS-1 L/C SAR Motion comp. 2 polarization SAR interpretation
Ground-based studies and experiments	MRSE: Ground-truth, experiments, user + application ERS-1: simulation, models, calibration Signature analysis, polarization Target classification	SIR-B: Ground-truth, experiments, user + application ERS-1 simulation, models + experiments Signature analysis, polarization Target classification	ERS-1: Ground-truth experiments, user + application, models Signature analysis, polarization Target classification	ERS-1: Test site Germany, user + experiments, application Target identification + classification	ERS-1: experiments, test site Germany, user, application Target identification + classification

139

EUROPEAN SPACE AGENCY, ERS-1 PROGRAM

A. Haskell
European Space Agency
Toulouse, France

I.   INTRODUCTION

On 24 March 1982 the European Space Agency was authorized by its member states[1] to proceed with the detailed design phase of the first ESA Remote Sensing Satellite, ERS-1. This task is being managed by the Earth Observation department of the Agency's Applications Directorate and is being executed by an industrial consortium led by Dornier Systems of the Federal Republic of Germany. In the present planning the construction phase of the satellite will start at the end of 1983 to provide for launch at the end of 1987.

The objectives selected for ERS-1 are primarily intended to facilitate the exploitation of coastal oceans, including ice-infested waters, and to facilitate the development of improved global weather information through the provision of information on the weather conditions over the oceans of the word. Additionally, land objectives will be addressed using the synthetic aperture radar incorporated in the payload.

II.   THE PAYLOAD

The priority in the payload has been given to a comprehensive set of active microwave instruments able to observe as completely as possible the surface wind and wave structure over the oceans. The set of instruments consists of:

Active Microwave Instrumentation (AMI) operating in the C-band and combining the functions of a Synthetic Aperture Radar (SAR), a wave scatterometer and a wind scatterometer, with the aim of measuring wind fields, the ocean wave image spectrum and of taking all-weather high resolution images of coastal zones, open oceans and ice areas and (on an experimental basis) over land;

Ku-band Radar Altimeter (RA) to measure significant wave-height and wind speed, and to provide measurements over ice and major ocean currents;

Laser Retroreflectors for accurate tracking from the ground.

---

[1] ESA Member States, Belgium, Denmark, Germany, France, Ireland, Italy, Netherlands, Spain, Sweden, Switzerland, United Kingdom, plus Canada and Norway as associated members.

In addition, as a result of an announcement of opportunity, two additional items are being considered for inclusion in the mission.[2] They are:

> Along-Track Scanning Radiometer with a microwave sounder (ATSR-M) to be provided and funded by the UK and France. This is a 3-channel infrared radiometer for accurate sea-surface temperature determination from measurements at two different incidence angles, plus a 2-channel nadir microwave radiometer for the determination of the total vertical column water vapor amount. Two additional experimental channels are also proposed (90 and 150 GHz) in this sounder.

> Precise Range and Range Rate Experiment (PRARE) to be provided and funded by Germany. This is a two-way X-band RF tracking system using pseudo-noise coding techniques. S-band one-way is also included to correct for the ionospheric error.

III. ORBIT

ERS-1 will be launched into a sun-synchronous orbit of 777 km nominal altitude, 98.5° inclination. This will give a three-day repeat cycle. Other repeat cycles (up to 29 days) may be selected as baseline, depending upon the final mission plan. The facility of changing repeat cycle several times during the lifetime will be provided.

IV. MISSION CAPABILITIES

Benefits to be expected from a mission such as ERS-1 result essentially from the possibility of generating short-term and medium-term forecasts of weather and ocean conditions on a local or global basis for the continuous and reliable monitoring of the ocean surface.

The major limitation of current ocean and atmospheric forecasts is the lack of data over the open ocean.

The main inputs required are surface wind field measurements, supplemented by measurements of the surface wave energy spectrum and by direct measurements of wave height. All of these parameters will be observed by ERS-1.

This information can be used in marine industries to improve weather or sea-state dependent operations, to supply better warning of severe wind and wave conditions, to provide a way to improve and manage the resource yield, and to permit a better understanding of the ocean and its dynamics.

---

[2] Final decision to employ these additional packages will be taken at the end of Phase B.

In addition to these ocean-oriented objectives, the observation of sea-ice is an important requirement. The mapping of sea ice boundaries and structure may be addressed, and the altimeter will be equipped with a special ice mode to permit ice topography to be studied.

Although the ERS-1 is primarily ocean/ice oriented, the SAR may also be operated over land, thus introducing a major additional branch of mission capabilities.

V. DATA PROCESSING AND PRODUCTS

To support any mission with a strong element of meteorological forecasting it is necessary to provide a very rapid delivery of products. The target time is 3 hours from reception at the ground station. On the other hand, the scientific users require data of the highest possible quality. These two needs tend to be incompatible.

Within the ERS-1 project emphasis has been placed on providing geophysical products (and SAR imagery) within three hours. This will be achieved using a single ERS-1 project ground station at Kiruna. In addition the raw data will be annotated and passed to Earthnet, the element of ESA responsible for remote sensing data acquisition and processing, where precision products will be generated in non-real-time, either in ESA or in national facilities.

In addition to the Agency's facilities mentioned above, some member states plan to use national facilities to receive and/or process data.

VI. CONCLUSION

After much careful planning, the design phase of ERS-1 is proceeding rapidly. A baseline system concept has been defined and a preliminary design review has successfully taken place.

THE CANADIAN RADARSAT PROGRAM

Keith Raney
Radarsat Project Office
Ottawa, Canada

Canada has allocated nearly $20 million to the definition phase and technology development leading towards an operational imaging radar satellite system, planned to be in orbit in 1990 and beyond. This paper outlines the project and its applications, from Arctic sea resources to agriculture and forestry, with benefits forecast in excess of $200 million per year.

The radar (SAR) is to be C-band, and processed in near-real-time so that prime users can have data, to scale and annotated, within 4 hours of overflight. Electronically steerable elevation patterns are planned for the antenna, to cover a range of incidence angles of $20^{o}-45^{o}$, allowing for more effective swath location, and a wider variety of application benefits. The high power required (500 W rf average) and the large antenna (18 x 2 m) are seen as the major technical challenges.

THE U.S. SPACE STATION: POTENTIAL BASE FOR A SPACEBORNE MICROWAVE FACILITY

D. McConnell
NASA Headquarters
Washington, D.C.

I. INTRODUCTION

NASA has begun to study concepts for a U.S. space station. This is fully in line with two key elements of the recently announced U.S. space policy: to achieve the full potential of the Space Shuttle and to provide a more permanent presence in space. The space station study is summarized in the following questions: Given a space station in orbit in the 1990's, how should it best be used to achieve science and applications objectives important at that time? And, in order to achieve those objectives, of what elements should the station be comprised and how should the elements be configured and equipped.

In order to address these questions as objectively as possible, NASA has implemented the following study approach:

(1) The user (science and applications) community and aerospace industry have both been involved from the outset. Figure 1 shows the study schedule. In parallel with the industrial studies, the National Research Council has also begun studies conducted by the Space Science Board and the Space Applications Board.

(2) An independent Space Station Task Force has been established so that the approach to issues will be neither payload nor system dominated.

(3) NASA has published a Space Science and Applications Notice inviting proposals for innovative utilization of the Space Station. The aims of the Notice are to broaden participation in the studies and to enable the presentation of ideas by people who might not be reached by the traditional processes.

Finally, in this regard, the main point of my talk today is to stimulate your thinking and planning for the space station era. Obviously, NASA would appreciate your advice and suggestions. But, as I will emphasize shortly, this is a particularly important period in the field of imaging microwave systems for earth observations. Research results during the next three to seven years could have an important bearing on the actual conceptualization and design of space station-associated measurement systems.

II. SYSTEM ARCHITECTURE AND THE ROLE OF MAN

Now, what might a space station look like? Figure 2 shows what is emerging as an attractive concept. On the right, there is an array of unmanned space platforms, each individually optimized to conduct specific

missions such as earth observations, astronomy, materials processing, and "other" missions. On the left, there is a space base of operations which is equipped for human habitation and outfitted to enable orbit-to-orbit maneuvers, resupply by the Shuttle, and even some experimentation, checkout of sensors, calibration, and the like. The terminology being adopted is that a space <u>platform</u> is unmanned, whereas a space <u>station</u> implies human habitation. These two basic elements of the system "architecture" are coupled by means of extravehicular crew activities or teleoperator (i.e., robotic) maneuvering systems for automated interaction with the platforms.

This concept embodies several important principles. First, it is widely felt that a prime role for man in space will be in servicing automated sensors. This could involve replacing or repairing defective subsystems, replenishing cryogens or other consummables, assuring the deployment of structures, and so forth. Successful use of this concept could have extended the lives of several spacecraft had the capability been available. Our Skylab experience comes to mind. The first test of repair on a spacecraft subsystem will be on the Solar Maximum Mission in 1984.

Effective use of the maintenance and refurbishment capability will require careful planning from the earliest design stages. For instance, in-space repair of the Solar Maximum Mission (SMM) is feasible because SMM uses the Multimission Modular Spacecraft in which the subsystems (e.g., attitude control, power, communications, etc.) are fairly accessible. Future missions such as the Space Telescope (ST), Gamma Ray Observatory (GRO), and the Advanced X-Ray Astrophysics Facility (AXAF) are being planned to make specific use of revisit capability. Dr. Franklin W. Martin, NASA's Director of Astrophysics, has led a working group on AXAF Utilization of STS and Satellite Servicing. That panel gained input from the scientific community, instrument and system designers, and engineers and mission managers in NASA and industry. Their findings are summarized in Figs. 3 and 4. As one considers highly capable, relatively expensive facilities for earth observations such as a microwave facility, they too should be planned for the longest effective life. Even though servicing is likely to be used first for repair or housekeeping subsystems, in time one might consider replacement of modification of sensor and instrument subsystems. Thus the planning should include the potential research users such as yourselves.

As distinct from the servicing function, the role of man as a direct observer is still being debated. In most cases, sensors acquire large amounts of repetitive data, so automated sensors are preferred. Where episodic events are concerned, an investigator can in principle interact in real-time, even if the investigator is on the ground. In this case, as was successfully shown on the International Ultraviolet Explorer Mission, the investigator has access to computer support, ancillary data, and so forth. Such an approach, however, places a very heavy burden on the data handling and communication systems. So the question of the most effective form of human interaction is still open.

Another idea embedded in this concept is that the array of unmanned platforms will enable optimization to achieve missions free of the encumbrances associated with the continuous presence of a crew. Thus the platforms are free of possible contamination from the exhaust of life support systems or stray accelerations from crew motions. Unmanned platforms offer a potentially wider array of altitudes and inclinations through the use of an Orbital Transfer Vehicle (OTV).

Now, what are the potential advantages for research of a large, man-tended space platform? Why should the science and applications communities be interested as potential users? Figure 5 shows an artist's rendition of the evolution of a space station and growth of capabilities through a series of Shuttle revisit flights. One potential benefit is this: in addition to maintenance and refurbishment of the current generation of spacecraft, revisit capability may enable different ways of doing business in space. Consider power and energy requirements. Certainly, a large platform could enable the deployment and control of large solar cell arrays. However, revisit capability will enable the resupply of consumables such as fuel cell reactants. In the case of hydrogen-oxygen fuel cells, the product water could be processed and used for the crew. This is especially interesting because each Shuttle flight carries some 15,000 pounds of excess liquid hydrogen and liquid oxygen propellants as a safety margin. The excess fuel from the Shuttle could be a "cost-free" source of liquid hydrogen and liquid oxygen - once we learn how to transfer cryogens in space. Revisit capability could also enable the use of more efficiently designed radioisotope thermal generators (RTG's), or even the use of nuclear reactors - but that latter involves substantial policy questions. The point is that new possibilities become available to us.

Figure 6 shows the erection of a large antenna for communications or for microwave observation of the earth. This brings us to the final issue, from the potential user's point of view, why is it desirable to have a large platform in space? One answer is that a large, man-tendable platform would enable capabilities not generally available on individual spacecraft. One would particularly expect higher power levels and the deployment and control of large structures such as microwave antennas. These capabilities should be important in the conduct of future earth sciences programs and were among those considered prime by the OSSA "System Z" study and other groups such as the panels of the Space Applications Board Workshop.

III. MICROWAVE FACILITY FOR EARTH SCIENCES

Figure 7 indicates the general strategic thrust being pursued by Burt Edelson in directing NASA's earth science program. His aim is to use the synoptic view from space to address global issues. The elements of the program are unified in the "Global Habitability" concept, the key objectives of which are to measure global changes and to assess their impact upon biological productivity and human health. The programs under Global Habitability will address such questions as the global biogeochemical cycles which, almost by their nature, require an interdisciplinary approach. For example, the global cycle of water involves measurement of the biosphere and living biota, continental snow cover, precipitation, soil moisture, and so forth.

To get firm information on the elements of the cycle through remote sensing, one would expect to make near simultaneous measurements in a range of spectral regions with a variety of sensors - especially while the techniques were in the development stage. The "System Z" study, considering the next generation earth observing system and not related to the Global Habitability effort, formulated a "red" payload to study global hydrology. Figures 8a and 8b show the JPL concept for the "red" payload and the associated mass and power requirements. Notice the obligatory solar cell array. Notice also the prevalence of microwave sensors. Unfortunately, a lot of technique development remains before we will be able routinely to measure the elements of global hydrology.

The measurement of global scale precipitation is a subset of the global hydrology problem, but it is also information of extreme importance in its own right. Figure 9 shows some of the uses for precipitation data and some of the measurement requirements. Direct precipitation data could: improve crop yield modeling and enable more timely crop production forecasts; improve our understanding of atmospheric energetics as the associated latent heat release is a major source of atmospheric heating; and enable the verification of climate models which predict long term prediction patterns. In their 1977 paper, Atlas, Elachi, and Brown analyzed the use of airborne SAR for mapping and measuring rainfall. Figure 10, taken from their paper, shows something of the capability one might expect from such a system. One can easily conceive of a "multispectral" facility using optical imagers, passive microwave radiometers, and SAR to intercompare rainfall estimates by the several associated techniques in order to reduce the individual uncertainties. Further, each technique has some limitations (e.g., the VIS-IR highly reflective cloud technique of Ramage and colleagues seems to apply only over the tropical oceans, passive microwave generally would not apply over land, SAR is costly in power and data analysis demands), so having all three techniques available would allow more complete coverage. Using the imaging systems, one would, for instance, take SAR data only where it was raining.

So far, this paper has emphasized the use of a microwave facility to address environmental questions because most of the other papers have considered geologic applications; but the benefits of a microwave facility are not so restricted. The Space Applications Board Summer Workshop to study the uses of a space station was divided into a number of panels. As a participant, I found it interesting that the Earth Resources, Oceans, and the Environmental Panels all separately arrived at the need for (that is, the significant benefits to be gained from) a multisensor microwave facility during the 1990's. At the outset, this would be a research and development facility. Thus, as far as active imaging systems are concerned, the facility would require combined multifrequency (say, L, C, and X bands) and dual polarization. There should be the opportunity to operate a number of frequency bands simultaneously and to operate with variable incidence angles and larger swath widths than have been available up to this time.

For environmental observations, it is expected that the facility would also have such additional sensors as a radar altimeter for ocean surface topography, an imaging radiometer for sea surface temperature and ice boundaries, a scatterometer for wind speeds, and so forth. These sensors complement each other especially in the R&D mode. It should be noted that in both

the System Z study and the work of the SAB panels, data handling requirements were found to be the most severe in terms of driving capabilities beyond those which now exist. It has been noted that both flights (Seasat and SIR-A) of imaging radars were severely limited by data transmission capability. Future data handling requirements become even more severe as one contemplates real-time interaction with the sensors. Such interaction is only meaningful if "quick-look" data processing and analysis are available. Figure 11, though taken from the System Z study, indicates how a microwave facility could provide a range of valuable information on ocean conditions.

IV. SUMMARY AND CONCLUSIONS

Let me conclude now with these summarizing observations:

(1) NASA is seeking your knowledgeable advice and suggestions on how an orbiting, revisitable, man-tended space platform could best be used in the 1990's.

(2) I have suggested that a large platform could enable the development and effective use of an orbiting, multisensor microwave facility and that such a facility would be useful both for technique development and for data which would be valuable in addressing a number of issues of importance in the 1990's. Furthermore, in order to make the best use of revisit and servicing capabilities, the using science and applications communities should begin the planning process as soon as possible.

(3) The U.S. plans to fly SAR systems in 1984 and 1987. On these flights, there will be other imaging systems, such as the Large Format Camera, which will fly with SIR-B. In the same general time frame, Japan and Germany are also expected to fly microwave systems. So lot of information will become available from different sensor and data analysis techniques. This will allow for experiments in the coregistration of different data sets and for the selection of the most effective measurement and data analysis techniques.

Given the acknowledged successes of Seasat and SIR-A, both the scientific community and governmental bodies are anxiously awaiting the results of these experiments. They will have both scientific and practical, economic applications. Therefore, the work that you plan now and conduct over the next three to seven years could have a very great impact on the development of the space station and on the conduct of the earth science and applications program. We hope that you will diligently bear this in mind as you move forward in the planning process — both in tomorrow's workshop and in the subsequent programs over the years.
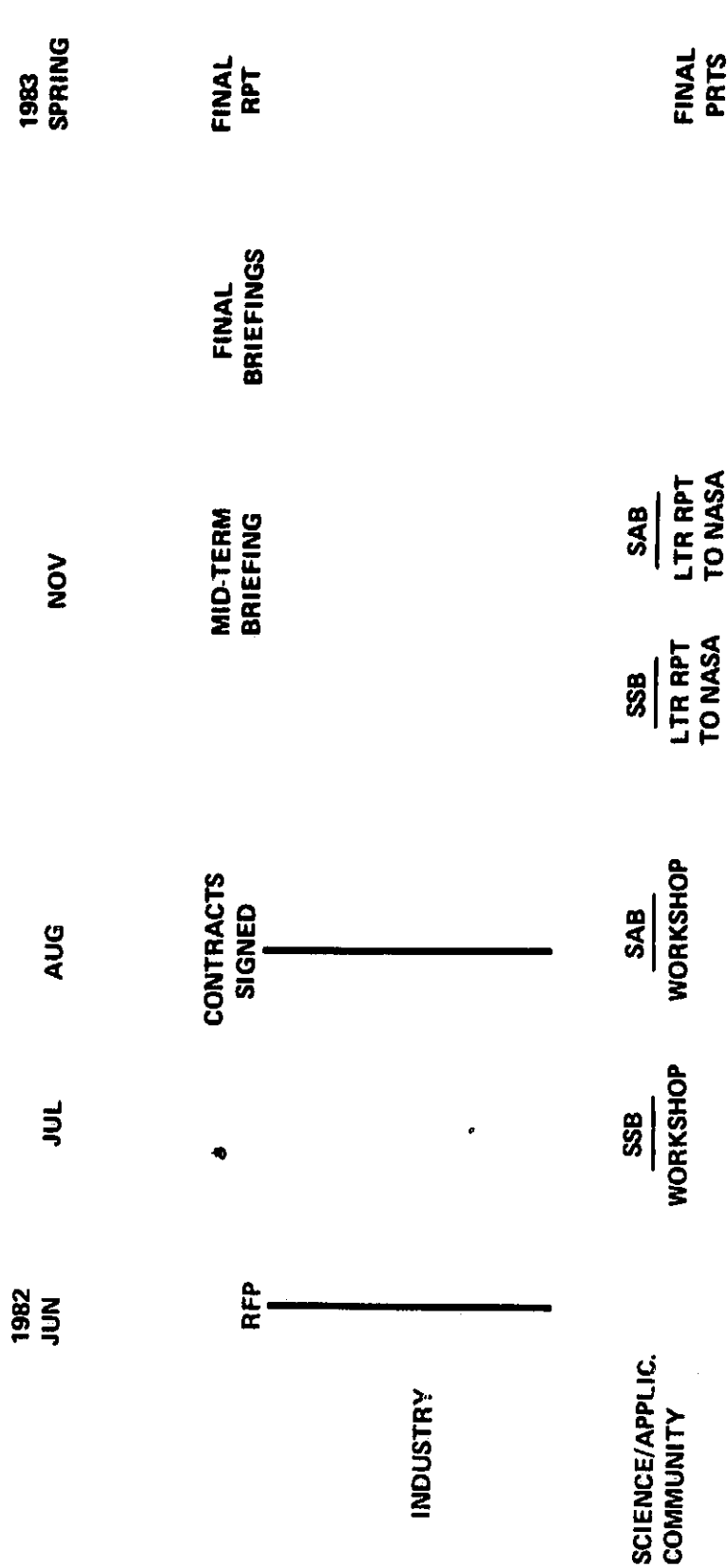
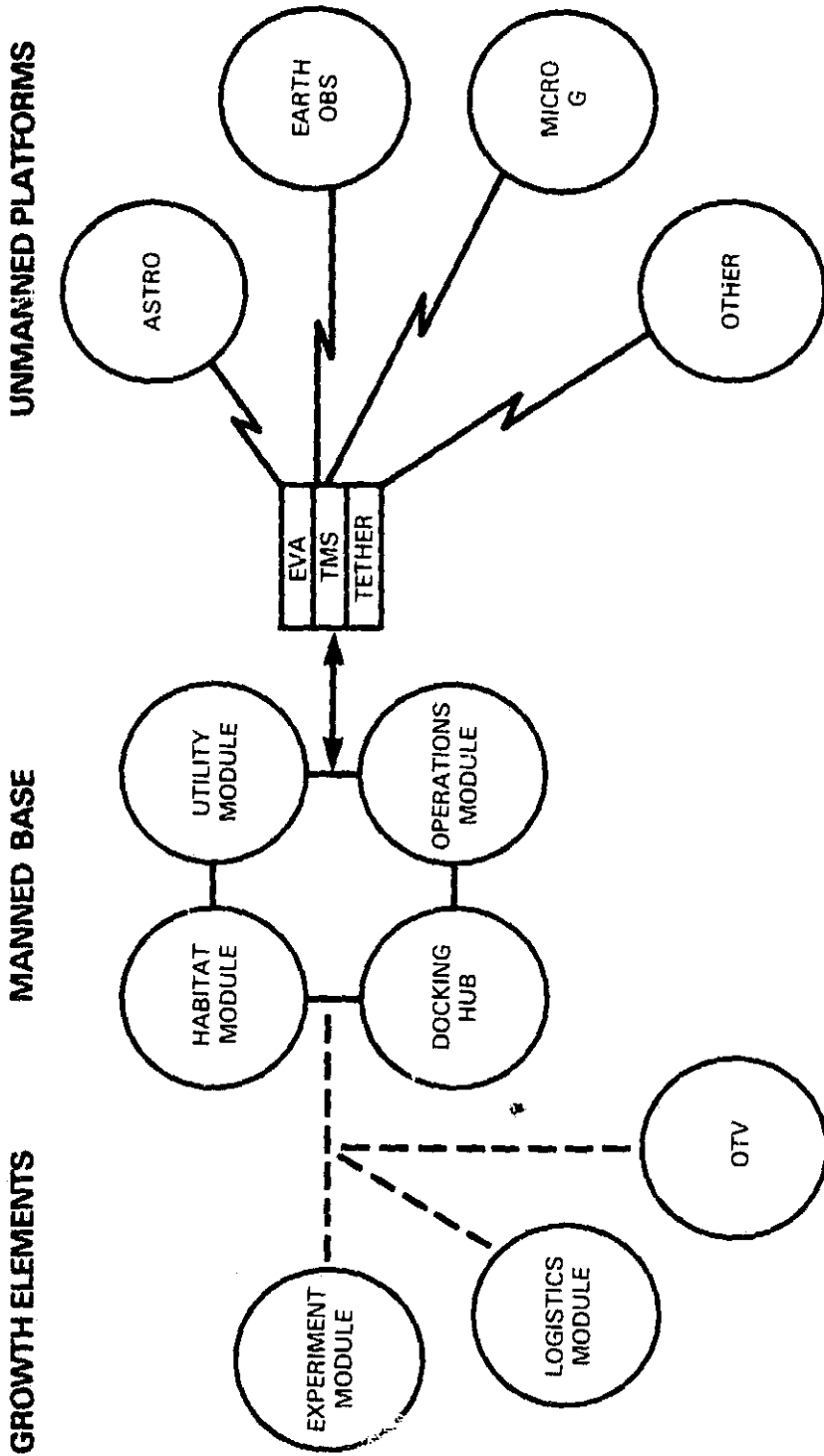Fig. 1. Aerospace Industry National Academy of Sciences.

149

Fig. 2. A space station architecture: cluster concept.

- CONCEPTUAL
  - AXAF BENEFITS FROM SERVICING
  - BALANCE REDUNDANCY, RELIABILITY, OPERATIONS, SPARES AND COSTS OVER LIFE-CYCLE
  - PLANNED GROUND REFURBISHMENT UNDESIRABLE
  - EMPHASIZE EVA OVER ROBOTICS IN NEAR TERM
  - "CLUSTER" SPACECRAFT FOR SERVICING
  - "DON'T FIX IT IF IT AIN'T BROKE"

- HARDWARE
  - INTEGRAL PROPULSION AND/OR TMS NEEDED
  - NEXT GENERATION SPACE SUIT
  - DEVELOP COMMON SUPPORT HARDWARE ACROSS PROJECTS
  - SOME SERVICING HARDWARE AND TMS SHOULD BE BASELINE STS
  - NO APPARENT STANDARDS FOR SERVICING

- OPERATIONS
  - DEVELOP "CALL-UP MISSION" CAPABILITY
  - TRANSPORTATION CAN DOMINATE M&R COSTS
  - CONTINGENCY RETRIEVAL CAN IMPACT MANIFEST OPPORTUNITIES
  - SHARED FLIGHT LAUNCH WINDOW CAN IMPACT SERVICING MISSIONS

Fig. 3.   AXAF panel observations.

- SERVICING CAN PROVIDE PROGRAM FLEXIBILITY AND COST ADVANTAGES

- INITIAL STEPS TO ESTABLISH M&R CAPABILITY ARE UNDERWAY
  - NEED BETTER SUITS TO PERMIT FINGER DEXTERITY

- INCREASE IN STS BASELINE IS NEEDED
  - NEED LAUNCH "CALL-UP" CAPABILITY

- LESSONS LEARNED SHOULD BE FOCUSED FOR FUTURE PROGRAMS

- PROJECTS SHOULD NOT INDEPENDENTLY CONDUCT M&R
  - "NEED FOR MAYTAG REPAIRMEN"

- "MAYTAG" APPROACH SHOULD ALLOW FOR DARWINIAN EVOLUTION NOT STANDARD/LOW COST SYSTEMS APPROACH
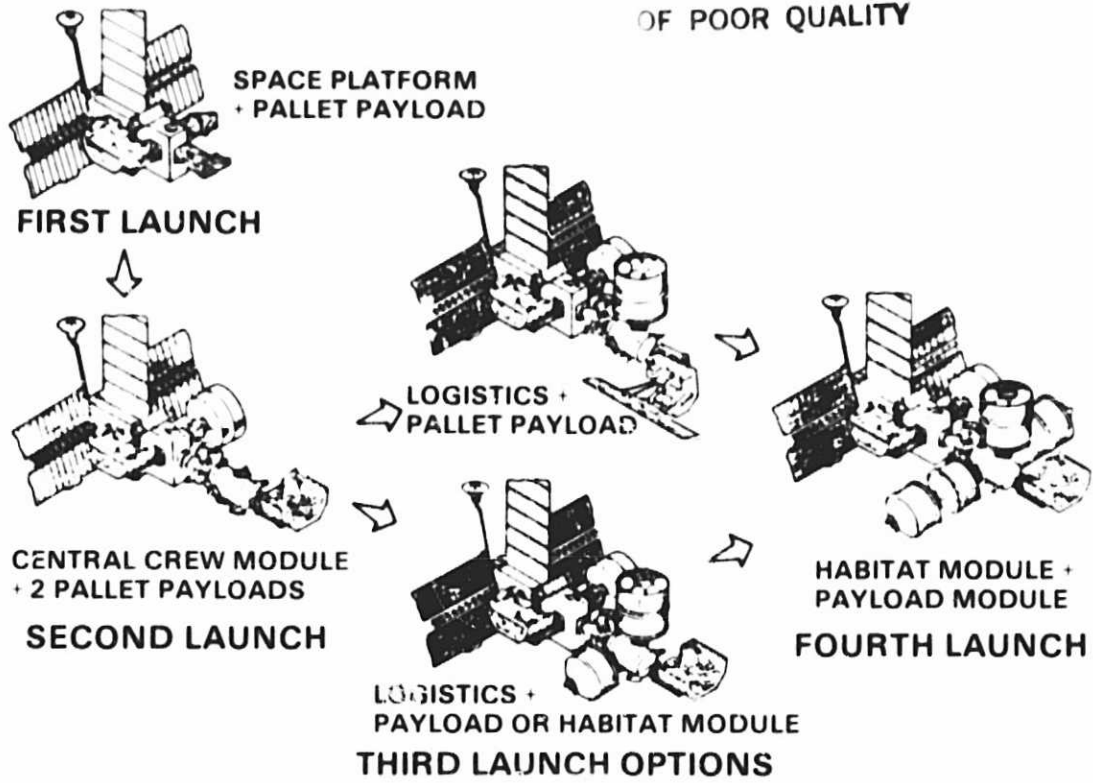
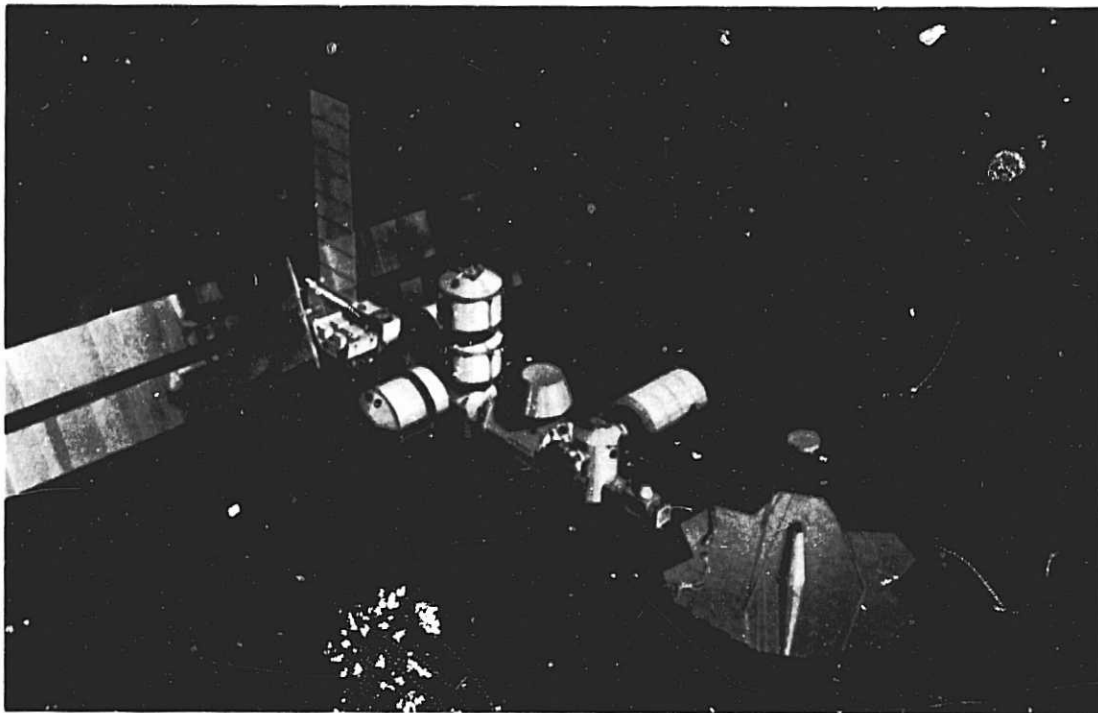Fig. 4.   Observations.

Fig. 5.   Manned platform buildup.

Fig. 6.   Erecting a large antenna in space.

DATA USE OBJECTIVES

- GLOBAL PERSPECTIVE
- EARTH SCIENCES ORIENTATION
- MULDISCIPLINARY EMPHASIS

- SIMULTANEOUS MEASUREMENT WITH MULTIPLE SENSOR
- INTERLEAVE & INTERCOMPARE MULTI-SENSOR DATA STREAMS

FLIGHT PROGRAM BASES

- NASA MISSION IN SPACE R&D
- SENSOR & TECHNIQUE DEVELOPMENT

Fig. 7.   OSSA programmatic outlook.

LAMMR
(10M ANTENNA)

DCLS
(DUAL AXIS)

WFIR

SOLAR ARRAY
(4M x 38M)

IR/MICROWAVE
SOUNDER

PROPULSION

SAR
(2M x 15M)

IMAGING
SPECTROMETER
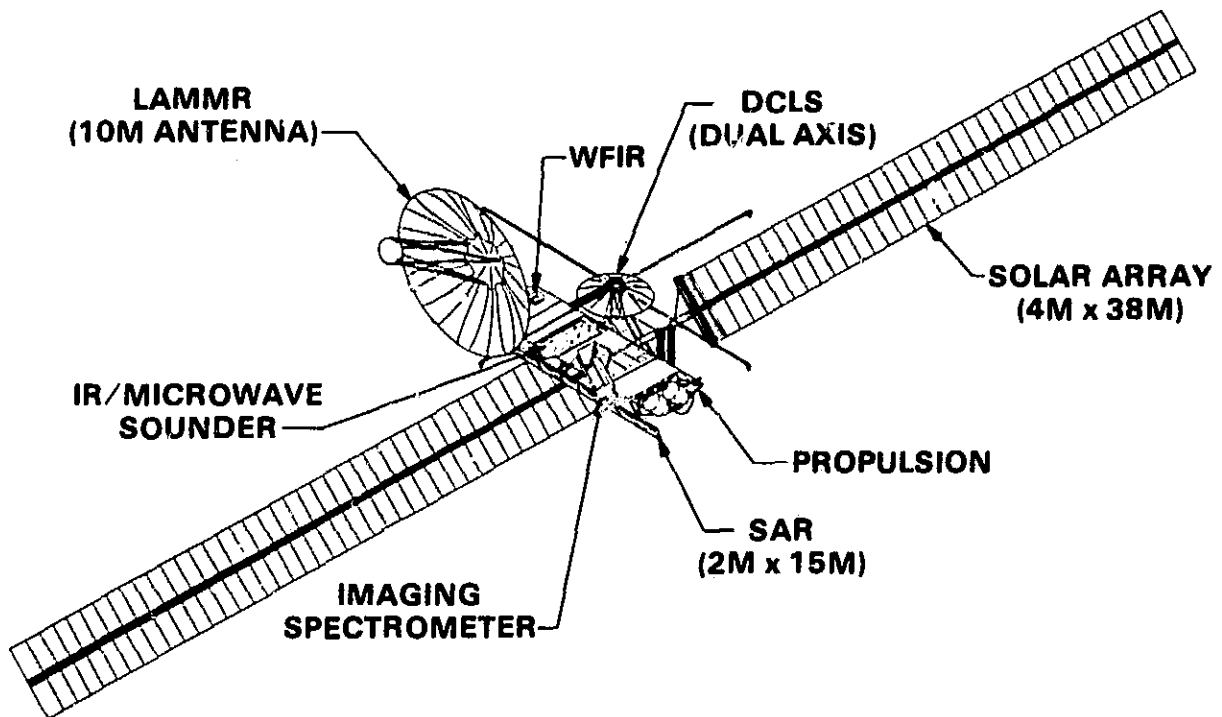
Fig. 8a.   System Z, "red" payload.

153

SUBSYSTEM	MASS (kg)	POWER (kW)
TELECOM	83	0.25
POWER	925	0.31
COMMAND/DATA	150	0.75
DATA STORAGE	142	0.50
AACS	1100	0.92
PROP (DRY)	538	0.31
STRUCTURE, CABLING, THERMAL CONTROL	1580	0.50
PAYLOAD	2330	7.77
SUBTOTAL:	6848	11.51
PROPELLANT	1860	
LAUNCH WT	8708	

*3 LMSC 1.57 m x 0.93 m N_2H_4 TANKS

Fig. 8b. Configuration sizing: "red" payload power and mass estimate.

- AVERAGE OF 6800 kg. LH_2/LO_2 ON EACH FLIGHT

- ASSUME STOICHIOMETRIC PROPORTION 7.934:1, LO_2:LH_2 BY MASS
  HENCE 6038.86 kg. LO_2, 761.14 kg LH_2 OR 377.54 kg-mol LH_2

- FREE ENERGY OF FORMATION OF LOW GRADE STEAM IS 228,000 kJ/kg-mol
  (BACON-TYPE FUEL CELL) $H_2 + 1/2\ O_2 \rightarrow H_2O$

- ASSUME CONVERSION EFFICIENCY OF 50%, YIELDS 43.04 x 10^6 kJ ENERGY

- SYSTEM Z "RED" PAYLOAD HAS RATED POWER REQUIREMENT OF
  11.5 kW OR 362.9 x 10^6 kJ/YR.

- EXCESS FUEL OF ONE STS FLIGHT WOULD ENABLE "ALL-UP" OPERATION
  FOR 43 DAYS

    -- A DUTY CYCLE LEADING TO A LOAD FACTOR OF 0.2 WOULD
       ENABLE OPERATION FOR 7 MONTHS

Fig. 8c. Estimate of energy (power) available from excess STS propellant.

SCIENCE QUESTIONS

- WHAT ARE THE DISTRIBUTION AND MAGNITUDE OF PRECIPITATION OVER LAND AS WELL AS OCEAN AREAS? CAN PRECIPITATION PATTERNS BE CHARACTERIZED IN MORE USEFUL SPATIAL AND TEMPORAL TERMS?

- CAN PRECIPITATION PROCESSES BE OBSERVED AND MEASURED OVER LARGE AREAS RANGING FROM SMALL BASINS TO CONTINENTAL AND OCEANIC AREAS?

- WHAT EFFECTS DO CHANGES IN PRECIPITATION PATTERNS AND AMOUNTS HAVE ON WATER SUPPLY, FOOD PRODUCTION, AND ATMOSPHERIC CIRCULATION?

IMPORTANCE

- PRECIPITATION IS THE MAJOR INPUT AND DRIVING FORCE IN THE HYDROLOGIC CYCLE.

- PRECIPITATION IS ONE OF THE MAJOR FORCING FUNCTIONS IN CLIMATE PROCESSES.

- PRECIPITATION IS THE CRITICAL ELEMENT FOR AGRICULTURAL PRODUCTION AND DOMESTIC WATER SUPPLIES.

- AN OVERABUNDANCE OR MARKED DEFICIENCY OF PRECIPITATION CAN HAVE CATASTROPHIC EFFECTS, NAMELY, FLOODING AND DROUGHT.

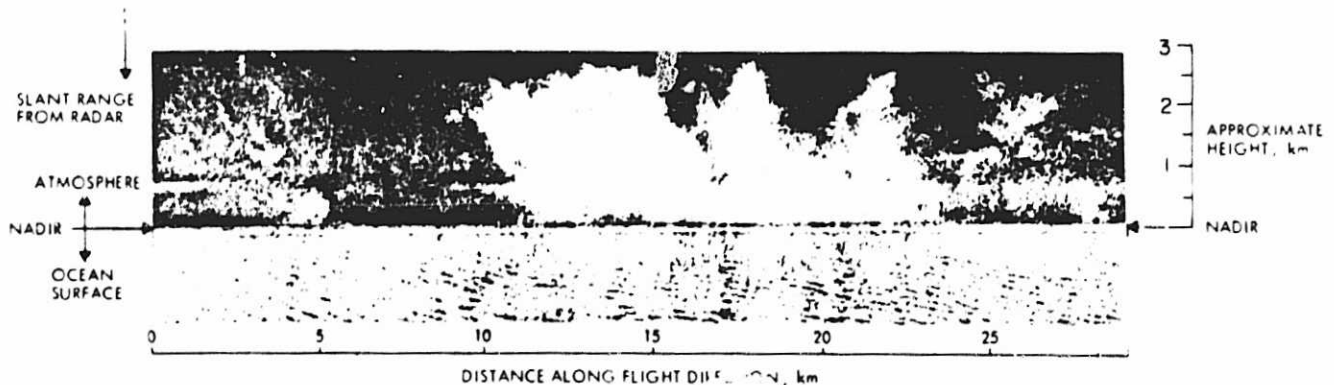Fig. 9.   Hydrologic cycle need for precipitation monitoring.
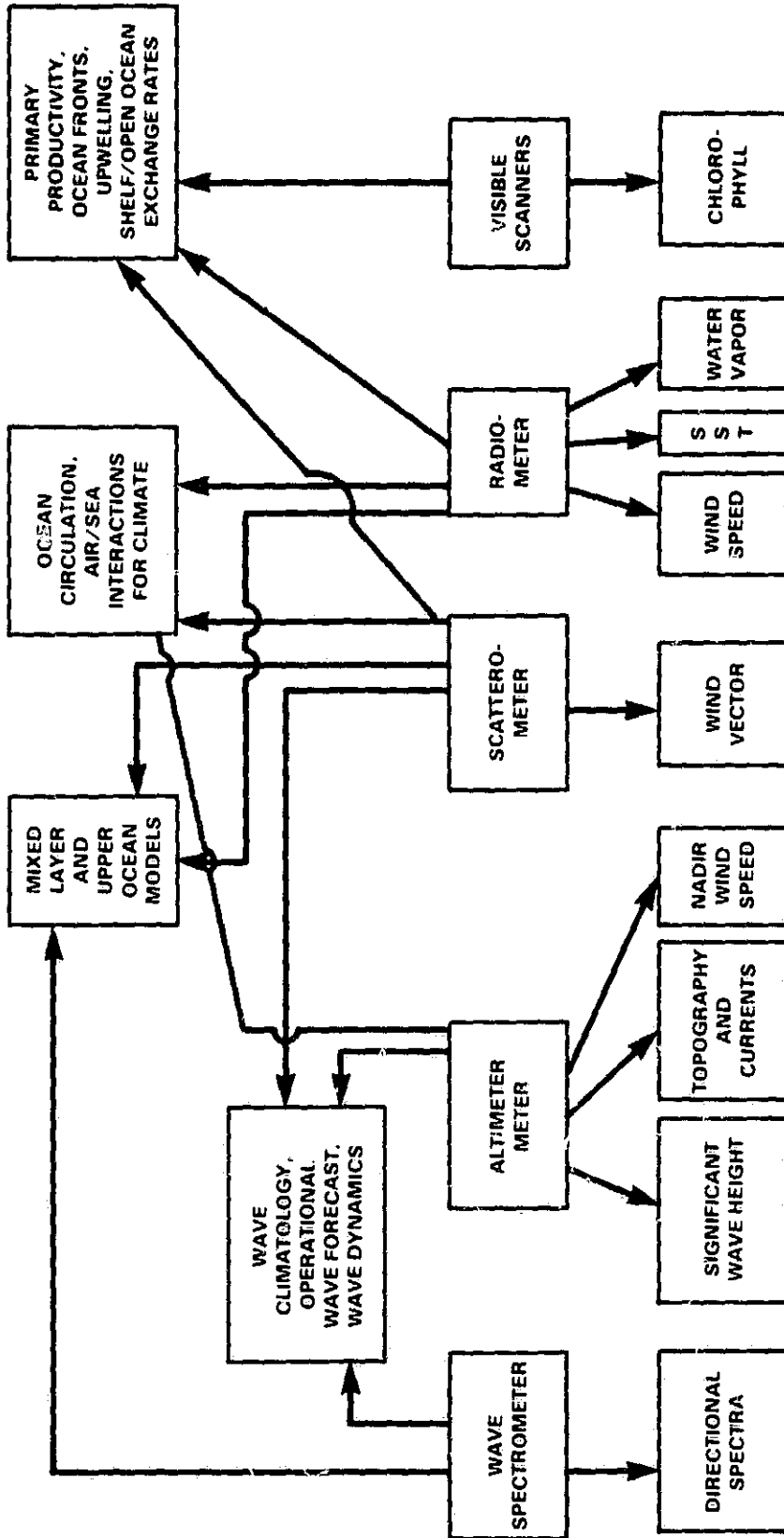

Fig. 10.   Example of system capability.

Fig. 11. Candidate instruments and their relevance to research in oceans programs.

APPENDIX

SPACEBORNE IMAGING RADAR SYMPOSIUM AGENDA

January 17-19, 1983

Jet Propulsion Laboratory
Pasadena, California

Monday, January 17

Opening Remarks (L. Allen, JPL Director)

Keynote Address (J. Moore, NASA Headquarters)

Introductory Remarks (C. Elachi, JPL)

Geologic Research (C. Elachi, Session Chairman)

    Geologic Application of Spaceborne Radars
    F. Sabins (Chevron Research, UCLA)

    Subsurface Geology of the Western Desert in Egypt and Sudan Revealed by
    Shuttle Imaging Radar (SIR-A)
    C. Breed/G. Schaber (USGS, Flagstaff, Arizona)

    Geologic Interpretation of Venus Radar Data
    J. Head (Brown University, Rhode Island)

    Use of Coregistered Radar, Visible and IR Images for Geologic Remote
    Sensing
    D. Evans (JPL)

Sensors and Antenna Technology (J. Welch, Session Chairman)

    Spaceborne SAR Sensor Architecture
    K. Carver (New Mexico State University, New Mexico)

    Shuttle Imaging Radar - A/B Sensors
    J. Granger (JPL)

    Microstrip Antennas for SAR Applications
    H. Haddad (Ball Aerospace Systems Division, Boulder, Colorado)

    Slotted Waveguide Array Antennas for Spaceborne SAR Applications
    D. Bostrom (Hughes Aircraft Company, California)

    Solid State Transmitters for Spaceborne Radars
    T. Turlington (Westinghouse Defense Electronics Center, Maryland)

    SAR Calibration: A Technology Review
    R. Larson (ERIM, Michigan)

Tuesday, January 18

Earth Resources Research (H. Hogg and M. Settle, Session Chairmen)

Stereo Imaging with Spaceborne Radars
F. Leberl (University of Graz, Austria)

SIR-A Aids Regional Geology: Comparisons of SIR-A Imagery with SLAR and
Landsat over Guyana, Venezuela, Nicaragua, and Mali
P. Martin-Kaye (Hunting Geology and Geophysics, London)

Use of Radar Image Texture in Geologic Mapping
T. Farr (JPL)

Mapping and Monitoring Renewable Resources with Space SAR
F. Ulaby (University of Kansas)

Crop Identification of SAR Data Using Digital Textural Analysis
D. Nuesch (University of Zurich, Switzerland)

The SIR-A Atlas
J. Ford (JPL)

Processor Technology (L. Holcomb, Session Chairman)

Processor Architecture for Airborne SAR Systems
C. Glass (Goodyear Aerospace, Arizona)

Performance Evaluation of the JPL Interim Digital SAR Processor
C. Wu (JPL)

Real-Time Digital Processing of SAR Data
T. Bicknell (JPL)

A Fast, Programmable Hardware Architecture for Spaceborne SAR Processing
J. Bennett (MacDonald Dettwiler Associates, Canada)

Acousto-Optic/CCD Real-Time SAR Data Processor
D. Psaltis (California Institute of Technology, California)

Real-Time Synthetic Aperture Radar Image Formation Utilizing an
Electro-Optic Spatial Light Modulator
A. Tanguay, Jr. (USC, California)

Wednesday, January 19

Ocean and Ice Research (L. McGoldrick, Session Chairmen)

Spaceborne SAR and Sea Ice: Status Report
W. Weeks (Cold Regions Research and Engineering Laboratory, New Hampshire)

Radar Image Interpretation Techniques Applied to Sea Ice Geophysical
Problems
F. Carsey (JPL)

Observations of Internal Waves in the Gulf of California by Seasat SAR
L. Fu (JPL)

900 km of Digital Ocean Wave Spectra from the Seasat SAR
R. Beal (Johns Hopkins University, Maryland)

Optimization of SAR for Ocean Wave Imaging
W. Alpers (Max Plank Institute, Hamburg, Germany)

Mechanisms for SAR Imaging of Ocean Surface Phenomena: Theory and
Experiment
J. Vesecky (Stanford University, California)

Future Missions (K. Carver, Session Chairman)

Spaceborne Radar Research in the '80s
C. Elachi (JPL)

NASA Radar Missions
M. Settle (NASA Headquarters)

Radar Activities of the DFVLR Institute for Radio Frequency Technology
W. Keydel (DFVLR,Germany)

European Space Agency, ERS-1 Program
A. Haskell (European Space Agency, Toulouse, France)

The Canadian Radarsat Program
K. Raney (Radarsat Project Office, Ottawa, Canada)

The U.S. Space Station: Potential Base for a Spaceborne Microwave
Facility
D. McConnell (NASA Headquarters)